UNIVERSITÀ DEGLI STUDI DELLA TUSCIA

Dipartimento di Economia, Ingegneria, Società e Impresa

Corso di Dottorato di Ricerca in
Engineering for Energy and Environment
Curriculum Energy and Engineering Systems
XXXV Ciclo

Tesi di Dottorato

Modeling, Design, and Optimization of Multi-Energy Systems

Settore scientifico disciplinare Ing-Ind/08

Tesi di dottorato di
Alessandro Rosati

Coordinatore del corso
Prof. Andrea L. Facci

Tutore
Prof. Andrea L. Facci
Co-tutore
Prof. Stefano Ubertini

A.A. 2021/2022

Ai miei cari.

Contents

Abstract **2**

Introduction **5**

1 Techno-economic analysis of the integration of a BESS in residential sector **17**

1.1 Problem Statement 18
1.2 Modelling and Description of the system 20
1.2.1 Energy fluxes 20
1.2.2 Residential Building 20
1.2.3 Battery 24
1.3 Results and discussion 29
1.3.1 Results 29
1.3.2 Discussion 34
1.4 Summary 39

2 Assessment of residential energy communities integrating an electric vehicles charging system **43**

2.1 Problem Statement 44
2.2 Methodology 47
2.2.1 Charging System 47
2.2.1.1 Hardware 47
2.2.1.2 Software 48
2.3 Case studies 53
2.4 Results and Discussion 61
2.4.1 Discussion 66
2.5 Summary 69

3 Optimized design of a H_2 powered moped 73
3.1 Problem Statement . . . 73
3.1.1 Vehicles selection and description . . . 75
3.2 Methododology . . . 76
3.2.1 Driving cycle . . . 76
3.2.2 Vehicle modeling . . . 76
3.2.3 Optimized control and design . . . 79
3.2.4 Power-train components modeling and design . . . 80
3.2.4.1 Fuel cell . . . 80
3.2.4.2 Metal hydrides . . . 81
3.2.4.3 Buffer battery . . . 82
3.3 Results and Discussion . . . 83
3.3.1 Discussion . . . 87
3.4 Summary . . . 91
3.4.1 Estimated impact and future works . . . 92

4 Performance evaluation of coupled MH-PCM storage systems through non-dimensional numbers 95
4.1 Problem Statement . . . 96
4.2 Methodology . . . 98
4.2.1 Mathematical model . . . 99
4.2.2 Domains discretization . . . 101
4.2.3 The heat exchange model . . . 102
4.2.4 Non-dimensionalization of the problem . . . 104
4.3 Results . . . 104
4.3.1 Absorption results . . . 105
4.3.2 Desorption results . . . 109
4.4 Discussion . . . 112
4.4.1 Case study . . . 113
4.5 Summary . . . 118

Conclusions 120

List of Figures 124

List of Tables 129

Bibliography 132

Ringraziamenti **164**

Abstract

Multi-energy systems are energy systems whereby several types of energy interact optimally each others at various levels. Such systems have a pivotal role in the current global energy transition towards an increasingly sustainable energy sector and distributed generation. However, the full potential of these systems can be achieved only through accurate modeling, design, and optimization operations. In fact, such processes can quantify the performance and the economic and environmental advantages of the elements that compose the multi-energy systems. The analyses must consider the individual elements, their insertion in the system, and therefore the interactions with other components.

Specifically, this thesis studies several technologies: (i) renewable energy sources, (ii) storage systems, (iii) alternative mobility, and (iv) hydrogen elements. Each of them has several peculiarities and critical issues to analyse. Chapter 1 evaluates the economic and environmental impact of the integration of a Li-Ion battery-based electricity storage in a residential context, for several battery capacities and climates. The aim is to determine a climate independent scaling law for the optimization of a battery energy storage system in a residential environment. Chapter 2 examines a condominium system for shared charge of electric vehicles implementing a rule-based logic and a pricing policy aimed at the intelligent use of the available energy and infrastructures. The proposed peer-to-peer charging strategy could be a crucial element for the energy communities. Chapter 3 studies the conversion of a commercial electric moped (Askoll eS_3®) in a fuel cell hybrid-light electric vehicle. An optimization methodology based on backward dynamic programming allows to determine the optimal components design. Such optimal design and operation strategy can be also implemented with a rule-based approach. Chapter 4 evaluates a non-dimensional methodology to feature the operation of several cylindrical metal hydride-phase change material hydrogen tank layouts and to

establish the optimal configuration in terms of power and charge/discharge time. In detail, 13 non-dimensional parameters which completely describe the process are determined through the Buckingham theorem. Finally, the presented methodology is applied to analyse the impact of such parameters on a baseline design metal hydride-phase change material system.

Introduction

The growing concerns about climate change, fossil fuel shortage, and air pollution are driving the global energy transition towards an increasingly sustainable energy sector [1]. In this perspective, the European Commission presented a detailed plan to reduce GreenHouse Gas (GHG) emissions by at least 55% by 2030, compared to 1990 levels [2]. Such result will be the first step in a balanced pathway to achieve climate neutrality by 2050 [3], to keep the CO_2 concentration below its tipping point of 450 ppm [4], and to stabilize the average global temperature rise below 2°C [5]. However, accomplishing such goals is difficult as many interconnected factors influence energy usage, conversion, and consumption. For this reason the energy transition regards all sectors [6–8] and aims to increase energy efficiency, to reduce environmental impact [9], and to optimize energy management [10] through several technological alternatives, such as: (i) promoting Distributed Generation (DG), cogeneration, and trigeneration [11, 12]; (ii) increasing the Renewable Energy Sources (RESs) penetration [13, 14]; (iii) improving the buildings efficiency [15, 16]; (iv) developing and diffusing alternative mobility solutions [17, 18]; (v) increasing the diffusion of secure, effective, and efficient energy storage systems [19, 20], capable of solving the temporal mismatch between production and use of RES [21]; (vi) spreading energy communities [22] and smart grids [23–25].

Multi-Energy Systems (MESs) are closely related to each of these solutions and can represent an important opportunity to improve the technical, economic, and environmental performance of the "classic" energy systems whose sectors are treated "separately" or "independently". From the engineering point of view, an energy system is a cluster of technical and economical elements predisposed to meet the energy demand [26]. Such a system can be used for several applications: stationary power production, mobility, and portable devices. More specifically, a multi-energy system

is a particular energy system whereby electricity, heat, cooling, hydrogen, fuels, transport, and so on interact optimally each others at various levels (for example within a district, city, region or nation) [27]. All the elements mentioned above (renewable energy plants, alternative vehicles, storage systems, etc.) collaborate in a MES (Figure 1) in order to satisfy the request from user, minimizing energy waste and harmful emissions. Making all these technologies effectively usable and performing requires substantial investments, appropriate policy choices, considerable design efforts, and research activities [12].

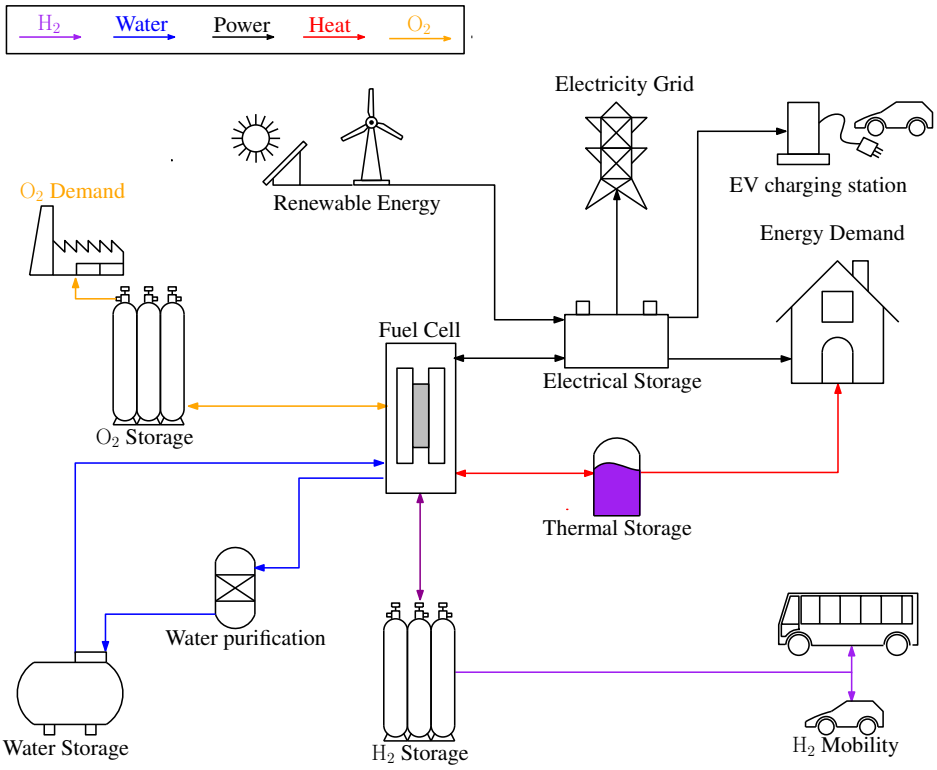


Figure 1: *Example of multi-energy system.*

In this new energetic phase, the distributed generation represents a different way of thinking and managing the electricity grid, based no longer, or rather not only, on large power plants connected to extended networks, but on small-medium sized production units integrating renewable energies. These plants are distributed homogeneously in the territory, connected directly to the utilities or in any case to low-voltage networks and can have powers ranging from a few W to hundreds of MW in the largest

cases [28]. The main advantages of distributed generation are: (i) shorter electricity distribution and transmission networks. This allows to decrease the construction and maintenance costs and to avoid electric energy losses that are around 7% of the electricity transported for the long high voltage networks [29]; (ii) greater network reliability, since the shutdown of a system does not lead to the interruption of the supply, but it is compensated by the presence of other plants. This aspect is particularly important for renewable energy systems, for which the most part of supply energy is in a discontinuous manner; (iii) reduction of harmful emissions and greenhouse gases; (iv) "greater intelligence" of the network; (v) exploitation of energy that would otherwise be lost. Within this new scenario, the electricity grid completely changes its role and functions. In fact, it will gradually transform itself from a "passive" network to an "active" and "intelligent" network (smart grid), capable of managing and regulating multiple electrical flows that circulate in a discontinuous and bidirectional manner [29]. In this new energy frontier, multi-energy systems play a role of primary importance, being the main energy production units integrated into the smart grid.

Moreover, the concepts of energy and time are tightly connected. In this respect, shifting demand to match supply and re-conceptualizing interactions between time and energy is pivotal to achieve low-carbon energy goals [30–32]. As a consequence, the design of new MESs must rely on real time-varying consumption data, rather than on peak or average demands to allow the contemporary optimization of production and demand phases [12, 33–36]. In this scenario, load control technologies (i.e. storage technologies) able to reshape customer load profiles with the aim to optimize the use of RESs [37] are central. Such storage technologies still need a co-evolution of innovation, investment, and deployment strategies [38]. This, highlights a significant knowledge gap on techno-economic assessment of electricity storage systems. Among the different energy storage solutions, Battery Energy Storage Systems (BESSs) are the most widespread technology [39–41]. Batteries are used in a wide range of applications such as energy storage, electric utility, portable devices, and electric vehicles [39–43]. They have drawn considerable attention thanks to favorable features, such as fast response, controllability, and geographical independent operation [44, 45]. The integration of RESs and BESSs is an effective approach to solve the temporal mismatch between production and use, and to perform peak shaving, load leveling, demand response, voltage regulation,

frequency regulation, and other ancillary services [46–50]. Batteries can also reduce the cost of electricity in commercial buildings and residential dwellings by absorbing and storing energy from the grid during off-peak periods and injecting it during high-demand periods when prices are very high [51, 52]. However, their investment cost is still high [53] even though in the last decade the price of Lithium-Ion (Li-Ion) batteries has fallen, and this trend is expected to continue [54]. In 2012 the contribution of buildings to the final energy consumption in Europe was 40%, making the building stock responsible for 36% of the total European CO_2 emissions [55]. Over the years, the buildings share of the final energy consumption has remained fairly stable and in 2017 it stood at around 42% [56]. Since 2007, stringent building codes and policies caused this value to decrease slightly in residential buildings. Conversely, the final energy consumption in non-residential buildings remained stable over the last decade [55]. In commercial buildings, high consumption ordinarily occurs during the daytime, when the PhotoVoltaic (PV) production also peaks. Instead, in residential buildings the consumption is usually lagged in time with respect to PV production. As a consequence, they are excellent candidates for increasing self-consumption thanks to the use of BESSs [57, 58]. Such considerations highlight that it is necessary to refurbish existing buildings and to design new ones with low energy demand, availability of RESs, and electricity storage [59–62]. In the last decade new policies have introduced technical and regulatory measures to promote a more rational energy use in the residential compartment [63–65]. One key is the introduction of nearly Zero Energy Buildings (nZEBs) concept as the new building target [66–70]. A nZEB is a building with a very high energy performance, where the nearly zero or the very low amount of energy required is covered to a very significant extent by energy from renewable sources produced on-site or nearby [71]. In such a building environment, Li-Ion battery systems are particularly suited to achieve high self-sufficiency, see for instance [72]. Therein, three different types of batteries, including lead acid, NaNiCl (Sodium-Nickel-Chloride) and Li-Ion, are studied in combination with PV within the Swedish context. Similarly, several studies focus on techno-economic analysis of BESS in residential buildings in specific energy markets and climates. In particular, in the Australian energy market combining PV and BESS gathers a sustainable investment [73]. In Finland, BESS is demonstrated to increase the PV optimal size for both apartment and detached houses [21]. However, such a result is subject

to the adoption of dedicated energy pricing policies. In the same way, for the United States energy market sustainability of the investment of BESS combined with PV still relies on the implementation of financial support mechanisms [74]. The profitability of combining PV and BESS in the residential environment depends on the possibility to significantly increment renewable energy self-consumption [75]. This also evidence the importance of selecting a proper control strategy [76, 77]. The relevance of such a control strategy is demonstrated for a MES in Hong Kong [76] and for a low energy building in China [77].

Alternative mobility, especially the electric mobility, is another key area for achieving climate neutrality. It has crossed a critical threshold leveraging on several increasingly important issues: carbon constraints, high oil prices, rise of organized car-sharing, and inter-modality [78]. Moreover, to facilitate its success the European Commission has set several goals on different scales. The key short-term goal is to improve local air quality [79]. To accomplish this, a 55% reduction in car emissions and a 50% reduction in van emissions by 2030 are planned. In the longer term, the Commission has developed a comprehensive strategy to phase out the conventionally powered cars [80]. In fact, no new cars with combustion engines will be sold from 2035 onward [81]. Electric Vehicles (EVs), both Plug-in Hybrid Electric Vehicles (PHEVs) and Battery Electric Vehicles (BEVs), are considered essential elements of such new sustainable context. These vehicles are two to four times more efficient than conventional internal combustion engine models and can reduce reliance on oil based fuels as well as deliver significant reductions in GHG emissions when running on low-carbon power [82–84]. After a decade of rapid growth in the EVs market, at the end of 2020 there were 10 millions electric cars in the world. In addition, in the first-quarter of 2021, global EVs sales rose by around 140% compared to the same period in 2020 [83]. This steady growth in sales is due to the continuous increase in the average driving range of the new BEVs, and to the decrease in their price [85], mainly driven by the lower cost of Li-Ion batteries. In fact, the weighted average range for a BEV increased from 200 km in 2015 to about 350 km in 2020. Li-Ion batteries prices in 2010 were above 1100 $/kWh and have fallen to 137 $/kWh in 2020 (89% reduction in real terms) [86, 87]. Future projections by BloombergNEF [86] indicate that the average prices will be soon close to 100 $/kWh. However, there are still several shortcomings that slow down massive EVs diffusion: high purchase and battery cost

[88], uncertain battery life, limited battery range, and "range anxiety" due to limited capillarity of charging infrastructures and long charging times [89–91]. Besides, regarding the electric battery range, there is a notable misperception among EVs drivers that the range cannot meet their actual driving needs [92]. The limited diffusion of charging infrastructures is one of the major problems that hinders the growth of electric mobility [93]. Electric vehicles sales and charging infrastructure development are connected through a tight loop [94]. In fact, without an adequate infrastructure, electric cars will not take over traditional vehicles. Conversely, as long as the electric vehicles market does not significantly grow, the infrastructure will never be built as the investment would be hardly recoverable [95]. Furthermore, a wider penetration of electric vehicles could generate problems on the grid such as phase imbalances, energy quality reductions, and overloading of transformers and lines [96, 97]. The lack of charging infrastructure is particularly relevant in residential buildings, where there is also the problem of shared electricity, which does not meet the EVs owner's requirements [98]. In fact, in residential context there is a widespread reluctance regarding the installation of EVs charging stations that could only be used by a few homeowners [99]. In addition, there is also a problem regarding the safety of electrical installations, since they are not built to support EVs charging stations and an upgrading of the condominium infrastructure could be necessary [98–101]. Literature demonstrates that it is possible to control and coordinate the charging schedule to improve electric mobility systems performance and sustainability. The coordinated EVs charging methods can be categorized into three types depending on the objective function [102, 103]:

- To reduce the effects of EVs charge on the distribution grid. Regarding the minimization of the effects of EVs on the grid, the authors in [104] and [105] evaluate the impacts of EVs charge on transformer capacity overloading, system power losses, and voltage deviations highlighting the need for controlled charging methods. Other studies conclude that uncontrolled charge of EVs loads can limit the EVs percentage penetration into the distribution grid [106–108]. In [109] an EVs optimal controlled charging policy using artificial immune systems is presented to minimize power losses, and to avoid overload as well as higher voltage levels. In [110] a charging strategy is proposed to minimize the peak load demand. The authors in [111] introduce a demand response strategy to decrease the potential im-

pacts of new load peaks due to EVs integration, while minimizing the cost of upgrading the infrastructure. In [112–115] the optimal charging control for EVs is achieved by optimizing the EVs energy usage through different method, also considering the Vehicle-to-Grid mode.

- To minimize the EVs charging cost. Several researchers propose to adjust the EVs charging rates and charging start times in order to minimize the charging cost. For instance, the authors in [116] introduce a control model for EVs charge according to real-time electricity price information. A real-time V2G control algorithm with price uncertainty is proposed in [117] to maximize the profit of each EV owner. In [118], [119], and [120] optimal EV control strategies are presented to minimize the total cost of electricity that the owners pay for their own vehicle charge. In [121] a real-time non-cooperative model is developed in order to encourage the EVs owners to change their charging schedule from peak hours to off peak hours. Finally, the study in [122] aims to minimize the EVs charging cost within the electrical system constraints, while in [123] the authors suggest a centralized approach to coordinate the EV charge.

- To use EVs batteries to store energy from renewable sources in a context of distributed generation and Vehicle-to-Grid (V2G) mode. Also the possibility to use renewable electricity from sun and wind has been largely investigated in literature [124]. In [125], the authors deepen the advantages of implementing charging stations based on large-scale turbines and show that EVs could be a critical factor for enabling the high penetration of wind energy. Moreover, shifting EVs charge to times with high wind availability allows to achieve cost savings [126]. Similarly, the analysis of a charging infrastructure with photovoltaic panels highlights that switching the EVs charge from night time to day time, which would match with peak solar production, could increase solar energy penetration and reduce charging cost [127]. Finally, several studies [128–131] show that a hybrid infrastructure (for example, solar energy, wind energy and battery energy system) with optimised EV charging methods could have environmental, cost, and grid advantages.

In the new and complex energy panorama, hydrogen technologies are and will be vital in different areas such as mobility, stationary energy gen-

eration and storage, and industrial applications [15, 36, 132] In the same way, they will also be crucial also in MESs. Fuel Cells (FCs) produce electricity by highly efficiently (electrical efficiency up to more than 60 % [133, 134]) oxi-reducing hydrogen. Therefore, stationary and mobility applications implementing FCs can reduce the operational costs and the emissions of carbon dioxide and other pollutants compared to traditional energy conversion systems. An extensive utilization of hydrogen (called as *hydrogen economy*) needs also harmless, compact, light and cost-efficient hydrogen storage [135]. The main hydrogen storage methods include gas, liquid, and solid storage [136], and every technique has its own strengths and weaknesses [137]. Among these methods, solid state Metal Hydride (MH) hydrogen storage is one of the most promising solutions for several stationary and mobile applications [138]. The main advantages of MHs over the other storage techniques are their high degree of safety and reliability, high hydrogen volumetric density, comparatively low operating pressure, the possibility of operation at room temperature and relatively low cost [139–142]. Nonetheless, none of the current MH technologies fulfills all the essential criteria for a practical hydrogen economy [135], especially due to their slow kinetics and the difficulty in controlling MH temperatures during hydrogen absorption and release. More specifically, being the hydrogen absorption (hydrogenation) and hydrogen desorption (dehydrogenation) to/from MH respectively exothermic and endothermic processes, the rate at which the hydrogen gas is absorbed can be maximized by lowering the system temperature, and the converse happens for the desorption process [143]. Therefore, advanced thermal control and management are crucial to enhance MH performance [144, 145].

In the mobility field, Fuel Cell Electric Vehicles (FCEVs) [146, 147] can offer several opportunities over BEVs, such as higher volume energy density of the storage, longer driving-range, shorter refueling times, and better drivability because their performance does not depend on the State of Charge (SoC). Moreover, FCEVs can ease the integration of RESs through higher flexibility in terms of fuel production, storage, and delivery. In this regard, the deployment of FCEVs based on blue and green H_2 must be addressed by considering the whole chain from the H_2 production, to its long term storage and distribution, on-board storage, and, finally, to the road. Fuel Cell Hybrid Electric Vehicles (FCHEVs) result from the combination of fuel cell and battery as energy sources [148]. Such combination enables to keep all the FCEVs advantages, while enabling the optimization of the

overall design [148, 149]. Several technical and economical challenges need to be subdued in order to make FCEVs and FCHEVs popular and successful competitor with conventional vehicles for consumers. Among such challenges there are: higher initial cost, higher replacement cost, possible increase in weight, and long-term reliability. Micro-mobility is an exponentially growing new trend [150], especially in urban environments [151]. In particular, Battery-Light Electric Vehicles (B-LEVs) such as e-bikes, e-scooters, and e-mopeds [152] offer different advantages over traditional ICE-based four- and two-wheeled vehicles [153]. For example, B-LEVs require less energy for production and operation [154], positively affect urban congestion by using less parking and driving space, and produce significantly less noise and harmful emission [155]. Thus, micro-mobility and new ownership models such as sharing services with B-LEVs are emerging in cities worldwide [156, 157]. According to the European Union guidelines, e-mopeds are two-wheeled motor vehicles with up to 4 kW for electric motors [158]. Since its inception in 2012, the e-moped sharing market has been growing year by year. The number of shared e-mopeds available worldwide increased by 164% in 2019 compared to 2018 [159] and by 58% in 2020 compared to 2019 [160]. Such diffusion of electric micro-mobility can be further boosted by developing and implementing Fuel Cell Hybrid-Light Electric Vehicles (FCH-LEVs), considering the aforementioned technical advantages. Power-train design and sizing is key towards maximum vehicle efficiency and durability [161–163], especially for hybrid systems [164, 165]. The application of the optimal management of the power-train to its design reduces both power demand and energy consumption, fostering the downsizing of the components [166, 167]. In fact, the operating efficiency largely depends from the control strategy [33, 168], as demonstrated in several studies [132, 169, 170]. The optimal management design has been proposed in [171] for a fleet of ZEVs. The potential of such design and control methods applied to the power-train of e-moped FCH-LEVs, has not been fully unveiled yet. In fact, only few papers study the optimized design of FCHEVs in bikes [172, 173], cars [174, 175], and yard-trucks [176]. Only few prototypical examples of motor-bikes [177] and e-moped FCHEVs exist [178]. Moreover, also the integration of MH tanks in the vehicles is a relatively untreated topic.

For what concern the hydrogen storage, literature shows significant research and development efforts to improve heat transfer in the MH tanks, in order to efficiently operate alternate heating and cooling and obtain re-

action times of practical interest. In particular, current research works focus on: (i) techniques to improve the effective thermal conductivity of the MH bed; (ii) high efficiency internal/external heat exchanger; (iii) Phase Change Materials (PCMs) utilization. Several studies evaluate simulation models for heat and mass transfer in MH tanks to determine the optimal system design and characteristics [179–186]. Various MH tanks configurations have an external heat source to generate the desorption heat and/or a cooling system to extract the absorption heat. More specifically, the usage of heat exchangers such as straight tubes [187], helically coiled tubes [188–190], multi-tubes [191, 192], tubes with fins [193–195], and heat pipes [196–198] is assessed. The results show that such heat exchangers are an efficient way to improve reaction kinetics. A more elegant (and efficient) solution is to store the heat emitted by the MH during the absorption process and then to reuse it in the desorption process. Such a "regenerative" process can be achieved through the thermal coupling of MH with phase change materials. PCMs are latent heat thermal storage systems used to stock and release heat in a narrow temperature range through melting and solidification [199, 200]. Currently, various researches investigate different aspects of MH-PCM coupling [201–203]. The purpose is to store all the heat released during the hydrogenation of the MH tank, thus minimizing the loading time and increasing the power performance of the reactor. To this end, the choice of an appropriate PCM and the optimization of its quantity are essential to ensure efficient heat transfer and fast hydrogen charge and discharge rates [204]. The PCM should have high thermal conductivity and melting enthalpy and a suited phase change temperature. In particular, the melting enthalpy should be equal or bigger than the reaction enthalpy of MH [143], and the phase change temperature must be between the highest and lowest temperatures reached during the whole process to maintain a sufficient temperature gradient for heat transfer [205]. In [206], the authors examine a MH-PCM system studying the PCM choice and evaluating the effect of several thermodynamic properties such as melting temperature, latent heat of fusion, specific heat capacity, density, and thermal conductivity. Especially, such last parameter is low for most PCMs [207] and an improvement is needed to enhance the heat exchange. In this perspective, Metal Foam (MF) can be integrated into both PCM and MH. Various researches study the integration of different MFs into the metal hydride to improve the hydrogen storage performance [208–210], and into PCM to improve thermal storage performance [211–

213]. In [214], a survey on a MH reactor surrounded by a PCM composited with MF is presented. Such MF-PCM-MH system shows improved heat transfer and hydrogen storage efficiency. In most literature research, PCM is matched with MH by surrounding the tank. For cylindrical storage canisters, the limited contact area between MH and PCM restricts heat transfer and hydrogen storage performance. Thus, it is vital to find alternative layouts to overcome this problem. In [215], a spherical and a cylindrical storage tank surrounded by PCM are compared. The results show that the spherical configuration is 22% faster than the cylindrical one to reach 80% storage capacity under the same conditions. In [216], a novel type of MH-PCM unit (PCM sandwiched between two layers of MH) is presented, along with a mathematical model to describe the hydrogen ab/desorption of MH and the heat storage/release of PCM. Such a new sandwiched MH-PCM configuration is compared with classical PCM-surrounded layout in [217]. The results show that hydrogen absorption and desorption times are reduced of $\sim 78\%$ and $\sim 59\%$, respectively, in sandwiched MH-PCM units, compared to cylindrical PCM-surrounded tank. The sandwiched MH-PCM configuration has faster charge and discharge rates due to the greater heat exchange area (about 2.5 times).

In this work all the topics related to the multi-energy systems presented in the introduction are debated. In Chapter 1 we assess a climate independent scaling law for the integration and the optimization of a battery energy storage system in a residential environment. In particular, we evaluate the environmental and economic impact of the introduction of a Li-Ion battery in a real existing nZEB, for five different climates and for several battery capacities. In Chapter 2 we develop a condominium system for shared charge of EVs implementing a rule-based logic and a pricing policy aimed at the smart use of the available energy and existing infrastructures. Chapter 3 evaluates the techno-economic feasibility of the conversion process of a battery electric moped in a fuel cell electric moped. Finally, Chapter 4 studies a non-dimensional methodology to characterize the operation of different cylindrical metal hydride-phase change material tank layouts and to determine the optimal configuration in term of charge/discharge time and power.

Chapter 1

Techno-economic analysis of the integration of a BESS in residential sector

Effective electricity storage solutions that decouple energy use and production are central to the green energy transition. In particular, in the residential sector, the implementation of such solutions should boost the potential of nearly Zero Energy Buildings (nZEBs) to reduce the primary energy consumption and greenhouse gases emission and towards a greater energy self-sufficiency.

Despite site-specific studies clearly evidence the usefulness and profitability of the Battery Energy Storage Systems (BESSs) in the residential setting, to the best of our knowledge, climate independent general scaling laws are still not established. In this chapter we posit the challenge to determine such scaling laws by dissecting the behavior of a whole nZEB for different climatic conditions and BESS capacities. We model all the elements of the system (residential building made of 13 apartments, reversible heat pump, PhotoVoltaic (PV), and Li-Ion battery). Specifically, we consider the BESS performance as a function of the State of Charge (SoC) and temperature, and its thermal management and geometry. High resolution measured energy demands are only sparsely available due to the limited diffusion of smart energy meters in residential settings and privacy concerns [218, 219]. Thus, we determine the nZEB energy demand through a thermodynamic building model validated by comparison against site-specific measures.

The chapter is organized as follows. The problem statement is presented in Section 1.1. In Section 1.2 we describe the system, its control logic, and the numerical models. Results are presented and discussed in Section 1.3. Finally, in Section 1.4, we draw the conclusions.

1.1 Problem Statement

In this chapter we dissect the environmental and economic impact of the integration of a Li-Ion battery-based electricity storage in a residential setting (Figure 1.1), for different climates and with different battery capacities. We analyze a year of system operation for the five different climates with a hourly time discretization.

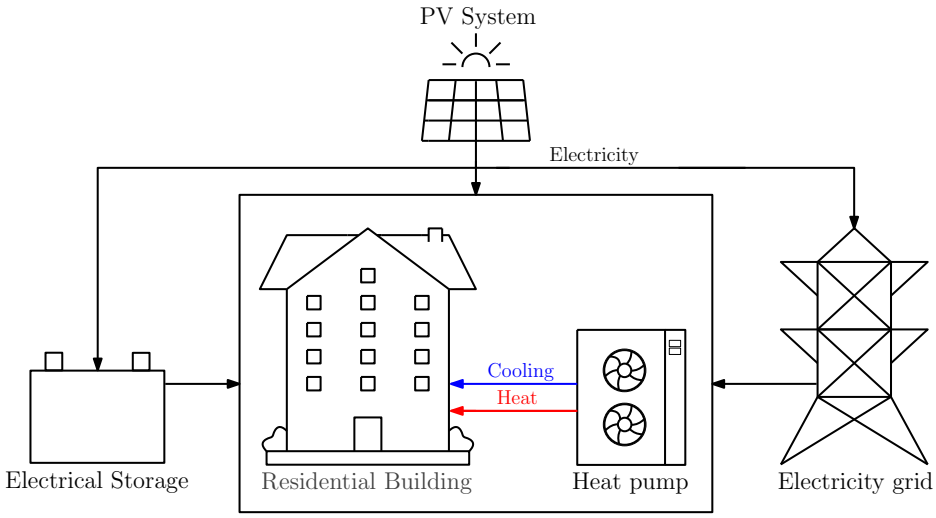


Figure 1.1: *Schematic representation of the main elements of the system.*

We consider a building designed following the "Directive of the European Parliament on the energy performance of building" (2010/31/*EU*) [220] and that meets the "Casaclima" energy certificate [221]. It belongs to the CasaClima A energy class (Class A for what concerns the envelope efficiency, Gold Class for what concerns the overall energy efficiency). It can be considered as a nZEB, and it is representative of future energy communities, in particular in a context of distributed generation [222]. The building is located in Viterbo, Italy, and is equipped with energy meters that allow to validate its modeling. Its main features are shown in Table 1.1. The building integrated PV (Figure 1.1) utilizes 75% of the

total building roof, for a peak power $P_{peak} = 38.6\,\text{kWp}$. A 42 kW centralized reversible heat pump system provides cooling and heating energy. Notably, such a system converts heat and cooling loads into an electricity demand, and the nZEB requires no fuels.

Feature	Value	Unit of Measure
Surface	1314	m^2
Floors	6	–
Apartments	13	–
Roof Surface	263	m^2

Table 1.1: *Relevant properties of the selected building reported in the "Casaclima" energy certificate.*

Electricity is stored in Li-Ion pouch cell batteries (i.e. those used in the Nissan Leaf car) whose main characteristics, according to the $IEC\,62660-1$ [223], are shown below in Table 1.2. Battery capacity is varied by changing the arrangement and number of cells.

Feature	Value	Unit of Measure
Rated capacity	56.3	Ah
Nominal voltage	3.65	V
Lenght	261	mm
Width	216	mm
Thickness	7.91	mm
Mass	914	g
Energy density	224	Wh/kg

Table 1.2: *Relevant properties of the Li-Ion pouch cells, according to* $IEC\,62660-1$ *[223].*

Environment temperature influences heating and cooling energy demands and, consequently, the interaction between the PV, the battery, and the electricity grid. To dissect such an influence, we consider five different climates, according to the International Energy Agency (IEA) classification [224]: Cold, Heating based, Moderate, Cooling based, and Hot. The IEA classifies the climatic conditions according to the total number of Heating Degrees Days (HDD) and Cooling Degrees Days (CDD) per year, as reported in Table 1.3. Therein, we also report a representative

European city for each climate.

Climatic Zone	HDD [°C]	CDD [°C]	City
Cold	≥ 2000	≤ 500	Warsaw (Poland)
Heating based	≥ 2000	$[500, 1000]$	Viterbo (Italy)
Moderate	≤ 2000	≤ 1000	Malaga (Spain)
Cooling based	$[1000, 2000]$	≥ 1000	Athens (Greece)
Hot	≤ 1000	≥ 1000	Larnaca (Cyprus)

Table 1.3: *Heating and Cooling Degrees Days and representative cities for each IEA climatic zone [224].*

1.2 Modelling and Description of the system

1.2.1 Energy fluxes

The system bidirectionally interacts with the electricity grid as evidenced in Figures 1.1 and 1.2. The load is first satisfied by the PV system. When its production is larger than demand, the surplus energy is sent to the battery and, once its maximum SoC is reached, to the grid. If the building consumption is greater than the PV production, the necessary energy is first drawn from the battery. When it is discharged, the grid feeds the required power.

1.2.2 Residential Building

We model the building through the "EnergyPlus" software [225]. It uses a thermodynamic approach based on energy and mass balance equations [225]. The building can be divided into different zones based on their usage and required temperature. The model inputs are: (i) the geometry of each building zone; (ii) the envelope properties; (iii) the activities (e.g appliances and lighting schedule) related to each zone; (iv) the temperatures that must be guaranteed in each zone; (v) the characteristics of the heat pump. Finally, a Typical Meteorological Year (TMY) provides all the meteorological data for each location. The outputs are the hourly electricity and Heating, Ventilation and Air Conditioning (HVAC) energy demands for each building zone for a calendar year.

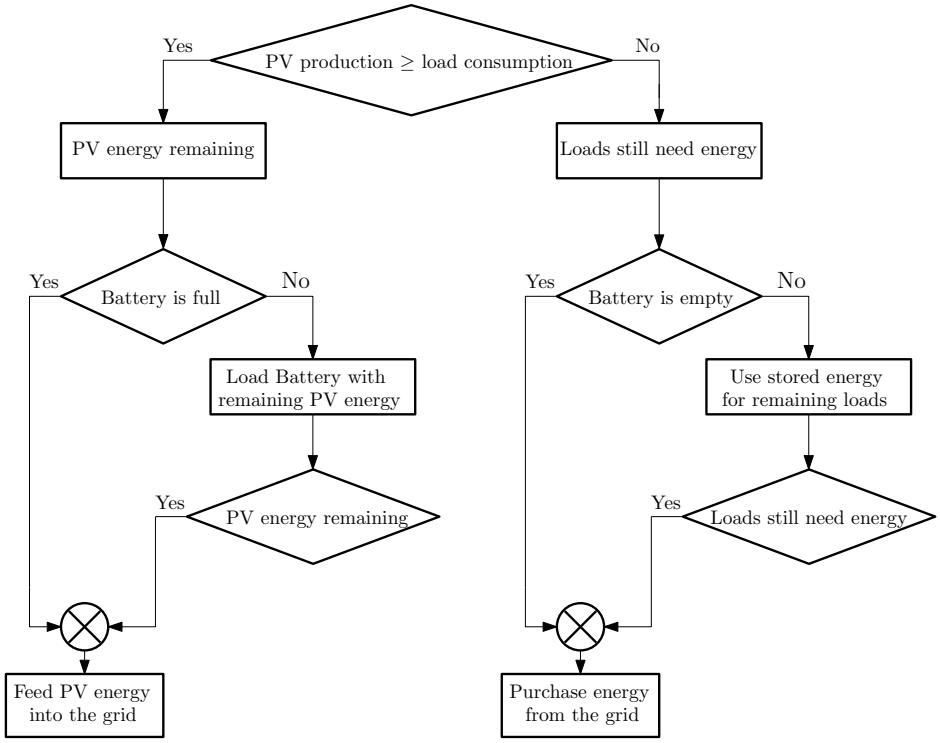


Figure 1.2: *Representation of the nZEB energy fluxes control logic.*

Apartments require electricity for lighting, appliances, and HVAC. Figure 1.3 shows the lighting and appliances consumption of an apartment (u_{el}) calculated through EnergyPlus for one week. On weekdays, it shows a repetitive daily trend with a peak in the morning and one in the evening. Weekends show three peaks per day: one in the morning, one at lunchtime, and one in the evening. The morning peak occurs earlier on weekdays than on weekend, as tenants get up earlier to go to work. On weekends, tenants spend more time at home and consume more energy, as arguable from the lunchtime peak and the longer duration of the evening peak compared to weekdays. The u_{el} time trace consistently repeats for all weeks of the year being excessively repetitive compared to real energy demands. Moreover, all the apartments have the same u_{el}.

To gather a more realistic demand we refer to the electricity demand of the i^{th} apartment

$$u^*_{el,i}(t) = u_{el}(t) + \sigma_i(t)\,, \tag{1.1}$$

where $\sigma_i(t)$ is a Gaussian white noise and t is time. Such a procedure does

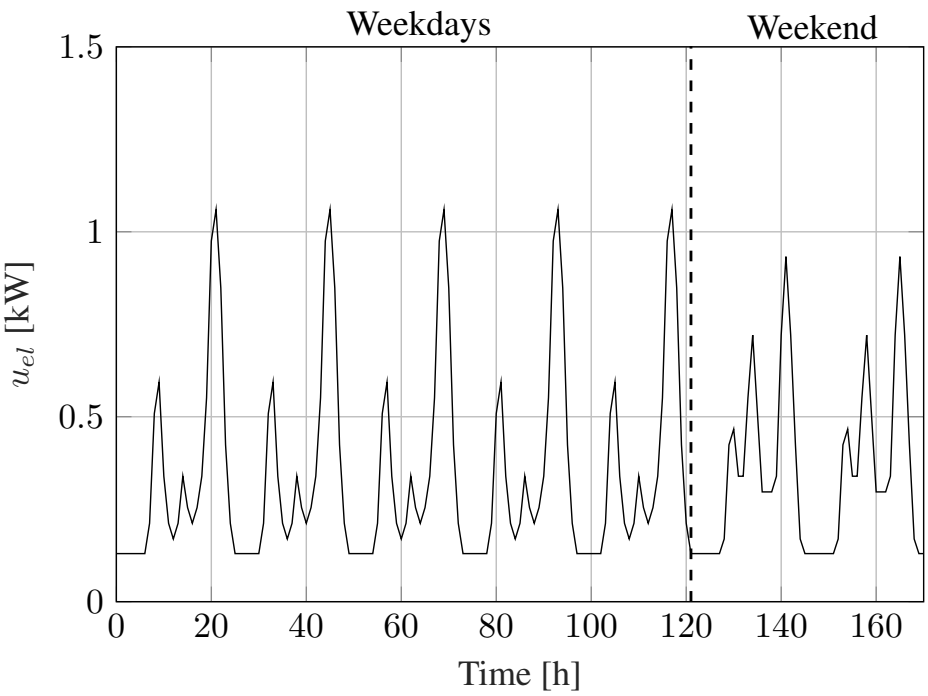


Figure 1.3: *Weekly appliances ad lighting consumption (u_{el}) of an apartment in the building.*

not impact the total energy consumption as σ has zero average. We estimate the amplitude of σ_i from the electricity consumption data reported in [218]. Specifically, we decompose each consumption profile (u) as

$$u(t) = \bar{u}(t) + u'(t)\,, \tag{1.2}$$

being $\bar{u}(t)$ the phase average

$$\bar{u}(t) = \frac{1}{7}\sum_{0}^{6}\left(u(t) + u(t+24)\right)\,. \tag{1.3}$$

Figure 1.4 reports the consumption deviation from phase average ($u'(t)$) relative to the data in Figure 1 and 9 of [218]. We assume that the amplitude of σ_i equals $\max(u'(t)) = 0.6\,\text{kW}$. The resulting $u^*_{el,i}(t)$ is exemplified in Figure 1.5.

We add the HVAC consumption to obtain the total electricity demand of each apartment ($u_{tot,i}$)

$$u_{tot,i}(t) = u^*_{el,i}(t) + \frac{u_{h,i}(t)}{\text{COP}_h} + \frac{u_{c,i}(t)}{\text{COP}_c}\,, \tag{1.4}$$

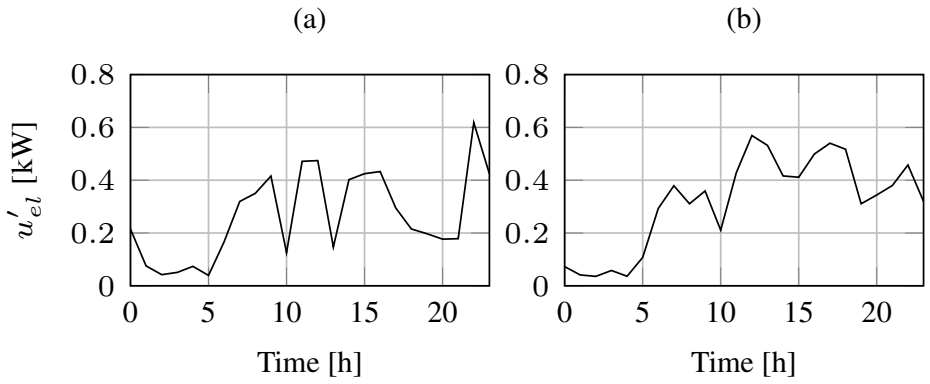


Figure 1.4: *Consumption deviation from phase average relative to (a) the data in Figures* 1 *of [218]; (b) the data in Figures* 9 *of [218].*

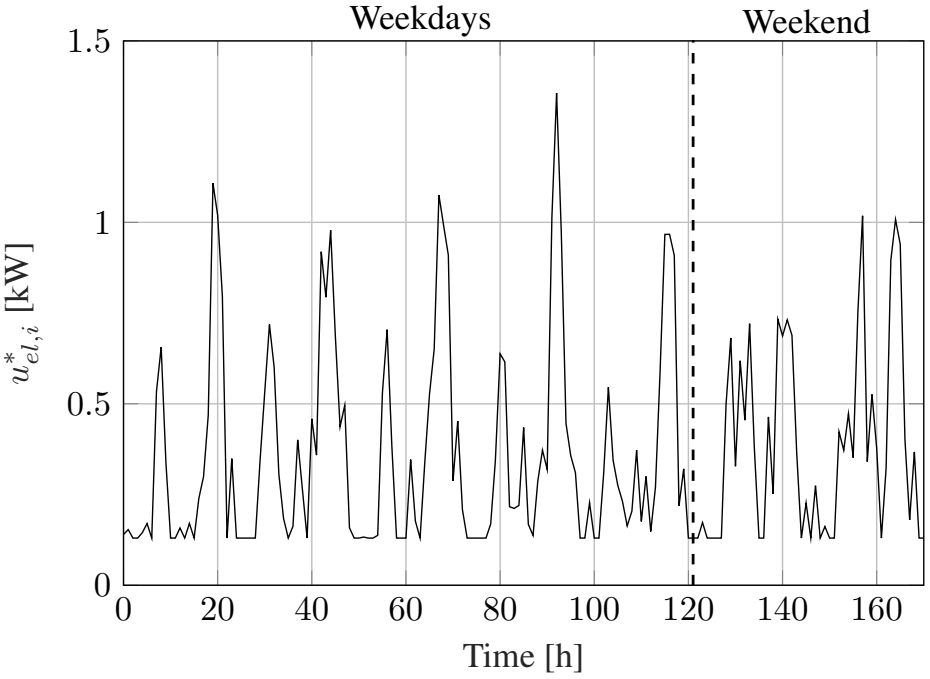


Figure 1.5: *Modified weekly appliances ad lighting consumption ($u^*_{el,i}$) of an apartment in the building.*

where $u_{h,i}$ and $u_{c,i}$ are the heat and cooling demands respectively, while COP_h and COP_c are the heat pump Coefficients Of Performance for heating and cooling operations, respectively.

Finally, the total electricity demand (u_{tot}) is the sum of all the $u_{tot,i}$ and of the lighting consumption of the common areas of the building.

The obtained energy demand is validated for the heating based climate. Table 1.4 compares the model results to measured data and to the "Casaclima" energy certificate requirements for the yearly consumption of electricity for appliances and lighting (U_{el}), heating (U_h), and cooling (U_c).

	Building Model	Measured Data	"Casaclima" Data
U_{el} [kWh]	42856	46319 [226]	38000
U_h [kWh]	7099	6013.3	6574
U_c [kWh]	15426	15898	//

Table 1.4: *Consumption data obtained, measured, and reported in the "Casaclima" energy certificate for the residential building in the Heating based climate.*

Measured data for U_{el} are not available for the present building. Yet, the obtained value is consistent because it is included between the consumption reported in the "Casaclima" energy certificate and the one reported in [226] for a similar residential building (with the same number of apartments). U_h is slightly higher than the measured data and that of the "Casaclima" certificate. U_c is the same as that measured in the residential building. The "Casaclima" certificate, does not report data for U_c.

PV production (P_{pv}), is estimated through the "PVGIS" platform for each considered locations [227].

1.2.3 Battery

The battery is made of Li-Ion pouch cells, whose characteristics are shown in Table 1.2. We model the cell through the zero-th order equivalent circuit presented in [228] (Figure 1.6).

This model demonstrated to be adequate for estimating the losses that occur during battery operation [229, 230]. We assume that at time t the current flowing in and out of the battery terminals (I), the battery temperature (T) and the SoC are known. For the battery charging process I is negative. Conversely, for the discharge process it is positive. The battery load voltage (V_L) is defined as

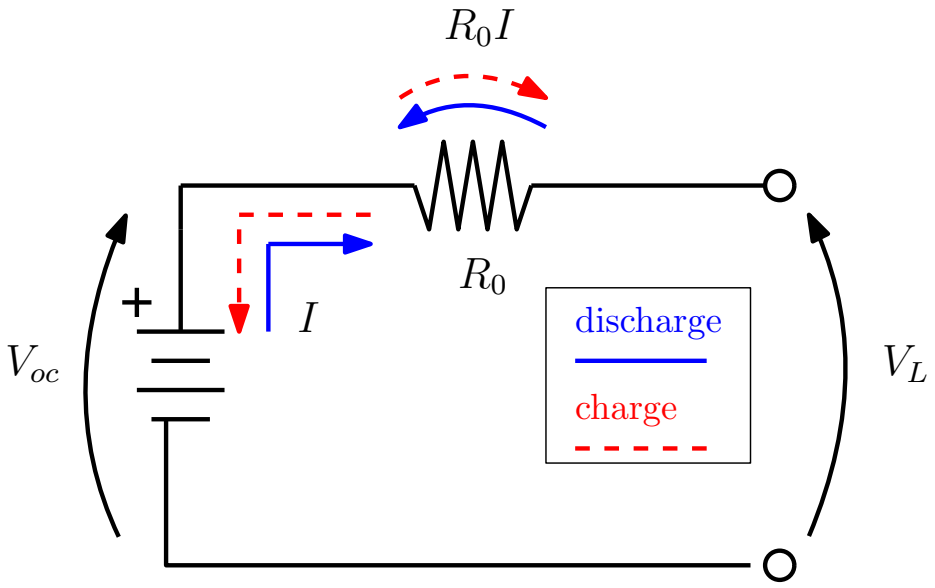


Figure 1.6: *Zero-th order electrical circuit model of the battery [228].*

$$V_L(t) = n_s[V_{oc}(t) - R_0(t)I(t)n_p]\,, \tag{1.5}$$

where n_s is the number of cells arranged in series, n_p is the number of cells arranged in parallel, V_{oc} is the open-circuit voltage, and R_0 is the equivalent resistance of the battery. R_0 varies as a function of the temperature and of the SoC (Figure 1.7). The effects of temperature on all the other parameters are neglected. For V_{oc}, this assumption is supported by experimental results [231], as evidenced in Figure 1.8. The internal resistance of the cell ($\mathcal{R}_i$) is

$$\mathcal{R}_i(t) = \Omega_{\text{cell}} R_0(t)\,, \tag{1.6}$$

being Ω_{cell} its volume. The heat generated per unit volume (q_{gen}) is determined through Equation (1.7)

$$q_{gen}(t) = \mathcal{R}_i(t)\frac{I(t)^2}{\Omega_{cell}^2} - \frac{I(t)}{\Omega_{cell}}T(t)\frac{\Delta S(t)}{\mathcal{F}}\,, \tag{1.7}$$

where $\mathcal{F} = 96485\,\text{C/mol}$ is the Faraday constant and ΔS is the entropy variation that is calculated as a function of the SoC through the experimental formulations presented in [232] and reported in Equation (1.8)

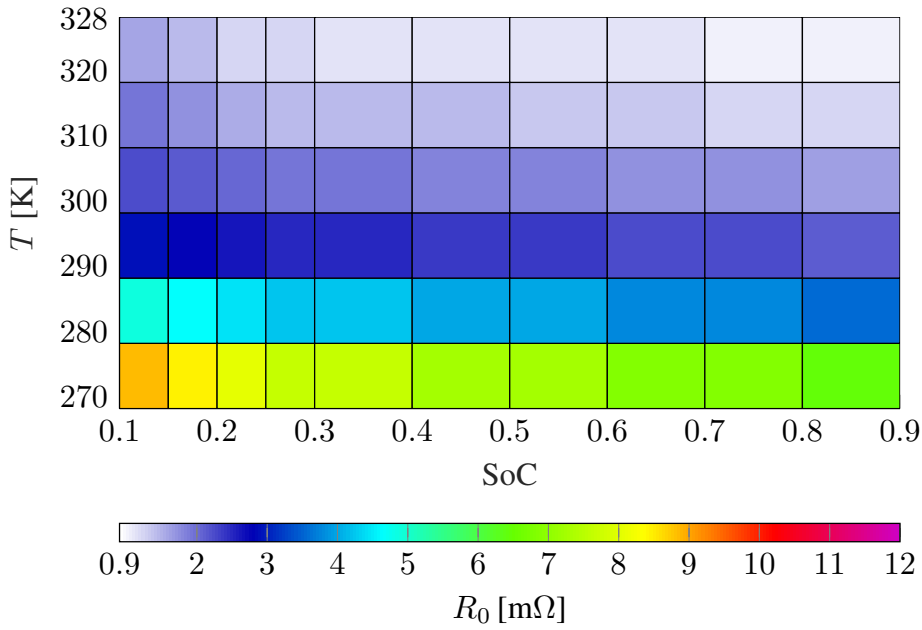


Figure 1.7: *Equivalent resistance of the battery as a function of the temperature and of the* SoC.

$$\Delta S(t) = \begin{cases} 99.88\,\mathrm{SoC}(t) - 76,67 & \text{if } 0 \leq \mathrm{SoC}(t) \leq 0.77 \\ -30 & \text{if } 0.77 < \mathrm{SoC}(t) \leq 0.87. \\ -20 & \text{if } 0.87 < \mathrm{SoC}(t) \leq 1 \end{cases} \tag{1.8}$$

The current $I(t+dt)$ is obtained as

$$I(t+dt) = \pm \frac{V_L(t) - \sqrt{V_L(t)^2 - 4P_{batt}(t)R_0(t)}}{2R_0(t)}, \tag{1.9}$$

where P_{batt} is the electrical power flowing in or out of the battery. The temperature of the battery $T(t+dt)$ is

$$T(t+dt) = T(t)\frac{q_{gen}(t) - \frac{q_{conv}(t)}{\Omega_{batt}}}{c_{p_{cell}}\,\rho_{cell}}, \tag{1.10}$$

where $c_{p_{cell}}$ is the specific heat capacity, ρ_{cell} is the density of the Li-Ion cell, Ω_{batt} is the volume occupied by the cells within the battery pack, and

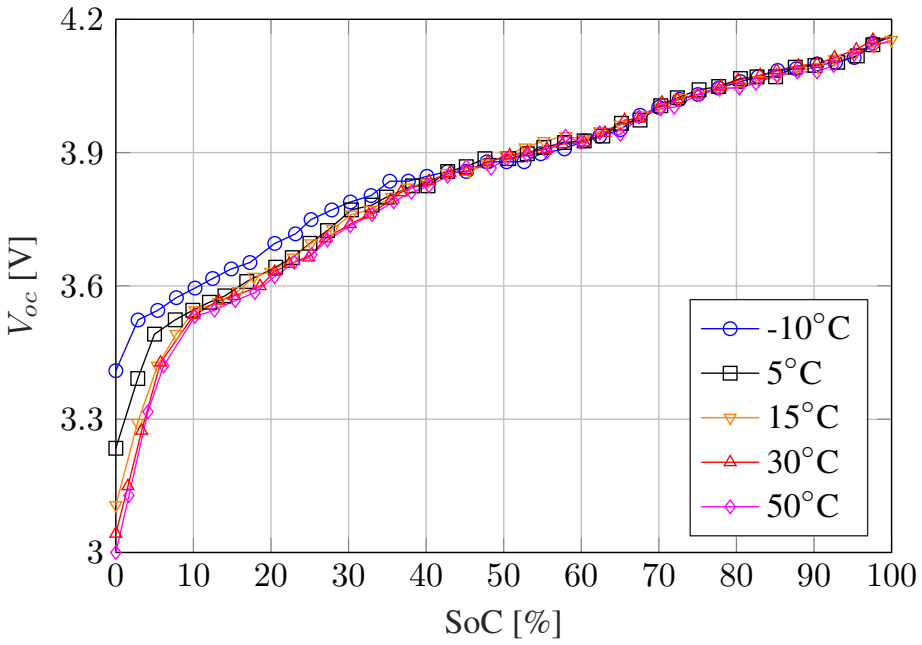


Figure 1.8: *Experimentally validated open-circuit voltage curves as a function of the* SoC *for different temperatures [228].*

q_{conv} is the heat exchanged by natural convection at the battery surface (A). Specifically

$$q_{conv}(t) = hA[T(t) - T_{\infty}]\,, \tag{1.11}$$

being h the convective coefficient and T_{∞} is the environment temperature. Leveraging on the geometry of the Nissan Leaf battery pack [233], we calculate A assuming an effective pack volume equal to $4\,\Omega_{batt}$. We estimate the $\mathrm{SoC}(t+dt)$ through the following Equation

$$\mathrm{SoC}(t+dt) = -\frac{I(t+dt)}{Q_{nom}}\eta_c + \mathrm{SoC}(t)\,, \tag{1.12}$$

where η_c is the Coulomb's efficiency [234] and Q_{nom} is the battery nominal capacity that varies as a function of the number of cells and their arrangement. To ensure correct operation and long battery life, and according to [235], companies like Hitachi, Saft and Solom recommend limiting the SoC variation to the range $0.1 < \mathrm{SoC} < 0.9$.

The model is implemented in the Matlab Simulink computational environment. Each simulation requires few seconds on a state-of-the-art desktop computer (intel-i7 8^{th} generation, 16 Gb RAM).

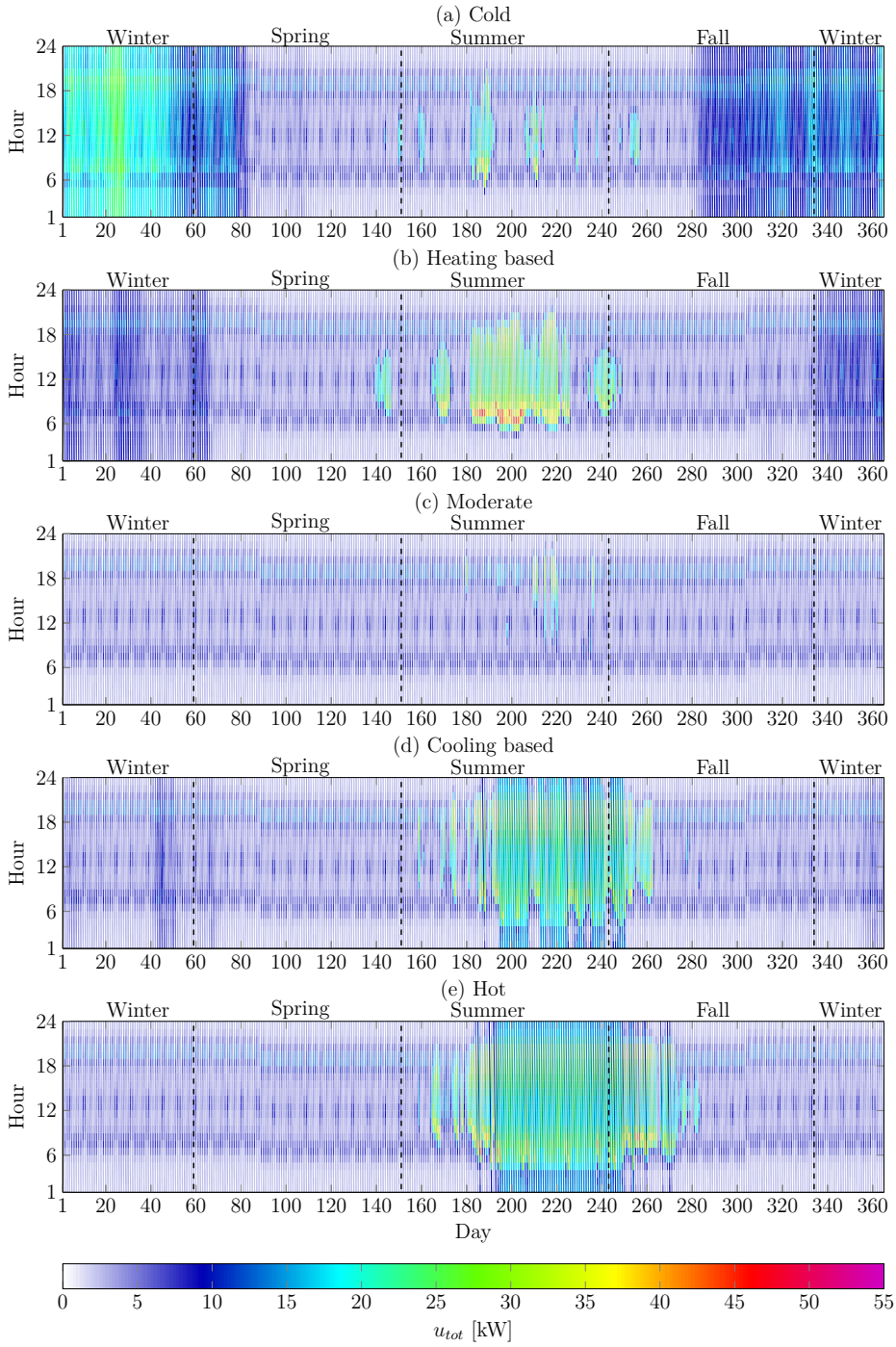


Figure 1.9: *Total building energy consumption as a function of time for (a) Cold climate; (b) Heating based climate; (c) Moderate climate; (d) Cooling based climate; (e) Hot climate. Numerical data can be found at 10.5281/zenodo.5816951.*

1.3 Results and discussion

1.3.1 Results

Table 1.5 reports the relevant consumption properties for each climate. In literature, the total annual energy consumption per unit area ($\mathbf{u}_a$) is often retrieved through building simulation models implemented in EnergyPlus, and ranges from a minimum of 30.24 kWh/m^2 [236] to a maximum of 88.67 kWh/m^2 [237]. We comment that, our results, are consistent with this range for all the considered climates.

Climatic Zone	U_{el} [kWh]	U_h [kWh]	U_c [kWh]	$\mathbf{u}_a$ [kWh/m^2]
Cold	42856	38028	3886	64.51
Heating Based	42856	7099	15426	49.76
Moderate	42856	813	1567	34.42
Cooling Based	42856	2132	28486	55.92
Hot	42856	820	37779	61.99

Table 1.5: *Building energy consumption for each climate.*

Figure 1.9 shows u_{tot} as a function of time for the five considered climates. We observe that in the cold climate the highest consumption is in winter whereas in the hot climate it is in the summer and at the beginning of the fall period. The heating based and cooling based climates exhibit similar trends and air conditioning during the summer is a relevant energy expenditure in both cases. In the heating based climate, consumption in the winter period is, as expected, higher than in the cooling based climate. Finally, for the moderate climate demand is constant throughout the year without significantly dominant periods unlike the other four.

Table 1.6 reports the relevant model results for the photovoltaic system. Therein, the renewable energy penetration factor is defined as $F = E_{pv}/U_{tot}$, where $U_{tot} = U_{el} + U_h + U_c$. We comment that $F < 1$ for all climates, except for the moderate one. For this particular type of climate, E_{pv} exceeds U_{tot}.

For each climate we study the annual behavior of the system for $n = 12$ different battery capacities: $Q_{nom,i} = [0\,\text{kWh (no battery)}, 40\,\text{kWh}, 50\,\text{kWh}, 60\,\text{kWh}, 70\,\text{kWh}, 80\,\text{kWh}, 100\,\text{kWh}, 120\,\text{kWh}, 140\,\text{kWh}, 160\,\text{kWh}, 215\,\text{kWh}, 270\,\text{kWh}]$. Specifically, we seek to assess the optimal capacity of the BESS to promote the local self-consumption of the PV energy by

Climatic Zone	E_{pv} [kWh]	F	P_{max} [kW]
Cold	40699	0.48	32.91
Heating Based	57434	0.88	32.72
Moderate	65856	1.46	34.75
Cooling Based	62404	0.85	34.30
Hot	64832	0.80	33.25

Table 1.6: *Relevant properties of the PV system as a fucntion of climate.*

filling the time lag between demand and production. To this aim, Figure 1.10(a) represents the self-consumed energy (E_s), that is the energy produced by the photovoltaic system effectively used to satisfy the consumption of the residential building, as a function of the relative battery capacity Θ, defined as

$$\Theta = \frac{Q_{nom}}{P_{max}}\,, \tag{1.13}$$

being P_{max} the maximum power of the PV. Note that P_{max} differs from the P_{peak} (Table 1.6).

E_s is a significant parameter both from an energy and system point of view. In fact, it should be maximized to enhance the value of locally produced energy, to minimize grid issues related to renewable energy sources fluctuations, and to minimize energy losses. As expected, the cold climate has the lowest E_s, having the lower E_{pv}. Conversely, the hot climate being characterized by a high E_{pv} and a high U_{tot} has the highest E_s. The moderate climate has the highest E_{pv} but also the lowest U_{tot}. Therefore its E_s is relatively low.

Despite in Figure 1.10(a) all the curves relative to different climates qualitatively exhibit the same trend, the different max(E_s) associated to each climate hinders a general analysis of the battery electricity storage impact.

The same results are reported in Figure 1.10(b) through a different parameter space that gathers more insights into the BESS optimal sizing. Specifically, we define the relative variation of self-consumed energy (λ) as

$$\lambda_i = 100 \times \frac{E_s(Q_{nom,i}) - E_s(Q_{nom,i-1})}{E_{pv}}\,. \tag{1.14}$$

Notably, in Figure 1.10(b), the patterns relative to all climates collapse on the same trend allowing a general analysis of the battery storage optimal

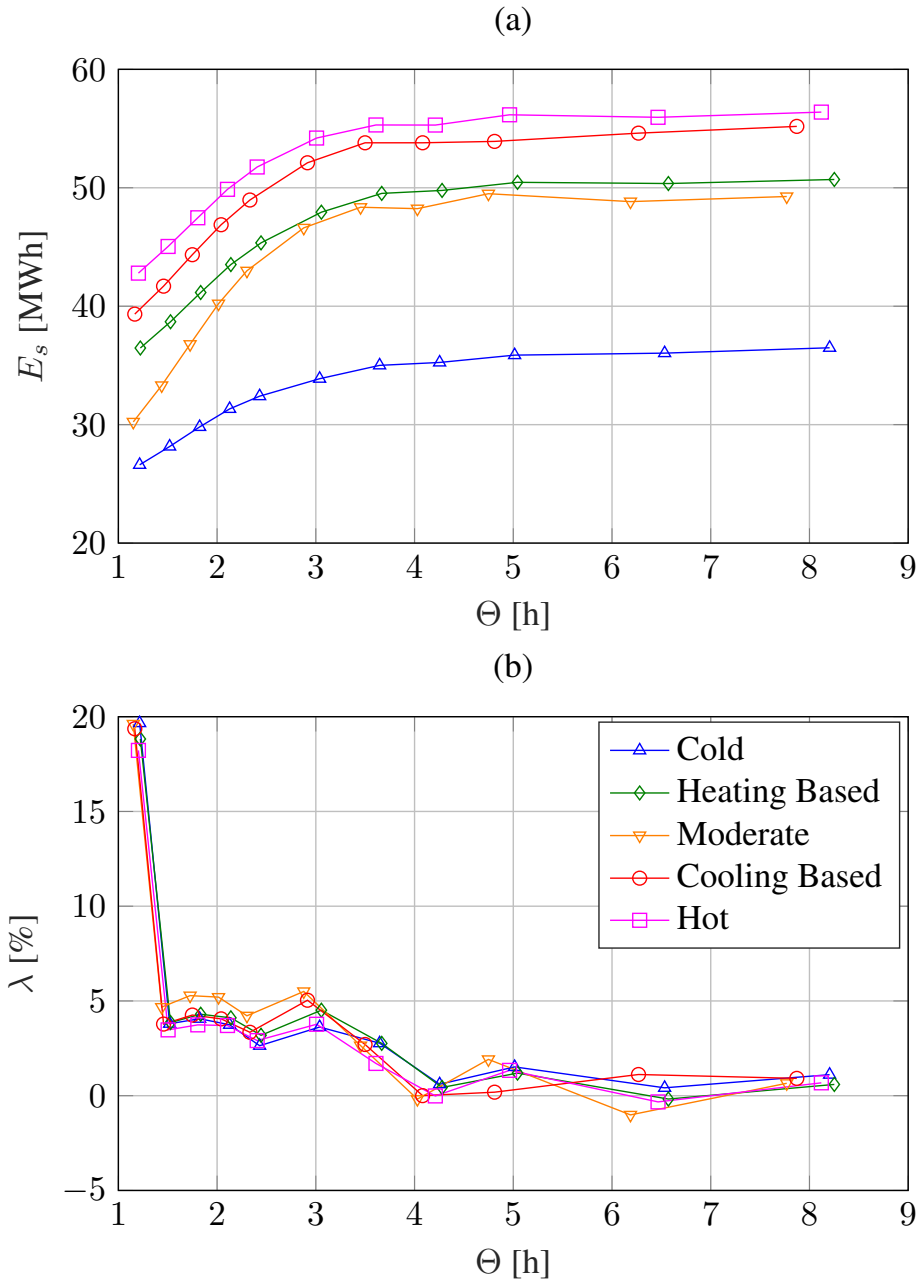


Figure 1.10: *(a) Self-consumed energy as a function of* Θ*; (b)* λ *as a function of* Θ*.*

sizing and operation. For all the climates, λ is a decreasing function of Θ. On average, $\lambda \simeq 20\%$ for $\Theta = 1.2\,\text{h}$. Such a figure suddenly drops to $\lambda \simeq 5\%$ for $1.5\,\text{h} < \Theta < 3\,\text{h}$. After a relatively flat pattern for $1.5\,\text{h} < \Theta < 3\,\text{h}$, λ reduces to negligible values for $\Theta > 4\,\text{h}$. In summary, $\Theta > 4\,\text{h}$ is not recommended in terms of capacity of the battery storage to increase the renewable energy self consumption while $\Theta = 3.5\,\text{h}$ can be safely considered an energy-system optimal solution. As a consequence, BESS is suitable to fill the daily temporal discrepancy between production and demand. Conversely, seasonal electricity storage would require much larger Θ not gathering significant benefits in terms of self-consumed renewable energy. Figure 1.10(a) shows that E_s reaches a plateau as Θ increases. For all climates, such a plateau is below E_{pv} evidencing that a portion of the locally produced renewable electricity is always fed to the grid (even for large Θ). Such an energy varies between 4200 kWh (cold climate) and 16500 kWh (moderate climate) and could be stored for later use by exploiting other storage systems.

In 2020, the average cost of the electricity withdrawn from the grid in Europe, was $c_e = 0.2134\,€/\text{kWh}$, including all taxes and levies [238]. Being C_w the total yearly cost of energy withdrawn from the grid, we define γ as

$$\gamma = 100 \times \frac{C_w(Q_{nom,i}) - C_w(Q_{nom,i-1})}{E_{pv} c_e}. \tag{1.15}$$

Figure 1.11(a) reports γ as a function of Θ showing a similar trend compared to λ (Figure 1.10(b)). Also in this case, $\gamma \simeq -20\%$ for $\Theta = 1.2\,\text{h}$ then the curves flatten almost immediately around zero after a short plateau around -5%. In 2010, Li-Ion battery pack prices were above 1100 \$/kWh and have fallen to 137 \$/kWh in 2020 (89% reduction in real terms) [86]. This is equivalent to $c_b = 112.65\,€/\text{kWh}$, according to the 2020 reference exchange rates [239]. By 2023, the average prices will be close to 100 \$/kWh, according to the latest forecast by BloombergNEF (BNEF) [86]. In this economic analysis that focuses on the interaction between residential building, battery, and grid, we assume that the energy fed into the grid is not paid for. In fact, its economic value is dominated by country-specific subsidiary mechanisms that would hinder a general analysis. Moreover, battery energy storage system should have the objective to maximize the self-consumption of locally produced renewable energy. Such an objective would be put in background by very generous subsidiary mechanism for the electricity eventually sold to the grid.

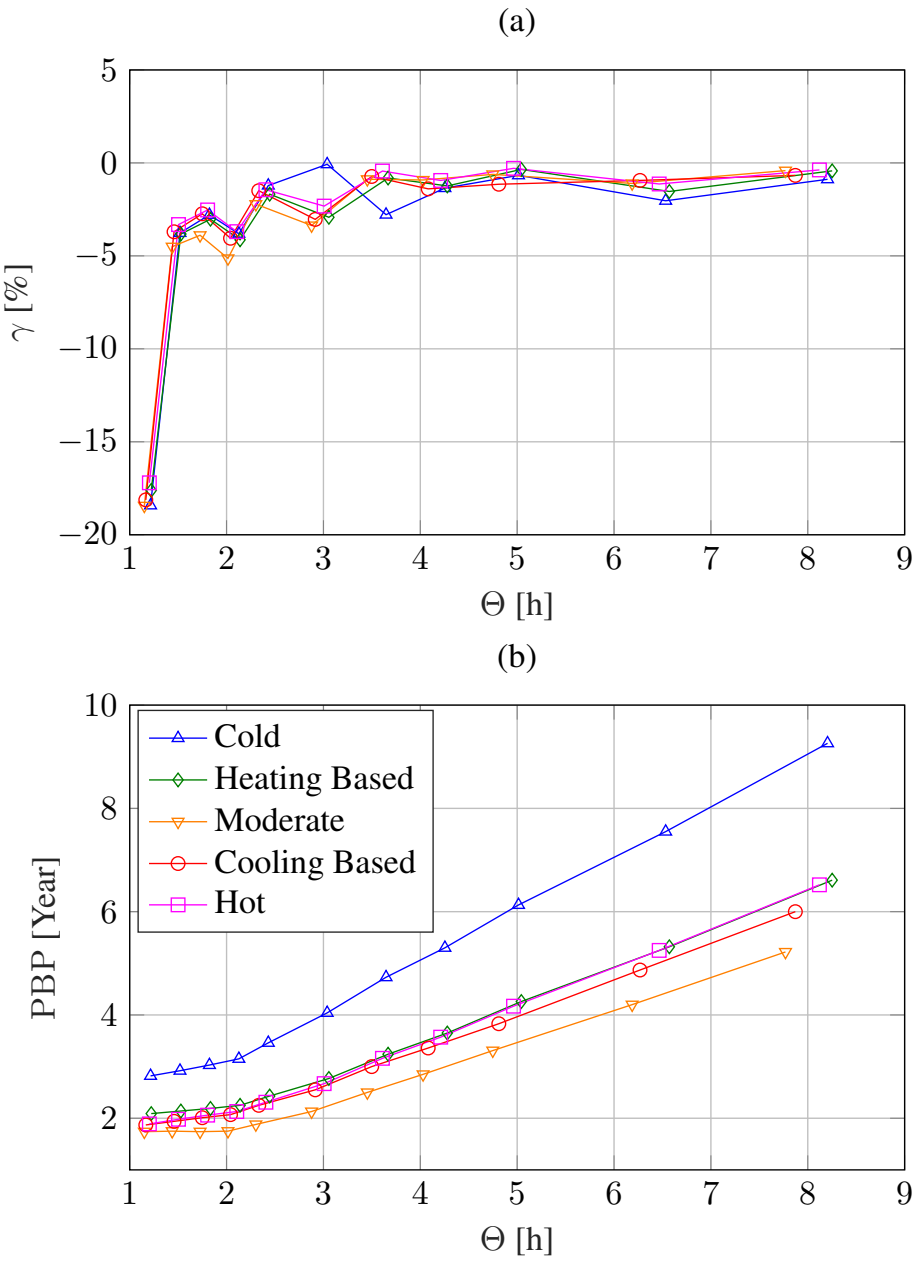


Figure 1.11: *(a) γ as a function Θ; (b) PayBack Period as a function of Θ.*

To evaluate the feasibility of the BESS investment, we analyze the Pay

Back Period PBP

$$\mathrm{PBP} = \frac{I_i}{S_a}\,, \tag{1.16}$$

where $I_i = Q_{nom}\, c_b$ is the initial investment for the battery and S_a is the annual saving due to the reduction of the energy withdrawn from the grid generated by the BESS. Figure 1.11(b) shows PBP as a function of Θ for all the climates. The moderate climate has the lowest PBP while the cold climate has the highest one. The other three climates have approximately the same PBP. We observe that PBP grows almost linearly for $\Theta > 2\,\mathrm{h}$ because the initial investment for the battery dominates compared to S_a. For $\Theta \simeq 3.5\,\mathrm{h}$, PBP is between 2.5 years (moderate climate) and 4.7 years (cold climate). Therefore, using λ curves to optimally size the battery returns a sustainable investment for all climates. Conversely, using the BESS for seasonal storage is unsustainable either with current batteries costs nor with those reasonably foreseeable in the short-medium term.

1.3.2 Discussion

Besides determining the optimal techno-economic size of the battery, our methodology allows to dissect its operation as a function of the climatic conditions.

We first consider the average BESS Charge (SoC_m) as an indicator of the system utilization factor. Comparing Table 1.7 to Figure 1.11(b) we observe that SoC_m correlates with the climatic variation of PBP. Specifically, the pay back period is inversely proportional to SoC_m. Cold and Moderate climates have the lowest and highest SoC_m, respectively. This is coherent with their PBP trends (Figure 1.11). Conversely, heating based, cooling based, and hot climates have similar SoC_m and their pay back period curves collapse on the same pattern (Figure 1.11). Such an analysis supports the conclusion that, for nZEB applications, BESSs are not suitable for seasonal storage. In fact, long term storage requires large capacities but the SoC_m decreases as Q_{nom} increases, consequently yielding a larger pay back period. Similar results are obtained in [73] that shows that the investment cost steadily rises with battery size, and that PBP is shorter for smaller capacity systems. In addition to this, our results provide a general criterion for the techno-economic optimization of the BESS capacity.

The pay back period also correlates to the share of the building demand fulfilled by local RES, $\Xi = E_s/U_{tot}$, (Table 1.7) as highlighted in

Climatic Zone	SoC_m	E_s/U_{tot}
Cold	0.29	0.41
Heating based	0.37	0.76
Moderate	0.53	1.00
Cooling based	0.39	0.73
Hot	0.40	0.68

Table 1.7: *Average annual State of Charge and renewable electricity self consumption for* $\Theta = 3.5\,h$.

[75]. Therein, it is shown that BESSs are highly profitable when the combination between the supply and the demand allows a significant increase of energy self-consumption. Similarly, we found that larger Ξ positively impact the PBP (Table 1.7). The imbalance between PV production and building demand

$$D = |P_{pv}(t) - u_{tot}(t)|\,, \tag{1.17}$$

largely determines the battery operation, the λ and γ values, and, finally, the battery optimal capacity. D exhibits the same frequency histogram for all the climates (Figure 1.12). As a consequence, the temporal mismatch between the P_{pv} and u_{tot} is similar for all the climates, despite they have different F values (Table 1.6). All diagrams exhibit a major frequency peak for $D \simeq 3\,\mathrm{kW}$ generally followed by a lower peak for $10\,\mathrm{kW} < D < 15\,\mathrm{kW}$. This, explains the patterns reported in Figure 1.10 and 1.11 suggesting also that F has a minor impact on the BESS operation. In fact, the optimal sizing of the battery is related to the temporal mismatch between P_{pv} and u_{tot}, and by the D frequency diagram. On the contrary, F compares the total energy produced by the renewable energy sources to the nZEB yearly demand, but does not provide information nor on their instantaneous difference nor on their discrepancy in time.

To this end, Figure 1.13 shows the SoC as a function of time for all the climates and for $\Theta = 3.5\,\mathrm{h}$. Generally, the battery is most likely to reach a high state of charge in transitional seasons when u_{tot} is commonly lower than P_{pv} (Figure 1.9). Specifically, in cold climate, the BESS is discharged for all winter and part of fall and spring, when the SoC is steadily about 10% and without significant cycling (Figure 1.13(a)). In the rest of the year, the SoC exhibits a clear daily cycling with relatively large values during the central part of the day. In fact, in this climate, u_h prevails over

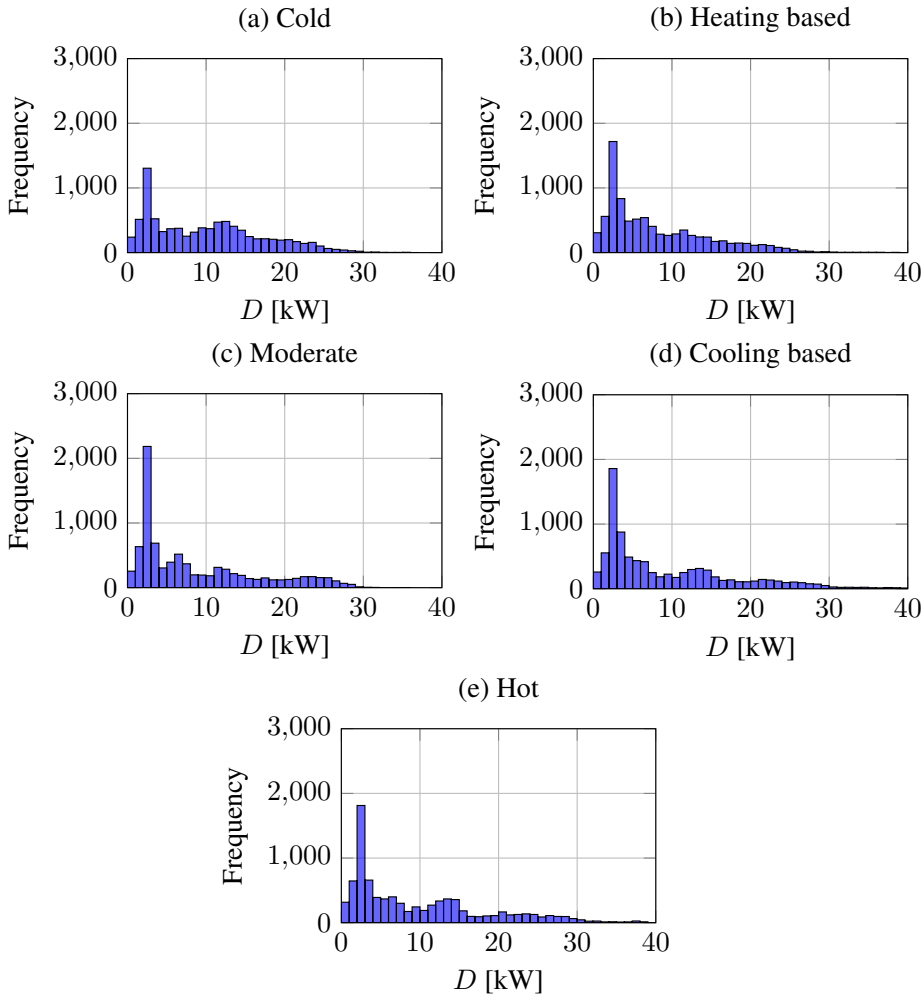


Figure 1.12: *D Frequency histograms: (a) Cold climate; (b) Heating based climate; (c) Moderate climate; (d) Cooling based climate; and (e) Hot climate.*

the other demands causing a large energy demand in the colder periods (Table 1.5). As a result, the battery is unused for about 100 days per year, concentrated in colder seasons. This further explains why the cold climate has the largest PBP: the low SoC_m results from a relatively long period of BESS disuse (about 1/3 of the year), rather then from and average low SoC. As a consequence the pay back period is 1/3 longer than the average of other climates (Figure 1.11(b)).

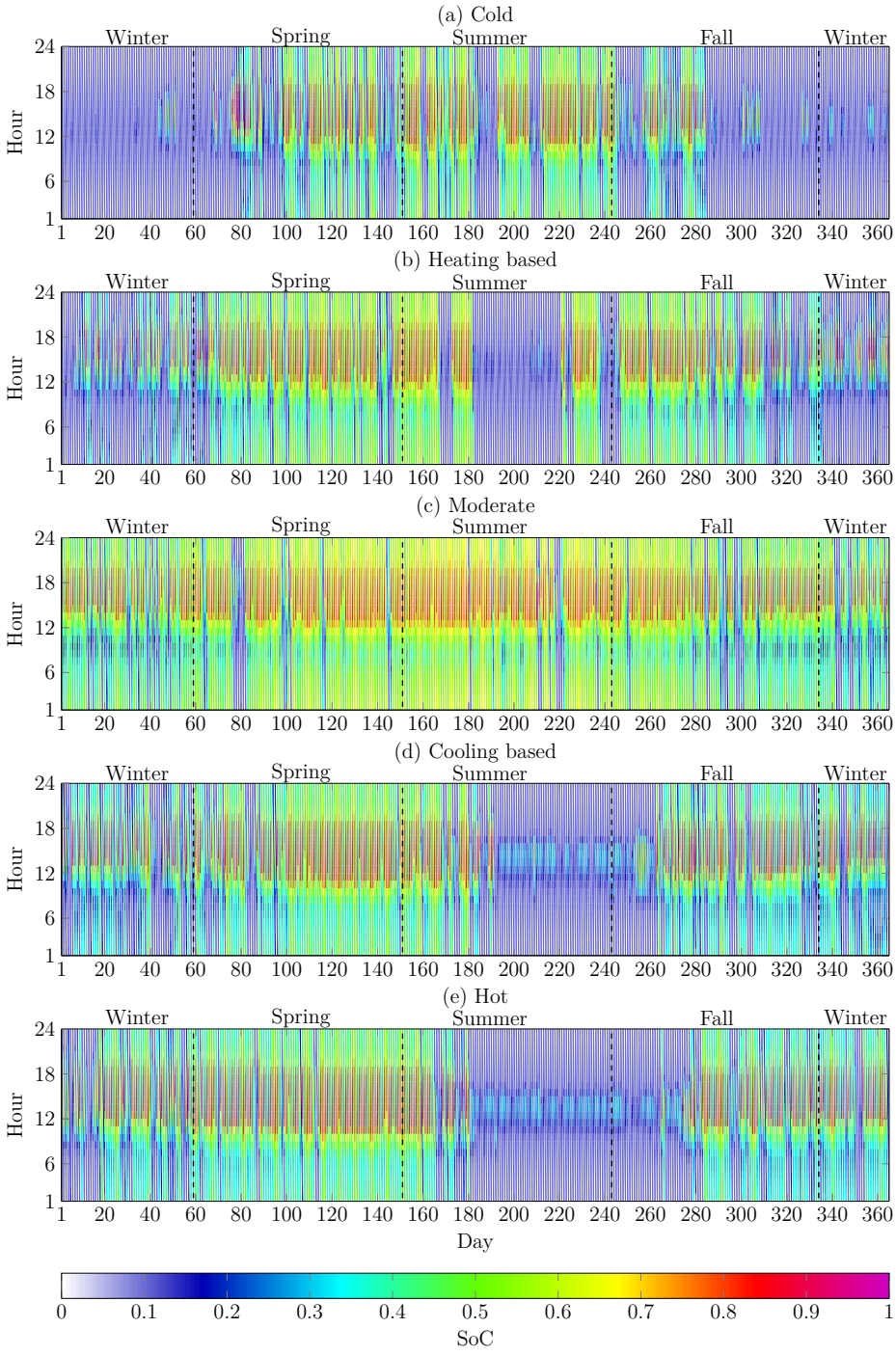


Figure 1.13: *State of Charge of the Li-Ion battery as a function of time for (a) Cold climate; (b) Heating based climate; (c) Moderate climate; (d) Cooling based climate; (e) Hot climate.*

In heating based climate (Figure 1.13(b)), the BESS has a steadily low SoC only for less than 30 days during summer. For the rest of the year there is a clear daily SoC cycling, indicating that the battery is effectively used to match photovoltaic production and nZEB demand. The highest SoC occurs during fall and spring, when it generally varies between 50% and 90%. In winter the state of charge is lower, in particular during late night and before noon. However, during such a cold season, the SoC varies between 10% and 90% showing a deeper cycling compared to warmer seasons. Only during transitional periods, SoC is consistently high at the evening, and energy is transferred to the following morning. The summer disuse period, causes such a climate to have the second longest PBP (Figure 1.11(b)).

In moderate climate the BESS has almost the same behavior throughout the whole year (Figure 1.13(c)). It is charged during the central hours of the day, reaching high state of charge and then discharged in the evening and during the morning. The SoC cycles between 35% and 90% during hot and transitional seasons, and between 10% and 90% during cold periods. At night, generally, SoC $> 40\%$ and residual energy is used during the subsequent morning. As a consequence the minimum state of charge locates at late morning (just before noon). This is particularly evident for the colder periods, when the PV production is lower in particular at morning.

In cooling based climate, the BESS is always used. In fact, even during summer, when SoC $< 40\%$ for about 60 days, Figure 1.13(d) evidences daily a SoC cycling. State of charge is always maximum after noon. During transitional seasons, residual SoC in the evening (SoC $> 50\%$), is used to satisfy the demand in the morning. Conversely, during summer, at night the battery is already completely discharged due to the large cooling energy demand (Figure 1.9). Cold periods, exhibit a more variable behavior where SoC at the evening varies between 10% and 40%. Overall, such a battery usage pattern returns the second shorter pay back period (Figure 1.11(b)).

Hot climate exhibits a SoC pattern similar to cooling based climate. Yet, the hot season is much longer and the state of charge remains below 40% for about 100 days. This reduces the effectiveness of the battery and yields a longer PBP, similar to that of the heating based climate.

SoC patterns show that the BESS never consistently charges during one season and discharges during another. Rather, it is always character-

ized by a daily state of charge cycling. This is consistent with and supports the results of Figure 1.10(b) and 1.11(b). Therein, $\Theta = 3.5\,\mathrm{h}$ was identified as the optimal techno-economic size for the battery that qualifies as a daily storage solution for nZEB (see also [72, 73] for similar conclusions). In fact, the BESS allows matching the PV production and nZEB demand within a day (Figure 1.13). Notably, such optimized battery storage increases the percentage of the nZEB energy consumption supplied by RES by roughly 50%. Similar results are also reported in [76] for different RES scenarios in typical high-rise building in Hong Kong. Moreover, our results allow analyzing how the BESS impact the RES consumption share for diverse climates. Specifically, the hot climate shows the largest increment (56%), the cold, heating based and cooling based climates are all close to 50%, whereas the moderate climate exhibits the lowest one (35%). In the moderate climate, the low increment is explained considering that for $\Theta = 3.5\,\mathrm{h}$ PV already completely fulfill the energy demand.

Results show that building level electricity storage cannot completely match production and demand.Other technologies (i.e. grid or sub-grid level storage) are required to further increase the self consumption share of the locally produces renewable energy. Electric mobility is one of such technologies. The Nissan Leaf consumes $20.6\,\mathrm{kWh}/100\,\mathrm{km}$ [240]. In Europe, the average daily distance traveled by a car is about 33 km [241], that results in an average energy required to recharge a car of about 2481 kWh per year. Therefore, the PV energy that cannot be locally used, could be exploited to fully recharge from a minimum of 2 vehicles (cold climate) to a maximum of almost 7 vehicles (moderate climate). The emission limits for a EURO 6 diesel vehicle are $g_{CO_2} = 95\,\mathrm{g/km}$ [242], $g_{CO} = 0.5\,\mathrm{g/km}$ [243], $g_{NO_x} = 0.08\,\mathrm{g/km}$ [243], $g_{PM} = 0.005\,\mathrm{g/km}$ [243]. Thus, this solution would avoid the release into the atmosphere of a minimum of about $G_{CO_2} = 1945\,\mathrm{kg/year}$, $G_{CO} = 10\,\mathrm{kg/year}$, $G_{NO_x} = 1.6\,\mathrm{kg/year}$, $G_{PM} = 0.1\,\mathrm{kg/year}$ (cold climate) to a maximum of about $G_{CO_2} = 7815\,\mathrm{kg/year}$, $G_{CO} = 41\,\mathrm{kg/year}$, $G_{NO_x} = 6.6\,\mathrm{kg/year}$, $G_{PM} = 0.4\,\mathrm{kg/year}$ (moderate climate). Vehicle energy storage, can be effectively integrated into the nZEB as demonstrated in [244].

1.4 Summary

In this chapter we assess a climate independent scaling law for the optimization of a BESS in a residential environment. We evaluate the

environmental and economic impact of the integration of a Li-Ion battery based electricity storage in a real existing nZEB, for five different climates and for different battery capacities. We optimize the system control in order to maximize the share of self consumed renewable energy for all configurations. We model the demand of the residential building for each climate through the "EnergyPlus" software. We determine the PV production with the "PVGIS" platform. In addition, we model the Li-Ion battery trough the zero-th order equivalent circuit presented in [228]. Consumption data are validated against measured energy demands.

We leverage on such data and models to carry out a techno-economic analysis of battery integration for five different climates and for twelve different battery capacities. We evaluate the self-consumed energy, his relative variation and the relative variation of the cost of energy withdrawn from the grid, as a function of the relative battery capacity. These representations correlate all the most significant energy quantities of the plant.

The results highlight that a relative battery capacity $1.5\,\mathrm{h} < \Theta < 3.5\,\mathrm{h}$ is the best solution from an energy and economical point of view. We observe that the selected design criterion yields a PBP between 1.8 years (moderate climate) and 4.7 years (cold climate). In conclusion, such an investment is sustainable and gathers significant advantages both on an energy and environmental level, for all the climates analyzed.

The methodology is also used to dissect the hourly operation of the optimized battery. This analysis, demonstrates that, in the nZEB scenario, the BESS qualifies as a daily storage system. In fact, allows matching the photovoltaic production and building consumption on a daily basis. Conversely, the battery never consistently charges during one season and discharges during another.This highlights the possibility/necessity to combine BESSs with different technologies, possibly grid or sub-grid level storage. Electric vehicles could effectively be one of such technologies.

In our vision, the presented framework is a valuable tool for the preliminary design of batteries in buildings. On the one hand, the design of such systems should leverage on instantaneous energy consumption and production data. On the other hand the scaling laws presented in Figure 1.10 and 1.11 greatly simplify BESSs sizing requiring only the maximum renewable energy sources production as input. Designing BESSs according to the results herein presented yields both a sustainable investment and an effective solution in terms of RES exploitation and limitation of

grid issues. Moreover, the battery and nZEB models, are valuable tools for policy makers to determine pricing policies that optimize specific objective functions such as to maximize the renewable energy sources exploitation. A further feasible application is utilizing the proposed battery model for the design of the battery. In fact, such model allows selecting the number of the cells, their connection (number of cells in parallel and in series), the battery volume, and cooling surface. To this end, the model could be ameliorated by implementing a more detailed thermal management. So far, battery self-discharge has been discarded. Its impact on the present results is negligible due to the low storage duration. However, such a phenomenon should be considered for longer (i.e. seasonal) storage. Finally, our results leverage on a rule based strategy for system control. Using an optimized strategy could further improve the framework effectiveness.

Chapter 2

Assessment of residential energy communities integrating an electric vehicles charging system

Electric vehicles (EVs) are expected to significantly reduce the environmental footprint of mobility and are one of the key elements of the current energy transition. However, several obstacles hamper the electric mobility take over, above all the limited diffusion of adequate charging infrastructures.

Although in literature there are methodologies to optimize the EVs charge in various aspects, a comprehensive peer-to-peer charging strategy exploiting the existing infrastructure in a building environment has not still been proposed, to the best of our knowledge. Therefore, in this chapter we develop a condominium system for shared charge of EVs implementing a rule-based logic and a pricing policy aimed at the intelligent use of the available energy and existing infrastructures. Such a system could be an essential component of energy communities because it allows to minimize both the EVs charging cost and the grid infrastructural investment by valorizing the unused portion of the electrical power installed in the building, and the photovoltaic plant. Moreover, by reasonably exploiting such an energy the impact on the existing electrical grid could be reduced. After describing the methodology, we assess the effectiveness of the system in realistic case studies, using measured data from: (i) the

ECO data-set [245] for energy consumption, (ii) the passenger car travel survey for vehicles usage [246], and (iii) PVGIS [247] for local renewable energy production.

The chapter is organized as follows. In Section 2.1 we present the problem statement. Section 2.2 describes constituent parts of the system, its control logic and the implemented methodology. Case studies and results are presented and discussed in Sections 2.3 and 2.4. Finally, we draw the conclusions of the work in Section 2.5.

2.1 Problem Statement

The aim of this chapter is to conceptualize, design, and prototype a condominium system for shared charge of electric vehicles implementing a logic and a pricing policy nudging the rational use of the available energy and existing infrastructures. In particular, the logic implemented in the charging infrastructure is based on a forecast part that allows the determination of realistic charging profiles and an actual charging part, in which energy is supplied to the vehicles. Such rule-based logic can be easily implemented in a real-time controller. Two charging strategies are available to the user: one that minimizes the charging cost, and one that minimizes the charging time.

In an energy community perspective, such peer-to-peer system minimizes the necessity of additional charging stations by exploiting the unused electrical power available in a residential building. In Figure 2.1(a) the grey area is the yearly electric energy load of an average apartment with 3 kW of installed power, as reported by the office of Energy Efficiency and Renewable Energy (EERE) [248]. Figures 2.1(b), (c), and (d) show the hourly load of the same apartment on the 200th day, 50th day, and 300th day representing respectively summer, winter, and transitional electrical energy loads. In the plots, the orange area represents the energy that is available to charge the vehicles being in excess to the apartment load. In detail, 15204 kWh per year are usable for vehicle charge, that is 57.9% of the total available energy. More precisely, the daily available energy for vehicles ranges from 23 kWh/day to 50 kWh/day.

Figure 2.2 represents the scheme of the proposed system highlighting all energy and data flows. The main components are: (i) the PhotoVoltaic system (PV), (ii) the Residential Building (RB), (iii) the Charge-Dedicated Electric Line (CDEL), (iv) the Charging System (CS), and (v) the

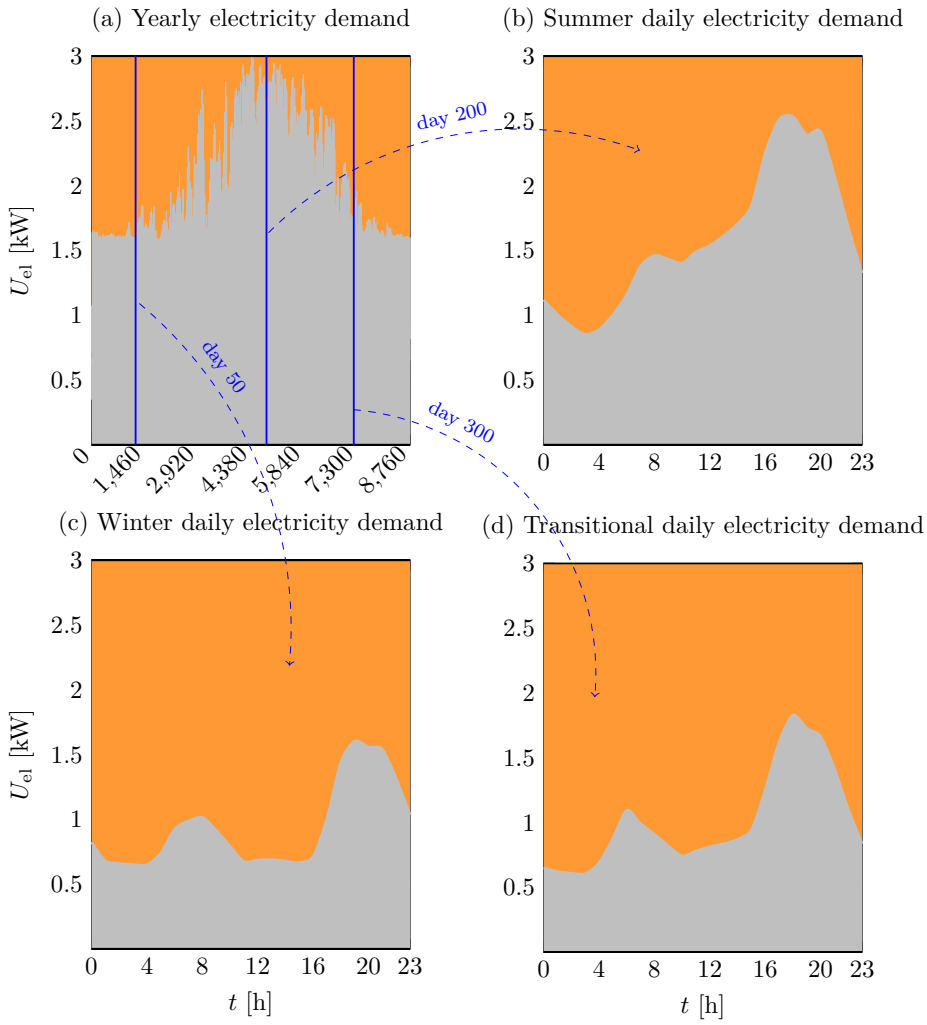


Figure 2.1: *Electric energy load in grey and unused electric energy in orange of an average apartment: a) yearly demand, b) demand of day* 200 *(summer), c) demand of day* 50 *(winter), and d) demand of day* 300 *(transitional). Data from the office of Energy Efficiency and Renewable Energy (EERE) [248].*

Electric Vehicles (EVs). The CS optimally manages three different energy sources following this priority order: (i) the photovoltaic, (ii) the residential building, and (iii) the charge-dedicated electric line. PV energy is primarily used to satisfy the demand of the apartments. The energy surplus can be used to charge EVs. Each of the apartments composing

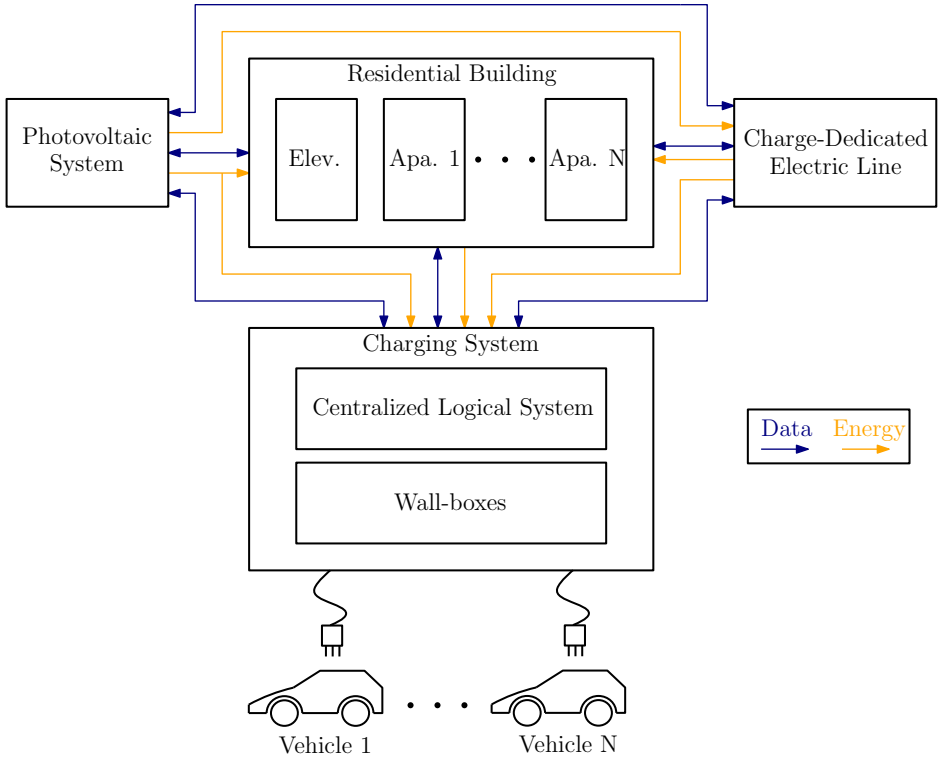


Figure 2.2: *Scheme of the main elements of the condominium system for shared charge of electric vehicles.*

the RB has an installed 3 kW electric line. Similarly, the elevator has 6 kW of installed power and it is activated $5 - 10$ times per hour. The energy load of the apartments and of the elevator is variable and often lower than the installed power. Therefore, the unused power is a source of energy for EVs charge that does not require an additional investment in infrastructure. Finally, the CDEL takes over when the energy that can be withdrawn from the PV and from the RB is not sufficient to meet the defined charging process.

2.2 Methodology

2.2.1 Charging System

The CS consists of a centralized logical system and of wall-boxes. The centralized logical system manages the continuous exchange of data and energy between the plant components. It allows to charge the connected EVs withdrawing in real-time the electricity from the PV, from the RB, and if necessary from the CDEL. It also manages the pricing associated with the charging process by considering the energy source and the power required. The purpose of this pricing policy is to nudge users to employ the CS responsibly (see Section 2.2.1.2).

Each EV can be connected to the CS through a wall-box, which is a wall-mounted device compatible with all electric car models. When a vehicle is connected it is necessary to set the car model, the finish time, and the remaining and desired State of Charge (SoC). Through forecast energy loads the CS determines if it is possible to successfully complete the required charging duty. In any case, the CS suggests alternative charging profiles associated with the forecast charging costs that the user can select. Once one of the different alternatives has been chosen, the vehicle charging process begins and the CS manages the energy flows based on the charging profile set and the SoC of the vehicle battery.

Therefore, the logic of the CS can be divided into a forecast part and an actual charging part. The first one allows the determination of realistic charging profiles, while in the second one the energy is supplied to the vehicles in real-time. These two parts interact with each other to ensure rational system operation.

2.2.1.1 Hardware

We design the hardware of the CS for the simultaneous charge of three vehicles (see Figure 2.3). System generalization to a larger cars number is straightforward. Moreover, our prototype is already able to evidence the advantages of energy sharing (see Section 2.4) The centralized logical system is implemented in NI® LabVIEW 2019. Such program runs on a workstation composed of: Intel® core i7-9700 @ 3.00 GHz CPU, RAM 16 GB and Intel® UHD Graphics 630 GPU. A USB cable connects the centralized logical system with each wall-box. The wall-boxes are commercially available models (NEMA® 14-50 - 42 A, OpenEvse, see Figure

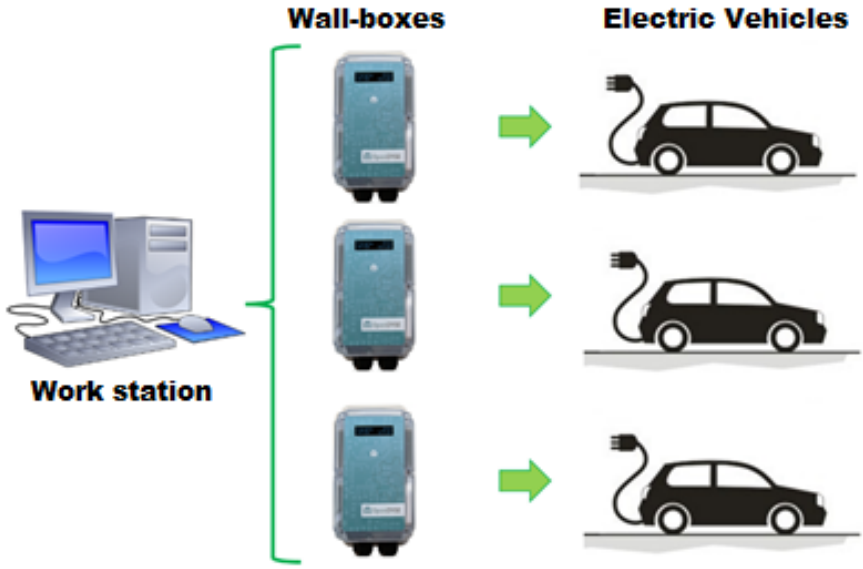


Figure 2.3: *Structure of the hardware of the charging system.*

2.4). Each wall-box can supply from a minimum of 1.32 kW (6 A - 220 V) to a maximum of 9.24 kW (42 A - 220 V) to a single vehicle. Each wall-box is equipped with an interactive LCD display and a SAE J1772 cable that guarantees the compatibility with all the modern vehicles. The display provides live power usage, state information (current to supply, current absorbed by the vehicle, energy to supply), and quick access to settings. The centralized logical system regulates the power by controlling the current according to the users' requirement. The system as a whole meets the prescriptions of the IEC Standard.

2.2.1.2 Software

Forecast charge Once an electric vehicle is connected, the CS estimates the charging dynamics following the logic shown in Figure 2.5 and considering the presence of other EVs already in charge. To this aim, the CS uses forecast energy loads of the building, and the PV production profiles on a 15-minutes base.

The user inputs several data of the EV: (i) the model (i.e the battery capacity), (ii) the initial and required final SoC, and (iii) the time by which the charging process has to finish. Based on these data, the CS informs the



Figure 2.4: *Wall-box: NEMA® 14-50 - 42 A, OpenEvse.*

user whether it is possible or not to complete the required charging procedure. In case of feasible charging schedule, the CS eventually provides the possibility to choose an alternative process that minimizes the cost by extending the charging time. For both the alternatives the CS forecasts the charging cost. On the other hand, if the required charging schedule is not feasible, the user can choose whether to cancel the operation or to: (i) finish the charging process at the established time without reaching the required SoC, (ii) meet the required SoC in the minimum possible time, or (iii) meet the required SoC with the minimum possible cost.

To administrate the energy demand responsibly, and to discourage the CDEL use, the system forecasts the charging cost as a function of the power required and of the energy source. In particular, we assume that the cost of the electric energy withdrawn from the residential building sc_{RB} is equal to 0.18 €/kWh being such value the average calculated in the period 2010-2020 for the Italian market [249]. Such market is representative of the overall European (EU28) context [250]. Following the pricing logic previously explained, we also assume that the electricity withdrawn from the CDEL is 40% more expensive of the energy from the apartment. Table

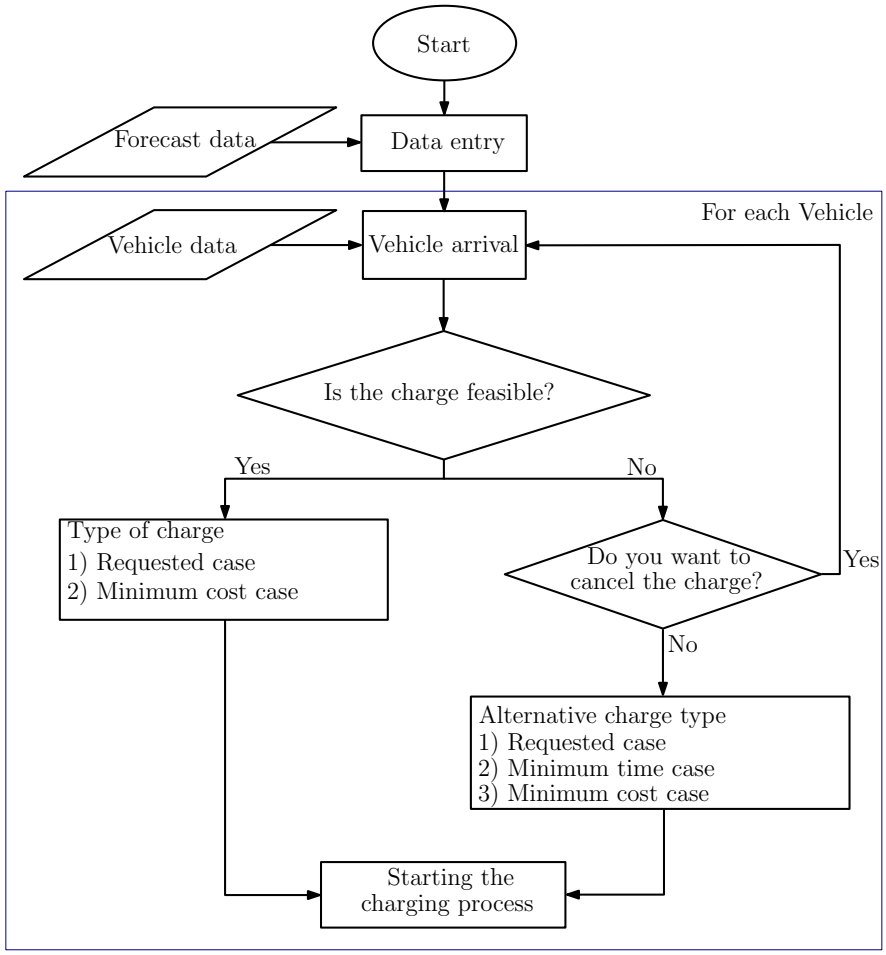


Figure 2.5: *Logical structure of the charging system for the forecast part.*

2.1 summarizes the specific energy costs assumed.

	Source	€/kWh
sc_{PV}	Photovoltaic System	0.06 €/kWh
sc_{RB}	Residential Building	0.18 €/kWh
sc_{CDEL}	Charge-Dedicated Electric Line	0.25 €/kWh

Table 2.1: *Specific energy costs based on the source.*

Specifically, the forecast cost of the vehicle charging process for a quar-

ter of an hour C_Q is defined as follows

$$C_Q = X \sum_{j=1}^{3} (sc_j E_j) = X(C_{\mathrm{PV}} + C_{\mathrm{RB}} + C_{\mathrm{CDEL}}), \tag{2.1}$$

where X is a multiplication factor that ranges between 1 and 2, sc_j is the specific energy cost of the j^{th} source, E_j is the energy withdrawn from the j^{th} source, C_{PV} is the cost of energy taken from PV, C_{RB} is the cost of energy taken from RB, and C_{CDEL} is the cost of energy taken from the CDEL. Considering E_w as the total energy that can be withdrawn from the charging system, E_d as the energy drawn

$$E_d = \sum_{j=1}^{3} E_j, \tag{2.2}$$

and α the number of EVs, the definition of X is

$$\begin{cases} X = 1 & \text{if } E_d \leq \frac{E_w}{\alpha} \\ 1 < X < 2 & \text{if } E_d > \frac{E_w}{\alpha} \\ X = 2 & \text{if } E_d = E_w \end{cases}. \tag{2.3}$$

X is directly proportional to the energy drawn and aims at discouraging excessively fast charges for which it is necessary to use a a big amount of the available energy. In fact, if all the energy available in a given period of time is used to charge a single EV then it will not be possible, in the same period of time, to charge other EVs. Such a behavior is inappropriate for peer-to-peer energy sharing system. Finally, the expected total cost associated with the charge of a vehicle C_{tot} can be defined as the sum of the forecast costs C_{Qi} relating to all the N quarters of an hour composing the charging process

$$C_{tot} = \sum_{i=1}^{N} C_{Qi}. \tag{2.4}$$

Actual charge Once the user chooses the charging schedule for the EV, the CS starts the charging procedure and monitors the energy and data flows from the various elements of the system (see Figure 2.6). In this phase, the user can control the charging progress through the SoC and the effective cost of charge. At the same time, the owner of each apartment can limit the energy flow that goes from his home to the CS in

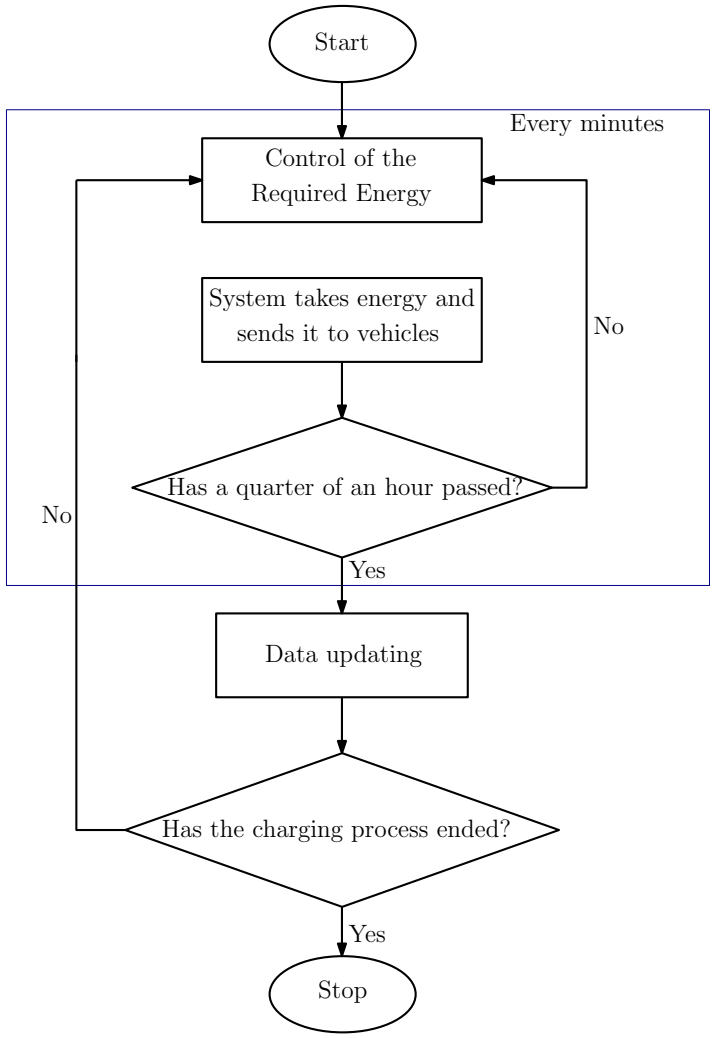


Figure 2.6: *Logical structure of the charging system for the part of actual charge.*

real-time. In this case, the energy required for the process is taken from another source, if possible. In the same way, if for any reason the energy supply of one of the sources changes instantaneously, the system takes the energy required, according to the logic already specified, from the other sources. At the end of every quarter of hour, the CS verifies if the charge proceeds as expected. If not, the missing energy is equally distributed and added to the energy required in the remaining quarters of hours. At the end of the procedure, the system outputs the energy stored in the battery,

the SoC, and the charging cost.

2.3 Case studies

In this section we define the features of the realistic case studies used to evaluate the impact of the previously described condominium system for shared charge of EVs. In particular, we retrieve from a measured data-set the energy loads of the condominium, we determine the size of the components of the system (Figure 2.2), and we characterize the electric vehicles and their usage.

In the past few years, several residential consumption data-sets have been introduced such as ECO [245], BLUED [251], GREEND [252], REDD [253], AMPds [254], and iAWE [255]. Each of these one shows different characteristics with respect to the number of households, data granularity, analysis time, side information (e.g. coverage of appliances with smart plugs), and level of detail of the measured data. Among the aforementioned, we select the ECO data-set as it is European (as the analyzed energy context), complete, detailed, and has a long period of observation. In fact, it has high-resolution measured electricity consumption data (1 Hz frequency) from 6 different households in Switzerland over a period of 8 months (from June 2012 to January 2013). From such data-set we select three households. The consumption of the following appliances are measured for each household: (i) Apartment 1: fridge, dryer, coffee machine, kettle, washing machine, PC, freezer, (ii) Apartment 2: tablet, dishwasher, stove, fridge, TV, Hi-Fi, freezer, kettle, lamp, laptops, and (iii) Apartment 3: fridge, kitchen appliances lamp, Hi-Fi, laptop, freezer, tablet, entertainment, microwave.

For each analyzed apartment, and for each season, we select from the data-set a typical weekday and a typical weekend day. To choose such typical days we first characterize the energy load distribution within the data-set by calculating the average electric power and representing it in a frequency histogram with a bin width of 100 W (Figures 2.7, 2.8, and 2.9 for apartments 1, 2, and 3 respectively). Then, in each histogram we select the typical days from the most populated intervals. Such selected days represent the actual charging loads of the apartments. For the forecast charge we assume to use the load of the previous day, differentiating between weekday and weekend. Following the procedure previously highlighted we obtain the electric energy loads of the apartment 1 represented

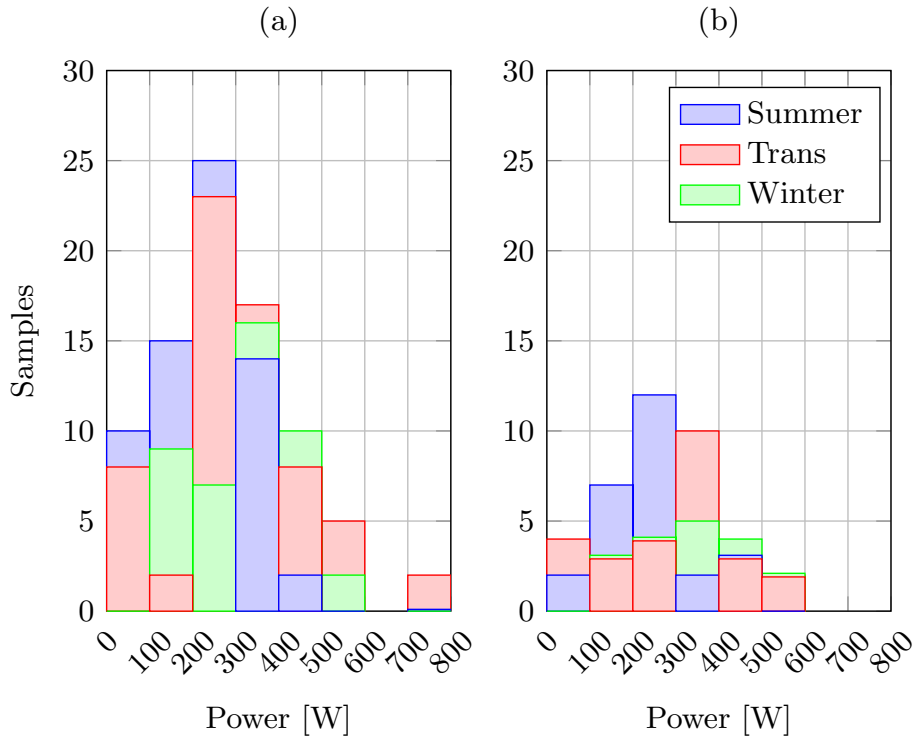


Figure 2.7: *(a) Weekdays electric load frequency histogram for apartment 1, (b) Weekend days electric load frequency histogram for apartment 1.*

in Figures 2.10 and 2.11. Similar detailed loads for apartments 2 and 3 are reported in Figures 2.12, 2.13, 2.14 and 2.15.

In the case studies, the components of the analyzed system have the following characteristics: (i) the RB is composed of the previously characterized 3 apartments and 1 elevator, (ii) the CS is composed of the centralized logical system and three wall-boxes (see Section 2.2.1), (iii) the EVs can be up to 3, (iv) the CDEL has 10 kW nominal power, and (v) the PV has a size of 10 kWp. We select such photovoltaic size because we consider 3 kWp for each apartment (equal to its maximum load), and 1 kWp for the elevator. We generate the PV production from the PVGIS tool [247], considering the city of Viterbo. We consider three EVs setting the parameter $\alpha = 3$ in Equation (2.3). Each vehicle represent a different commercial model covering all the price ranges in the current market. Their relevant properties are represented in Table 2.2. Users 1, 2 and 3 are the inhabitants of the apartments 1, 2, and 3 respectively. User 1 is the owner of the

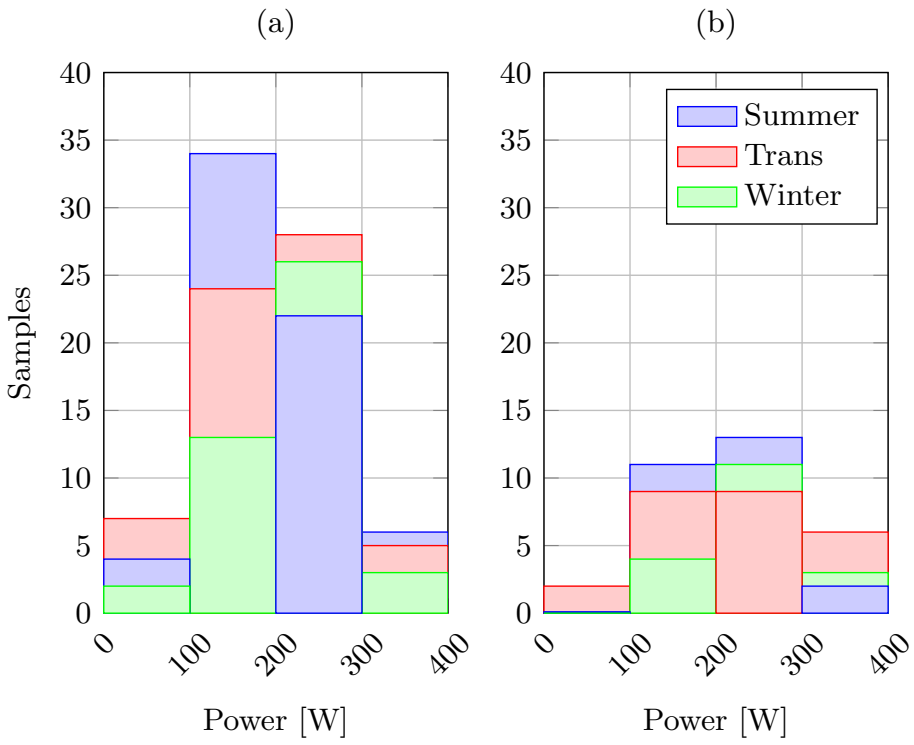


Figure 2.8: *(a) Weekdays electric load frequency histogram for apartment 2, (b) Weekend days electric load frequency histogram for apartment 2.*

Type of car	Battery Capacity	Consumption c_k
Smart fortwo electric drive	16.7 kWh	0.167 kWh/km
Nissan Leaf	62 kWh	0.185 kWh/km
Tesla Model 3	57.5 kWh	0.151 kWh/km

Table 2.2: *Relevant properties of the selected electric vehicles [240, 256, 257].*

Nissan Leaf, user 2 is the owner of the Smart fortwo electric drive, and user 3 is the owner of the Tesla Model 3. Being a residential context each user has his own vehicle and there is no sharing.

We evaluate the charging system operation in different utilization scenarios considering several Origin Times (OTs) and Destination Times (DTs), and several user charging behavioral patterns (selected type of charge). The OTs and DTs for the proposed scenarios are extrapolated

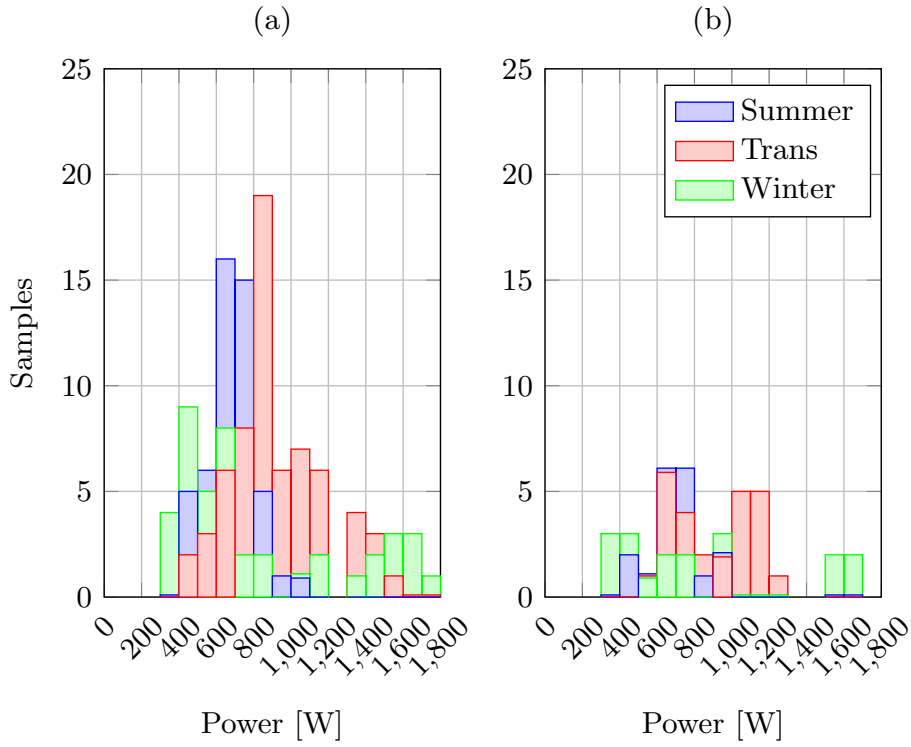


Figure 2.9: *(a) Weekdays electric load frequency histogram for apartment 3, (b) Weekend days electric load frequency histogram for apartment 3.*

by a passenger car travel survey [246]. Figure 2.16 summarizes the results of such survey showing percentage distribution curves of OT and DT on weekdays and weekends. In particular, we note that the distribution is around 0% from 12 AM to 6 AM for all the surveyed cases. Then, on weekends the percentage increases to stabilize around 8% from 8 AM to 9 PM, and finally decrease in the evening. On weekdays, the trends show peaks up to 15% from 7 AM to 10 AM and from 5 PM to 8 PM, while in the central hours of the day the probability is around 4%. From such distribution curves, we distinguish a scheduling of arrivals and departures for the weekdays (Table 2.3) and one for the weekend days (Table 2.4). In both tables, for each user are shown the origin and departure times of two routes. OT1 is the time when the user leaves home, while DT2 is the time when he returns home. Therefore, a vehicle can be charged over a period

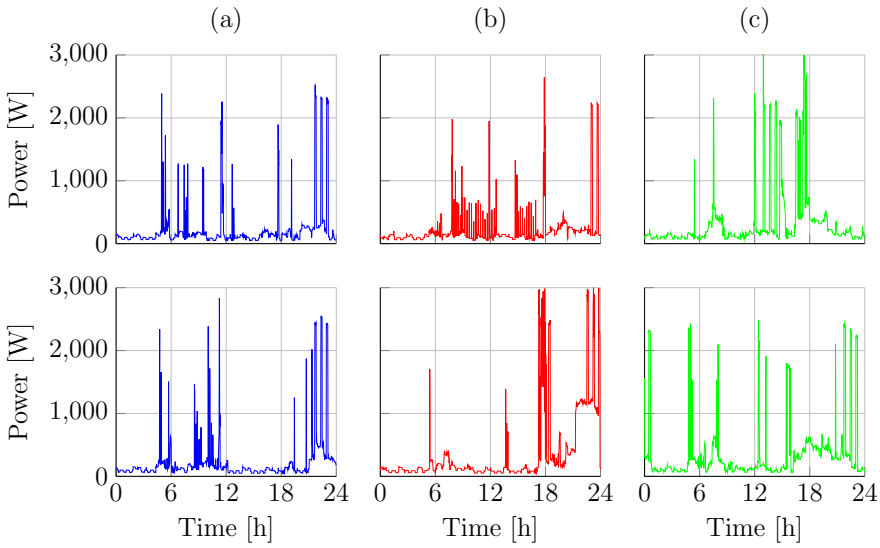


Figure 2.10: *Electric energy loads of the apartment 1 on weekday. Actual and forecast consumption in: (a) summer season, (b) transitional season, and (c) winter season.*

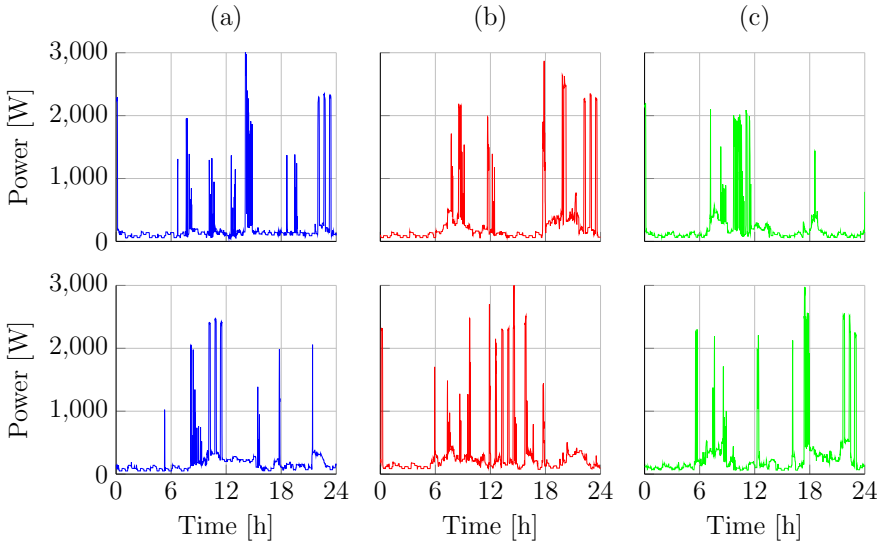


Figure 2.11: *Electric energy loads of the apartment 1 on weekend day. Actual and forecast consumption in: (a) summer season, (b) transitional season, and (c) winter season.*

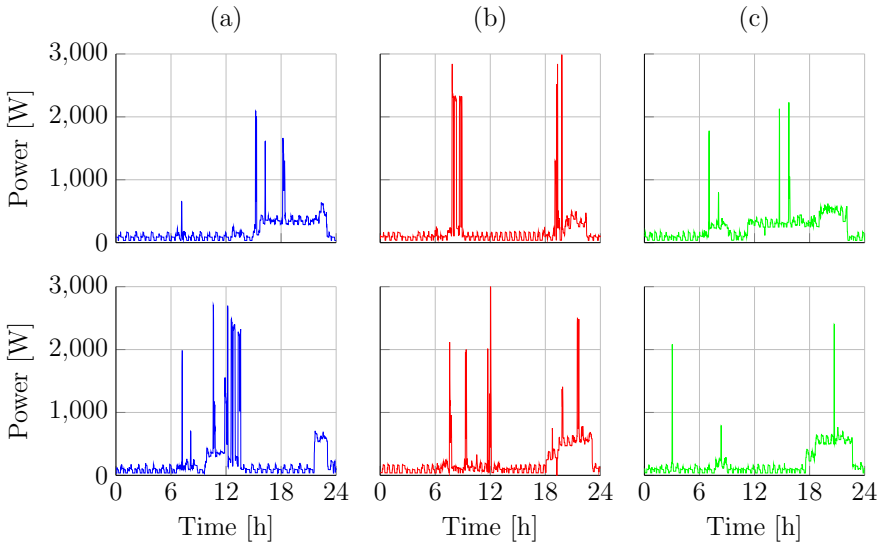


Figure 2.12: *Electric energy loads of the apartment 2 on weekday. Actual and forecast consumption in: (a) summer season, (b) transitional season, and (c) winter season.*

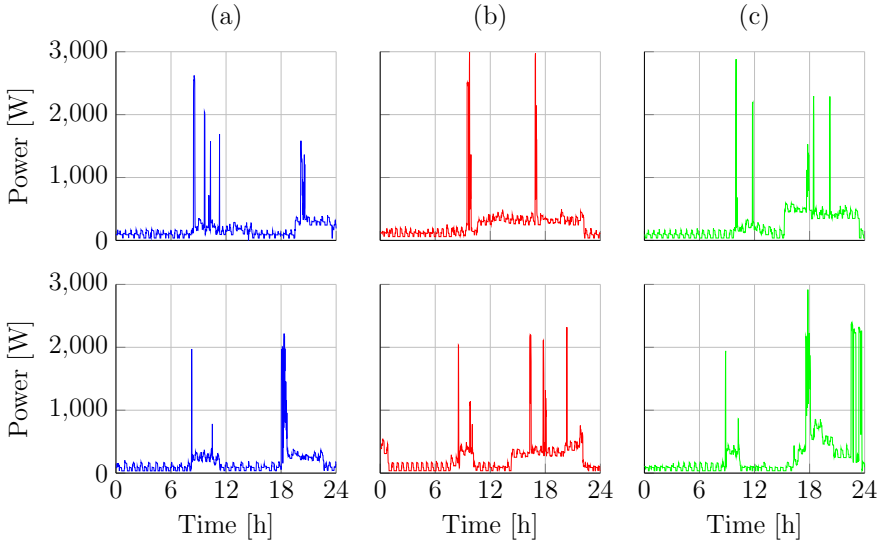


Figure 2.13: *Electric energy loads of the apartment 2 on weekend day. Actual and forecast consumption in: (a) summer season, (b) transitional season, and (c) winter season.*

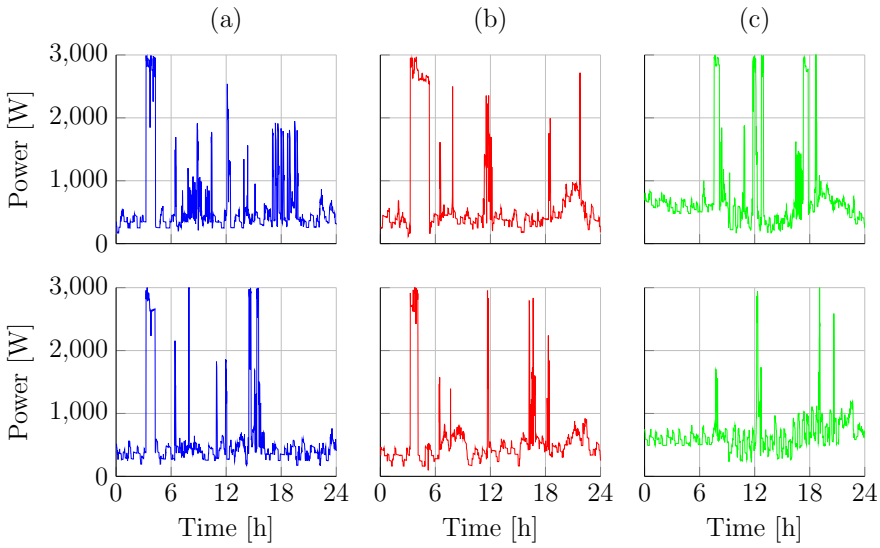


Figure 2.14: *Electric energy loads of the apartment 3 on weekday. Actual and forecast consumption in: (a) summer season, (b) transitional season, and (c) winter season.*

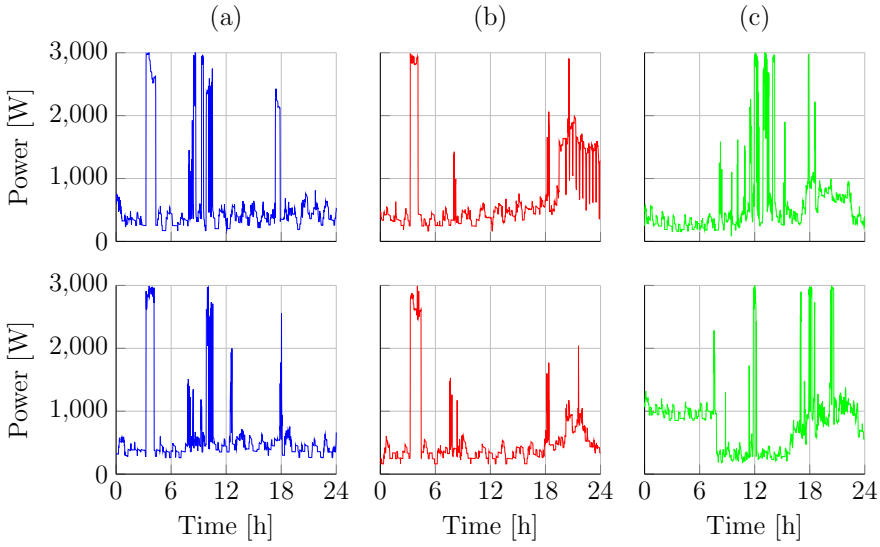


Figure 2.15: *Electric energy loads of the apartment 3 on weekend day. Actual and forecast consumption in: (a) summer season, (b) transitional season, and (c) winter season.*

of time from DT2 to OT1. The consumption in kWh per each route c_e is

$$c_e = T_r \cdot v_a \cdot c_k, \tag{2.5}$$

being $T_r = \mathrm{DT}_i - \mathrm{OT}_i$ the route time of the i^{th} route, c_k the consumption per kilometre of the EV analyzed, and v_a the average trip speed that in Europe is $v_a = 47.5\,\text{km/h}$ [258]. Equation (2.5) allows to calculate the daily energy demands for each EV on weekdays and weekends. In particular, on weekdays user 1 requires 8.78 kWh, user 2 requires 3.97 kWh, and user 3 requires 14.34 kWh. Similarly, on weekend days user 1 requires 8.78 kWh, user 2 requires 15.86 kWh, and user 3 requires 28.69 kWh. Such daily energy requirements can be matched with two distinct user charging behavioral patterns. In one case, the user accepts a flexible process that minimizes the charging cost by extending charging time if necessary (Figure 2.5), we refer to this pattern as C_{min}. In the other case, the user demands that the charging process is completed in the minimum possible time, we refer to this pattern as T_{min}.

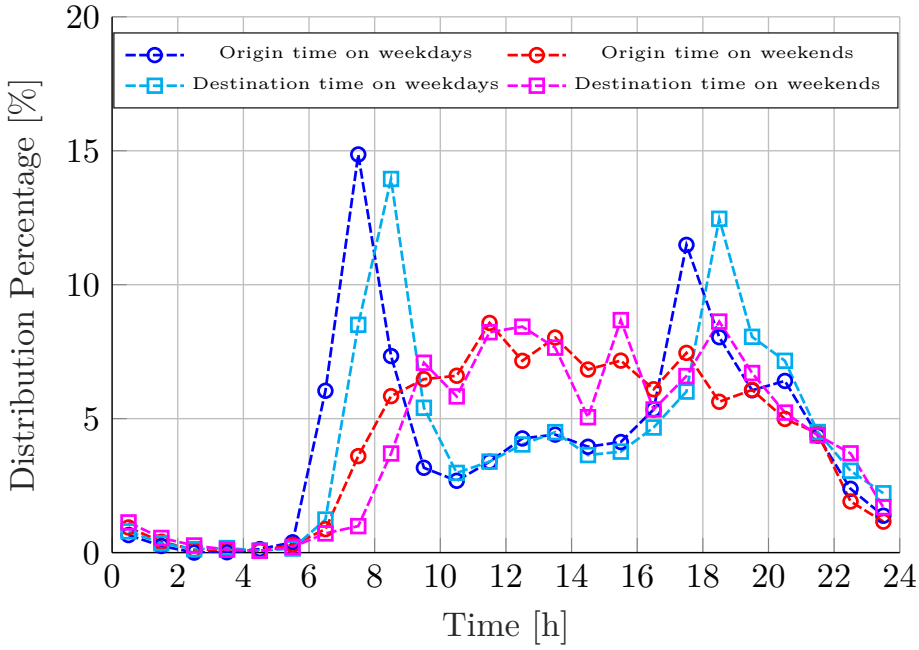


Figure 2.16: *Percentage distribution curves of origin time and destination time on weekdays and weekend days [246].*

User	OT1	DT1	OT2	DT2
User 1	6.30 AM	7 AM	4.30 PM	5 PM
User 2	11.30 AM	11.45 AM	12.45 PM	1 PM
User 3	7.30 AM	8.30 AM	5.30 PM	6.30 PM

Table 2.3: *Selected origin and departure times on weekdays.*

User	OT1	DT1	OT2	DT2
User 1	12 AM	12.30 AM	2.30 PM	3 PM
User 2	11.30 AM	12.30 PM	5.30 PM	6.30 PM
User 3	7.30 AM	9.30 AM	6 PM	8 PM

Table 2.4: *Selected origin and departure times on weekend days.*

2.4 Results and Discussion

Figures 2.17, 2.18, and 2.19 report the costs and the specific costs (€/kWh) of charge for the case studies defined in Section 2.3 for summer, transitional, and winter seasons respectively.

In the summer weekday the charging costs are 1.56 €, 0.49 €, and 2.43 € for users 1, 2, and 3 respectively, considering the C_{min} behavioral pattern (Figure 2.17(a)). Taking into account also the required energy, the specific charging costs for users 1, 2, and 3 are 0.18 €/kWh, 0.12 €/kWh, and 0.17 €/kWh (Figure 2.17(b)). User 2 pays the lowest specific cost because it starts the charging process at 1 PM and withdraws almost 60 % of the charging energy from PV (2.3 kWh over a total of 3.97 kWh). Users 1 and 3 arrive at 5 PM and 6.30 PM respectively, when the sun radiation is lower. In fact, user 1 withdraws from PV only 16 % of the charging energy, while user 3 only 9.2 %. In the same typical day, considering the T_{min} behavioral pattern, the specific charging costs are 0.21 €/kWh, 0.07 €/kWh, and 0.2 €/kWh. As expected, the cost increases for users 1 and 3 of 17 % and of 18 % respectively. In fact, minimizing the charging time the user 1 withdraws 1.25 kWh from PV, 4.7 kWh from the apartments, and 2.83 kWh from the CDEL while with C_{min} behavioral pattern the user withdraws 1.42 kWh from PV, 7.22 kWh from the apartments, and only 0.14 kWh from CDEL. Similar figures can be observed also for user 3. Counter-intuitively, the user 2 following the T_{min} behavioral pattern

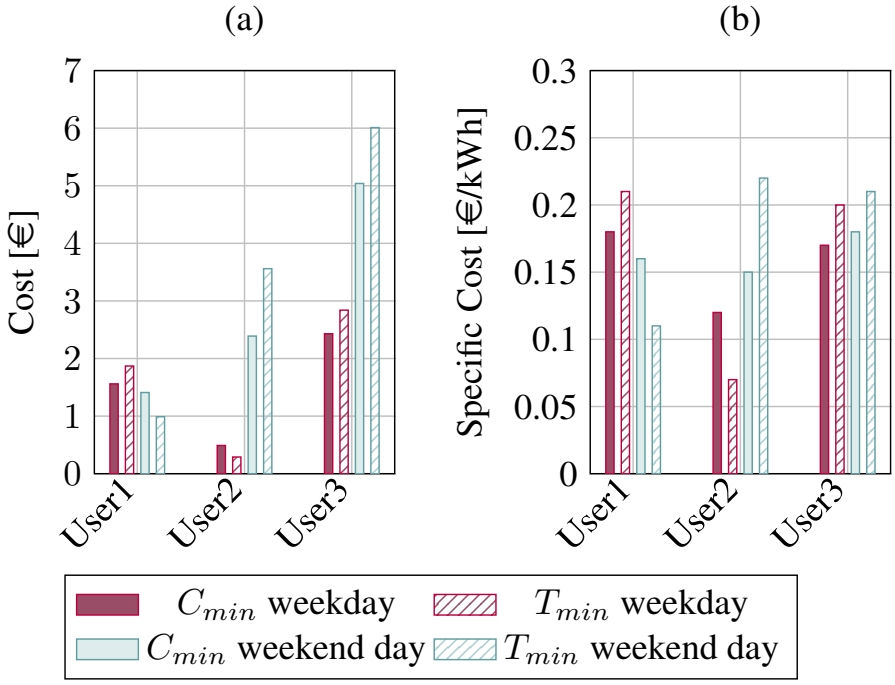


Figure 2.17: *Economic results of the charging system serving a smart energy community of 3 users considering both the minimum cost (C_{min}) and the minimum time (T_{min}) behavioral patterns in summer season: (a) Charging costs, (b) Specific charging costs.*

achieves 42% lower charging cost than C_{min} strategy. In fact, pursuing T_{min} the user withdraws 76% of energy from PV, while pursuing C_{min} only 58%, as a results of a short-term greedy behavior. We also note that with C_{min} the CDEL does not provide energy, while with T_{min} it provides 0.23 kWh showing that the user saturates the PV and apartments capacity. However, the total charging cost for the three users is 4.48 € following C_{min} behavioral pattern and 5 € following T_{min} behavioral pattern. Such result proves that a greedy strategy can be partially beneficial for a user but not for the whole smart energy community. Finally, we observe that the charging processes with T_{min} do not overlap given that the arrival times of the cars are temporally spaced. Otherwise, if the charging processes are simultaneous we expect that the T_{min} behavioral pattern is even less convenient given the sources saturation and the factor X impact (Figure 2.20).

In the summer weekend day the charging costs are 1.41 €, 2.39 €, and

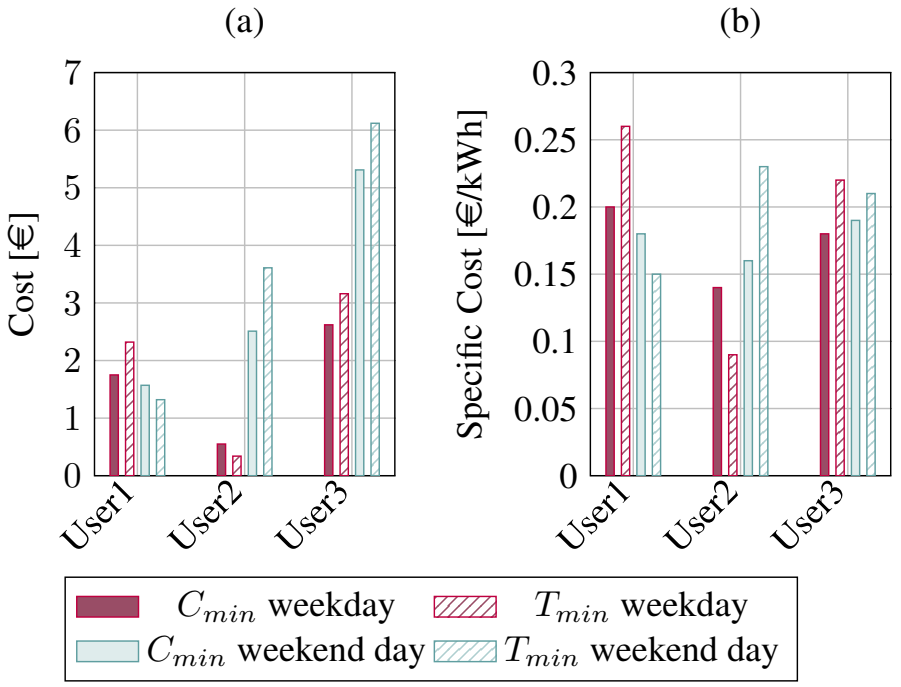


Figure 2.18: *Economic results of the charging system serving a smart energy community of 3 users considering both the minimum cost (C_{min}) and the minimum time (T_{min}) behavioral patterns in transitional season: (a) Charging costs, (b) Specific charging costs.*

5.04 € (Figure 2.17 (a)), while the specific charging costs are 0.16 €/kWh, 0.15 €/kWh, and 0.18 €/kWh (Figure 2.17(b)) for users 1, 2, and 3 respectively, with the C_{min} behavioral pattern. Such results can be explained considering that users 1 and 2 achieve almost 30% of the required energy from PV, while user 3 only 3%. In particular, user 1 arrives at 3 PM and immediately exploits the sun radiation. User 2 arrives at 6.30 PM but manages to utilize the sunlight of the following morning given that the OT1 is 11.30 AM. On the contrary, user 3 cannot store the energy production from sunlight because arrives at 8 PM and leaves the following day at 7.30 AM. The total charging cost in the summer weekend day for the smart energy community is 8.84 € pursuing C_{min}, while it is 10.56 € (0.99 €, 3.56 €, and 6.01 € for users 1, 2, and 3) pursuing T_{min}. Such results confirm the analysis outlined commenting summer weekday. In more detail, users 2 and 3 specific charging costs increase respectively up to 0.22 €/kWh and 0.21 €/kWh. These increments dominate over the

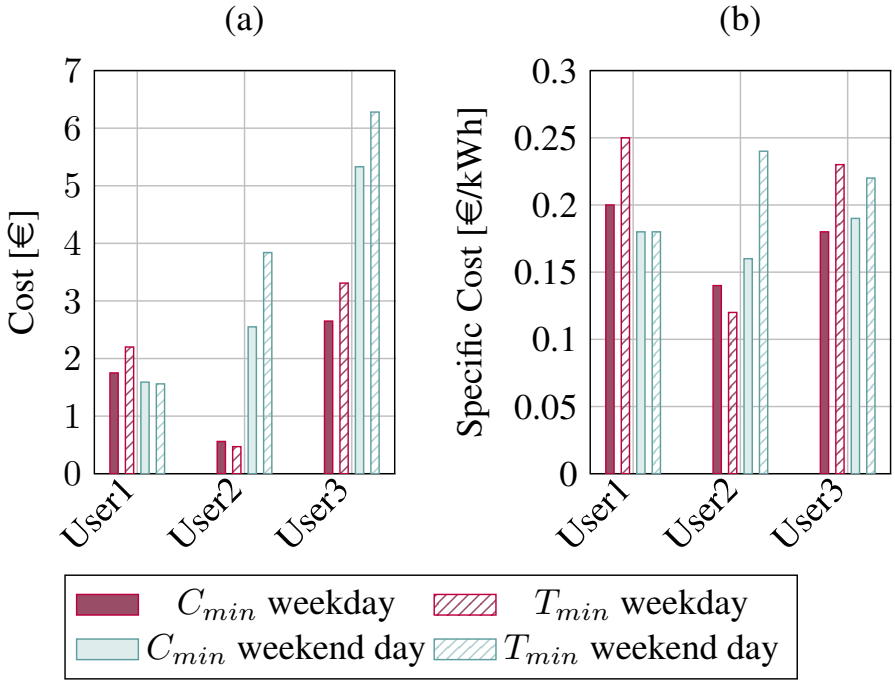


Figure 2.19: *Economic results of the charging system serving a smart energy community of 3 users considering both the minimum cost (C_{min}) and the minimum time (T_{min}) behavioral patterns in winter season: (a) Charging costs, (b) Specific charging costs.*

decrease of user 1 that pays 0.11 €/kWh. Such phenomenon results from the greedy exploitation of the PV as already observed for user 2 in the summer weekday.

Comparing Figures 2.18 and 2.19 with Figure 2.17, we note that in the analyzed reference seasons, the charging costs for each user scale in the same way varying the reference day (weekend or week) and the behavioral pattern. Therefore, we conclude that in the reference seasons the charging costs for each user maintain the same proportions. For example, user 1 pays for every season the highest charging cost for T_{min} weekday, followed by C_{min} weekday, C_{min} weekend day, and T_{min} weekend day. The charging costs for the energy community monotonically increase going from summer, through transitional, to winter. Considering the C_{min} behavioral pattern the costs are 4.48 €, 4.92 €, and 4.96 € in the weekday, whereas the costs are 8.84 €, 9.39 €, and 9.47 € in the weekend day for summer, transitional, and winter respectively. Similarly, for

the T_{min} behavioral pattern such costs are 5 €, 5.82 €, and 5.98 € in the weekday, whereas the costs are 10.56 €, 11.05 €, and 11.68 € in the weekend day. In this regard, the charging costs increase going from summer, through transitional, to winter because the available PV power decreases resulting in higher electricity withdrawn from the apartments and from the CDEL. For instance, for the C_{min} weekday the energy community withdraws 5.04 kWh, 2.12 kWh, and 1.77 kWh from PV for summer, transitional, and winter respectively. At the same time, the withdrawals from the apartments are 20.89 kWh, 23.74 kWh, and 24.2 kWh. In this context, the CDEL works as a buffer providing on average 1.17 kWh. Similar results can be observed also for C_{min} weekend day, and for T_{min} week and week end days.

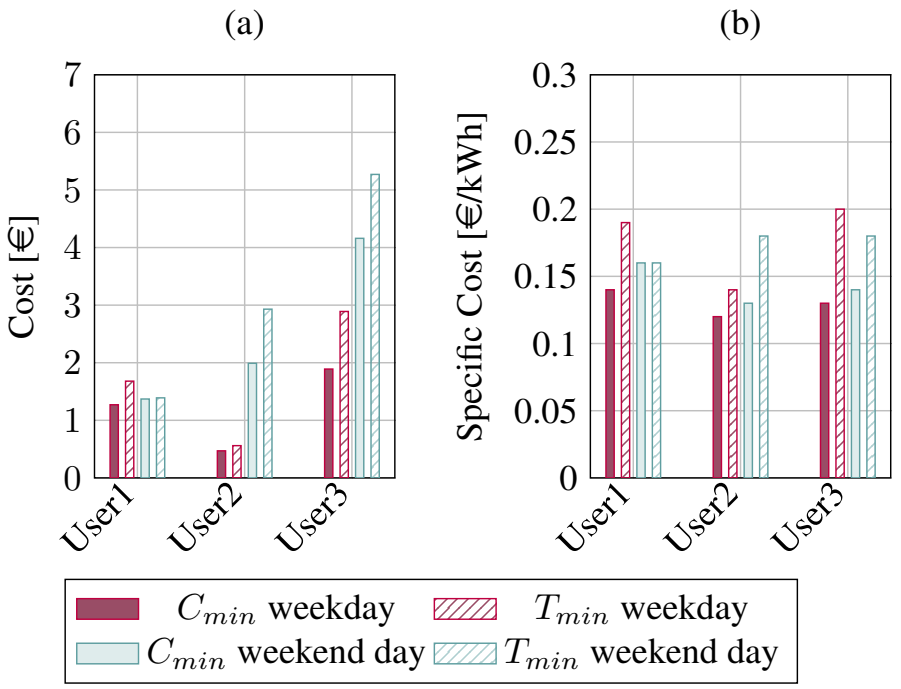


Figure 2.20: *Economic results of the charging system serving a smart energy community of 3 users that arrive at 1 PM considering both the (C_{min}) and the minimum time (T_{min}) behavioral patterns in summer season: (a) Charging costs, (b) Specific charging costs.*

The counter-intuitively economic saving passing from C_{min} to T_{min} behavioral pattern observed for user 1 in weekend day and for user 2 in weekday during summer, is less pronounced during transitional season and

is not noted during winter, as a result of the lower available PV power. However, we expect that also in summer the T_{min} behavioral pattern results in higher cost for the single user if several EVs arrive at the same time. To prove this, we analyze an additional case where all the users arrive at 1 PM maintaining the energy requirements previously reported. In particular, the EVs arrive with the following orders: (i) user 2, 1, 3 for weekday, and (ii) user 1, 2, 3 for weekend day. Figure 2.20 reports the costs and specific costs of charge for the corner case just described. In such figure, we note that for all the users passing from C_{min} to T_{min} the charging costs increase. The cost increment is less pronounced for the user arriving first that finds the highest available energy. With the T_{min} behavioral pattern, we observe that the PV and apartments power availability saturates and consequently the withdrawal from CDEL increments. In fact, considering C_{min} the energy community during weekday takes 10.23 kWh, 16.31 kWh, and 0.92 kWh from PV, apartments, and CDEL respectively. While with T_{min} such figures are 9.32 kWh, 7.72 kWh, and 9.96 kWh. The energy from PV and apartments decreases with T_{min} because the charging time is shorter and such sources have limited available power. Similar results can be observed also for weekend day, where the CDEL energy increases 11 times for T_{min} with respect to C_{min}. Finally, we also note that the factor X contributes to raise the costs.

2.4.1 Discussion

Summarizing, the charging costs for the energy community in weekday are 4.48 €, 4.92 €, and 4.96 € following C_{min} behavioral pattern for summer, transitional and winter respectively. Alternatively, following T_{min} behavioral pattern the costs are 5 €, 5.82 €, and 5.98 €. In the weekend day the energy community pays for the charging processes 8.84 €, 9.39 €, and 9.47 € following C_{min} behavioral pattern for summer, transitional and winter respectively. Instead, considering the T_{min} behavioral pattern such charging costs are 10.56 €, 11.05 €, and 11.68 €. The alternative to the proposed condominium charging system is publicly available slow charging station (i.e. Enel X®), where the specific charging price is equal to 0.45 €/kWh [259]. Recalling that the users require 27.09 kWh and 53.33 kWh to charge the EVs in the weekdays and weekend days respectively, the aggregate charging costs in public charging stations are 12.19 € and 24 €. Therefore, both in the weekdays and in the weekend

days it is possible to save between 51% and 63% depending on the season and on the behavioral pattern.

Besides minimizing the charging costs, the aim of the proposed system is to decrease the load on the grid to subsequently reduce the required investments for electric mobility diffusion. To effectively lower the grid requirements, the system should reduce: (i) the amount of electricity required from charge-dedicated electric line, and (ii) the amount of renewable electricity sent to the grid being not self-consumed. To assess the first point we report in Table 2.5 the energy withdrawn from the charge-dedicated electric line E_{CDEL}, comparing the baseline scenario where external charging stations are used and the scenarios where the proposed system is used with both C_{min} and T_{min} strategies. The data in such table are aggregated for the three users.

	Baseline	C_{min}	T_{min}
Summer weekday E_{CDEL} [kWh]	27.09	1.16	8.87
Summer weekend day E_{CDEL} [kWh]	53.33	2.04	23.68
Transitional weekday E_{CDEL} [kWh]	27.09	1.23	9.82
Transitional weekend day E_{CDEL} [kWh]	53.33	2.83	21.07
Winter weekday E_{CDEL} [kWh]	27.09	1.12	9.47
Winter weekend day E_{CDEL} [kWh]	53.33	2.54	23.33

Table 2.5: *Charge-dedicated electric line energy requirements aggregated for the three users.*

The values reported in Table 2.5 confirm the high potential of the developed system in reducing the amount of electricity required from charge-dedicated electric line. In particular, we observe that the E_{CDEL} percentage reduction varies between 95% and 96% considering the C_{min} strategy, while it varies between 56% and 67% considering the T_{min} strategy. We also observe that following the C_{min} strategy the seasonal variation and the type of the day only marginally affect (i.e. 1% differential) the effectiveness of the charging system. The opposite is true following the T_{min} strategy.

To assess the interaction between the grid and the photovoltaic system we report in Table 2.6 the aggregated photovoltaic self-consumption percentage $E_{\text{PV,SC}}$ comparing the baseline, C_{min}, and T_{min} scenarios.

	Baseline	C_{min}	T_{min}
Summer weekday $E_{\mathrm{PV,SC}}$ [%]	16.52	23.86	22.94
Summer weekend day $E_{\mathrm{PV,SC}}$ [%]	20.23	32.25	24.87
Transitional weekday $E_{\mathrm{PV,SC}}$ [%]	16.58	20.08	20.15
Transitional weekend day $E_{\mathrm{PV,SC}}$ [%]	18.64	26.35	23.08
Winter weekday $E_{\mathrm{PV,SC}}$ [%]	28.66	34.28	34.16
Winter weekend day $E_{\mathrm{PV,SC}}$ [%]	24.93	38.63	29.82

Table 2.6: *Photovoltaic self-consumption percentage aggregated for the three users.*

In Table 2.6 we note that the photovoltaic energy self-consumption increases following both C_{min} and T_{min} strategies with respect to the baseline, where the PV energy is used only by the apartments. We note that an higher $E_{\mathrm{PV,SC}}$ also entails lower greenhouse-gases emissions attributable to electric mobility, considering the actual grid emission factor of 275 g CO_{2eq}/kWh for Europe [260]. The $E_{\mathrm{PV,SC}}$ increment is generally more pronounced seeking for the minimum cost: it varies between 4% and 14% considering the C_{min} strategy, while it varies between 4% and 7% considering the T_{min} strategy. Therefore, we state that despite the results of the C_{min} strategy are more variable with seasons and day type, they are better in terms of self-consumption increase. Such positive outcomes, sum up to the lower charging prices, lower electricity required from CDEL, and higher power left available to the other users of the energy community. Finally, we note that despite the advantages in terms of self-consumption could be higher with a properly designed stationary battery energy storage system ($\geq$ 60%) [87], the $E_{\mathrm{PV,SC}}$ increment attainable with the proposed charging policy is still relevant, especially considering that the batteries of the cars are only partially available in time and in capacity.

In conclusion, we underline that the system and the logic discussed in this chapter yield economic, environmental, and grid impact advantages similar to those obtained in literature with coordinated EVs charging methods. For example, Ayyadi et al. [102] demonstrated that a system implementing an optimized charging method through linear programming could reduce EVs charging cost by 38% and 50% for 50% and 100% of the EVs penetration rate respectively, compared to an uncoordinated charge. Such results are comparable to the attainable cost reduction demonstrated in this chapter between 51% and 63%. Also other studies implementing

mixed-integer second-order cone programming model [261], and other optimized smart energy control strategies [110, 120] obtain similar results. Therefore, we underline that the performance of the simple system here presented are comparable to those of more complicated charging management methods. The simplicity of our system is crucial to make it applicable as a robust real-time controller. Moreover, it could be possible integrate our EVs charging system and logic with a coordinated method to further optimize its operation.

2.5 Summary

The exploitation of unused electric energy in existing buildings can help to mitigate one of the greatest obstacles to electric mobility diffusion, that is the lack of charging infrastructure. The rationale is that in most buildings the instantaneous required power is often lower than the installed power. More available energy can also come from on-site photovoltaic system. By exploiting such energy sources in an energy community context, it is possible to reduce the impact of electric mobility on the grid, avoiding problems of overload and network malfunction.

In this chapter, we develop and prototype a condominium system for shared charge of electric vehicles implementing a logic and a pricing policy to foster the intelligent use of the available energy and existing buildings. Such peer-to-peer system promotes an energy-responsible and cost-effective charge that discourages the use of electric energy not already available in the building. The main components of the system are: (i) the photovoltaic plant, (ii) the residential building, (iii) the charge-dedicated electric line, (iv) the charging system, and (v) the electric vehicles. The charging system consists of a centralized logical system and wall-boxes. The centralized logical system manages the continuous exchange of data and energy between the plant components. The logic of such an element is based on a forecast part that allows the determination of realistic charging profiles and an actual charging part, in which energy is supplied to the vehicles. These two parts interact with each other to ensure rational system operation.

To evaluate the potential of the developed condominium system for shared charge of electric vehicles, we define realistic case studies leveraging on the prototype characteristics. In particular, the structure of the plant consists of: (i) a residential building composed of 3 apartments and

1 elevator, (ii) the charging system, (iii) 3 electric vehicles (Nissan Leaf, Smart fortwo electric drive, and Tesla Model 3), (iv) a 10 kW charge-dedicated electric line, and (v) a 10 kWp photovoltaic system. We extrapolate the measured energy loads of the apartments for a weekday and a weekend day in every season (summer, transitional, and winter), from the ECO residential consumption data-set [245]. Our study is one of the few [120] using such data-set for mobility applications. We generate the PV production from the PVGIS tool [247], considering a city in central Italy (Viterbo). We use a passenger car travel survey [246] to determine the daily energy demand of electric vehicles and the period in which they can be charged. According to the centralized logical system, the electric vehicles energy demand can be satisfied following two behavioral patterns: one that minimizes the charging cost by extending charging time (called C_{min}), and the other one that minimizes the charging time (called T_{min}). Results show that the charging costs for the energy community in weekday are 4.48 €, 4.92 €, and 4.96 € following C_{min} behavioral pattern for summer, transitional and winter respectively. In such cases the average electric energy withdrawn from the charge-dedicated electric line is 1.17 kWh. The same results for T_{min} behavioral pattern are 5 €, 5.82 €, and 5.98 € with an average value of 9.38 kWh from the dedicated line. The same charging service consisting of 27.09 kWh can be obtained in a publicly available slow charging station (i.e. Enel X®) paying 12.19 €, being the charging price equal to 0.45 €/kWh [259]. In the weekend day the energy community pays for the charging processes 8.84 €, 9.39 €, and 9.47 € following C_{min} behavioral pattern for summer, transitional and winter respectively, withdrawing on average 2.47 kWh from the dedicated line. Instead, considering the T_{min} behavioral pattern such charging costs are 10.56 €, 11.05 €, and 11.68 € with 22.69 kWh from the dedicated line. In the weekend day the cars charge of the energy community requires 53.33 kWh, that in an external charging station costs 24 €. Therefore, the charging system is more convenient than publicly available slow charging stations even considering the behavioral pattern that minimizes the charging time. However, the greatest advantages can be obtained choosing the minimum cost process. From these results, we conclude that the proposed system effectively minimizes the economic expenditure for the electric vehicles charge and the grid usage. We also note that the system increases photovoltaic self-consumption from 4% up to 14%.

Further developments of the study regard the extension to other re-

newable sources (i.e. wind turbine) and to storage solutions (i.e. lithium ion batteries) as well as the integration with a coordinated electric vehicles charging method. Moreover, to further validate the methodology we could evaluate the performance of the proposed system in different energy contexts, climate conditions, and within extensive time periods.

Chapter 3

Optimized design of a H_2 powered moped

Micro-mobility is an increasingly important part of the current energy transition, given the lower energy consumption and reduced tendence to form urban congestion. In this scenario, Fuel Cell Hybrid Electric Vehicles (FCHEVs) present several advantages over state-of-the-art battery electric vehicles, such as increased driving-range and reduced recharge time. In this chapter, we study the conversion of a commercial electric moped (Askoll eS_3®) in a Fuel Cell Hybrid-Light Electric Vehicles (FCH-LEVs) by finding the optimal design of the components through an optimization methodology based on backward dynamic programming. Such optimal design and operation strategy can be also implemented with a rule-based approach.

Section 3.1 states the aim of the chapter by describing in detail the conversion of the power-train of the vehicle. Section 3.2 dissects the developed methodology, while Section 3.3 presents the obtained results and the potential impact of the FC electric moped in several total green energy systems. Finally, Section 3.4 summarizes the methodology and the findings of the chapter.

3.1 Problem Statement

In this chapter we assess the techno-economic feasibility of the conversion of a battery electric moped in a Fuel Cell (FC) electric moped. We develop an optimized sizing methodology for such conversion, which

involves the replacement of the Li-ion battery with a FC, one or more Metal Hydride (MH) tanks and a Li-ion Buffer Battery (BB).We seek the optimal control and design strategy for the moped through a methodology based on backward dynamic programming, introduced in [33], and further developed in [12, 34, 132, 168]. We also demonstrate that such methodology can be implemented through a rule-based approach.

Figure 3.1 represents the main elements of the two vehicles configurations analyzed. In the battery electric moped the electric energy is withdrawn from the Li-ion battery and then used by the electric motor for the drive. On the other hand, in the FC electric moped the hydrogen is withdrawn from the MH tank and oxidized to produce the energy utilized by the electric motor for the traction. For this application we consider Proton Exchange Membrane Fuel Cells (PEMFCs) that are the standard for mobility applications given the high power density, the fast dynamic resulting from the low operating temperature (60-80 °C), and the high durability [262, 263]. Moreover, we select metal hydrides to store hydrogen because such technology has a higher volumetric energy density at relatively low pressure (i.e. ≤ 15 bar) when compared to pressurized tank hydrogen storage. In both configurations, the motor works as an electric generator during deceleration by supplying energy to the batteries.

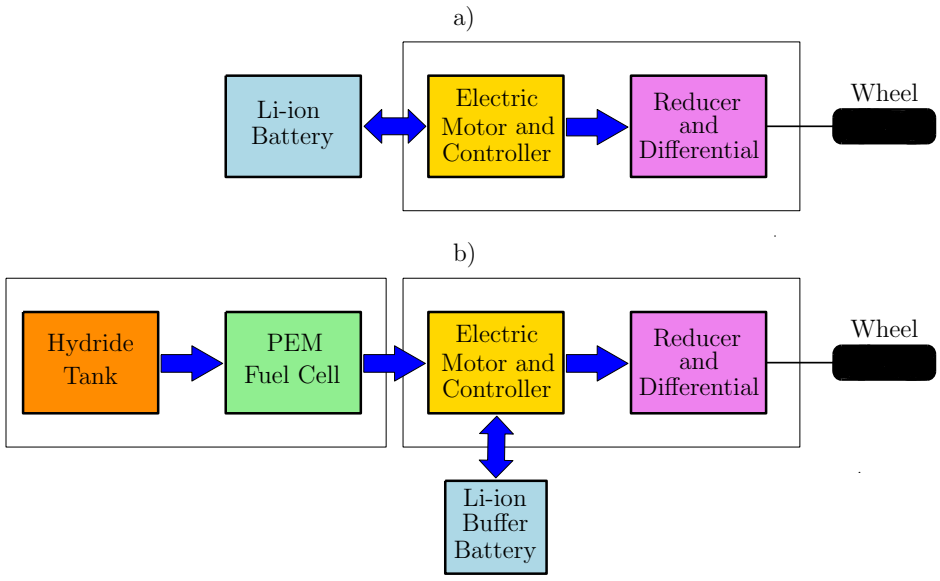


Figure 3.1: *Schematic representation of the moped configurations: a) main elements of the e-moped, b) main elements of the FCH-LEV.*

3.1.1 Vehicles selection and description

We select the Askoll eS$_3$® [264] as the reference e-moped for our case studies because it is the most sold in Italy in the period January-November 2019 [265]. Moreover, in terms of cost, power, and battery capacity it constitutes a representative solution of the best-selling electric mopeds in Europe [266]. The main characteristics of the Askoll eS$_3$® are shown in Tables 3.1 and 3.2.

Feature	Value	Unit of Measure
Power of electric Motor	2700	W
Maximum speed	66	km/h
Maximum torque (to the wheel)	130	Nm
Range	96	km
Width	1830	mm
Seat height	760	mm
Maximum height	1036	mm
Weight (without battery)	70	kg
Permissible maximum weight	245	kg
Cost	3790	€

Table 3.1: *Relevant properties of the Askoll eS$_3$® [267].*

Battery	Li-ion	
Number of Batteries	2	
Battery capacity (for a battery)	1410	Wh
Battery Weight (for a battery)	8.1	kg
Cost	900	€

Table 3.2: *Relevant properties of the Askoll eS$_3$® batteries [268].*

3.2 Methododology

3.2.1 Driving cycle

We use the World harmonised Light-duty vehicles Test Procedure (WLTP) to analyze the consumption and the performance of the moped. Such procedure consists of several cycles [269] that are applicable to different categories of vehicles on the basis of the weight-power ratio (PMR), defined as

$$PMR = \frac{P_{\mathrm{M,max}}}{m_{\mathrm{tot}}}, \tag{3.1}$$

in which $P_{\mathrm{M,max}}$ is the nominal motor power, and m_{tot} is the total mass. For the Askoll eS_3® $P_{\mathrm{M,max}} = 2700\,\mathrm{W}$, and

$$m_{\mathrm{tot}} = m_{\mathrm{e}} + m_{\mathrm{b}} + m_{\mathrm{p}} = 157\,\mathrm{kg}, \tag{3.2}$$

where $m_{\mathrm{e}} = 70\,\mathrm{kg}$ is the empty mass of the e-moped (Table 3.1), $m_{\mathrm{b}} = 16.2\,\mathrm{kg}$ is the mass of the batteries (Table 3.2), and $m_{\mathrm{p}} = 70.8\,\mathrm{kg}$ is the mass that we assume for an European average passenger [270]. $PMR = 17.2\ \mathrm{W/kg} < 22\,\mathrm{W/kg}$, therefore the Askoll eS_3® belongs to the class 1 Worldwide harmonized Light vehicles Test Cycles (WLTC). Such cycle has a maximum speed of 64.4 km/h, and consists of three subcycles: the first one at low speed, the second one at medium speed, and the third at low speed for a total duration of 1613 s. The integration over time of the speed profile in Figure 3.2 a) gives a distance of $d_{\mathrm{WLTC,1}} = 11.4\,\mathrm{km}$.

3.2.2 Vehicle modeling

The total tractive effort of the moped in the direction of motion compensates the aerodynamic drag and the inertia

$$F_{\mathrm{W}}(t) = \frac{1}{2} A_{\mathrm{CS}} C_{\mathrm{D}} \rho v(t)^2 + m_{tot} a(t), \tag{3.3}$$

where $v(t)$ and $a(t)$ are respectively the instantaneous speed and acceleration retrieved from the class 1 WLTC speed and acceleration profiles (Figure 3.2), A_{CS} is the cross section surface, C_{D} is the drag coefficient, $\rho = 1.225\,\mathrm{kg/m^3}$ is the air density at 15 °C and atmospheric pressure, and m_{tot} is the total mass of the moped and of the passenger, see Equation (3.2). In this equation, we consider negligible a mass factor accounting for the equivalent mass increase due to the angular moments of the rotating components of the moped, and the gravitational resistance over slopes.

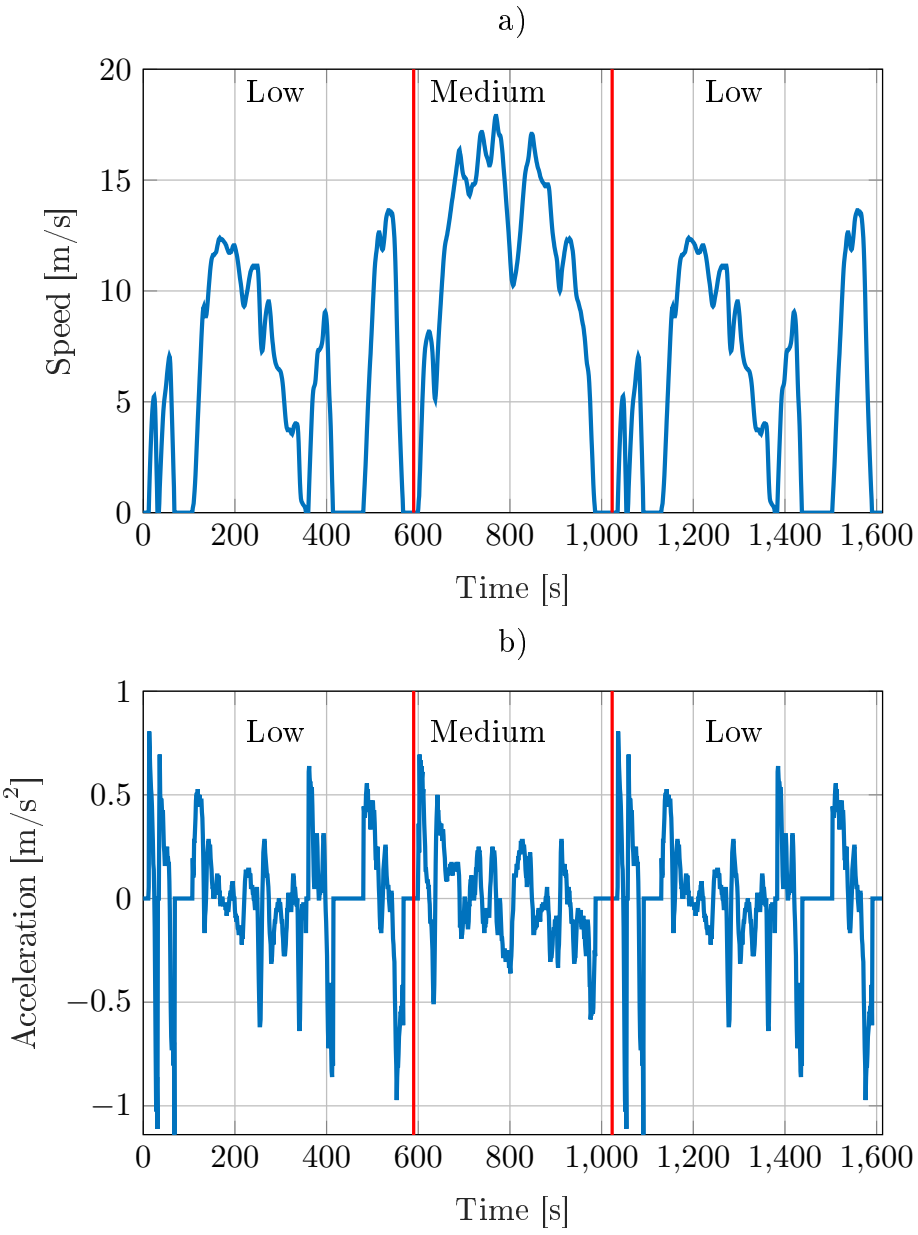


Figure 3.2: *a) Class 1 WLTC speed profile; b) Class 1 WLTC acceleration profile.*

The cross section surface $A_{CS} = 0.5165\,m^2$ is the sum of the front area of the moped, of the torso, and of the neck of the passenger assuming average antropometric values [271], and of the helmet [272]. The instantaneous

power to the wheel P_W is then

$$P_W(t) = F_W(t)v(t). \tag{3.4}$$

The power to the motor P_M considers the power loss due to transmission

$$\begin{cases} P_M(t) = P_W(t)/\eta_T & \text{if} \quad P_W(t) > 0 \\ P_M(t) = P_W(t)\eta_T & \text{if} \quad P_W(t) \leq 0 \end{cases}, \tag{3.5}$$

where $\eta_T = 0.912$ is the transmission efficiency [273]. To quantify the drag coefficient in Equation (3.3) we consider that at the maximum speed $v_{max} = 18.3\,\text{m/s}$, (see Table 3.1) the motor produces the maximum power $P_{M,max} = 2.7\,\text{kW}$ only to compensate the aerodynamic drag, that means $C_D = 1.26$. With this approach we also embed the effect of the rolling resistance in C_D.

The motor also works as a generator when $P_M(t) < 0$, besides producing power when $P_M(t) > 0$. The primary power P_P in input and in output to the motor/generator has to consider the conversion efficiency

$$\begin{cases} P_P(t) = P_M(t)/\eta_M & \text{if} \quad P_M(t) > 0 \\ P_P(t) = P_M(t)\eta_G & \text{if} \quad P_M(t) \leq 0 \end{cases}, \tag{3.6}$$

where $\eta_M = 0.8$ [274] is the motor efficiency and $\eta_G = 0.4$ is the generator efficiency [273].

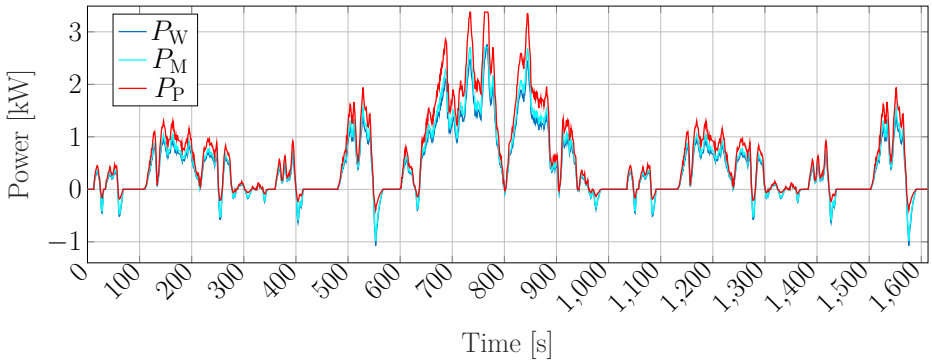


Figure 3.3: *Power to the wheel P_W (blue curve), power to the motor P_M (cyan curve), and primary power P_P (red curve) as a function of time for the driving cycle class 1 WLTC in Figure 3.2.*

Figure 3.3 shows P_W, P_M, and P_P as a function of time for the class 1 WLTC. Such figure shows the direct correlation of the vehicle power to

the driving cycle. We note that the recovered power during deceleration is limited due to the low generator efficiency $\eta_G = 0.4$.

3.2.3 Optimized control and design

As demonstrated in several studies [132, 169, 170] the operating efficiency of any energy system is largely determined by its control strategy [33, 168]. Therefore, we optimally design the FCH-LEV components leveraging on an optimization methodology based on backward dynamic programming. Such methodology has been introduced in [33], and further developed in [12, 34, 132, 168]. It determines the set-points of the active components of the energy system minimizing a prescribed objective function over a determined time-span. In general, it can account for: i) thermal, cooling, and electrical loads, ii) constraints related to the energy flows and to the dynamic behaviour of the plant subsystems, iii) power and efficiency derating with environmental conditions, iv) fuel, maintenance, and cold start costs, and v) the connection to a distribution/immission grid.

In this study, we select the operating cost (i.e. fuel consumption) as the objective function to be minimized, and the BB and the FC as active components of the power-train (see Figure 3.1). We consider the buffer battery and the fuel cell because their operation impacts the efficiency of the whole process and the consequent use of hydrogen. The optimization takes as input the design performance of the active components, and the variation of such performance at part load, together with the required primary power demand P_P, see Equation (3.6). We realistically assume that the buffer battery charge and discharge efficiencies do not vary as a function of the set-point. Whereas, the fuel cell is modeled with a black-box approach, through its efficiency curves as functions of the set-point, to obtain the part load performance, see Section 3.2.4. Specifically, the electric power output of the FC at time t is calculated as

$$P_{FC}(t) = \Phi_{FC}(t) P_{FC,nom}\,, \tag{3.7}$$

where $\Phi_{FC}(t)$ is the set-point and $P_{FC,nom}$ is the FC nominal power. The corresponding required input power is

$$U_{FC}(t) = \frac{P_{FC}(t)}{\eta_{FC}(\Phi_{FC}(t))}\,, \tag{3.8}$$

where $\eta_{\mathrm{FC}}(\Phi_{\mathrm{FC}}(t))$ is the electrical efficiency. The problem is non-linear, being the efficiency a function of $\Phi_{\mathrm{FC}}(t)$. The economic objective function reads

$$G_{\mathrm{Cost}} = \sum_{t=0}^{D} C_{\mathrm{F}}(t, s(t)), \tag{3.9}$$

being t the time interval, $D = 1613\,\mathrm{s}$ the total duration of the class 1 WLTC driving cycle, and C_{F} the fuel cost. The cost is a function of the time interval and the plant state $s(t)$ (i.e. the cluster of set-points of the active components). Equation (3.9) is subject to constraints related to the energy flows. The moped can be considered an isolated electrical energy system being not connected to the grid, therefore the power balance for each time interval reads

$$P_{\mathrm{P}}(t) - P_{\mathrm{FC}}(t) + P_{\mathrm{BB}}(t) = 0 \quad \forall t\,, \tag{3.10}$$

where $P_{\mathrm{BB}}(t)$ is the electrical power of the buffer battery. Note that $P_{\mathrm{FC}}(t)$ is positive, $P_{\mathrm{P}}(t)$ can be positive or negative (regenerative braking), while $P_{\mathrm{BB}}(t)$ is positive when the battery stores energy and negative when it releases energy.

Equation (3.9) is discretized with respect to time and to the plant state to represent the problem as a weighted and oriented graph. The optimal control strategy is determined by seeking for the shortest path across the graph. The reader can consult [12, 33, 34, 168] for more details on the optimization methodology.

3.2.4 Power-train components modeling and design

3.2.4.1 Fuel cell

The integral average primary power demand is $\overline{P}_{\mathrm{P}} = 580\,\mathrm{W}$, and such value is compared with the nominal power of commercially available air-cooled PEMFC stacks. In particular, we consider stacks with $P_{\mathrm{FC,nom}}$ equal to 1 kW and 2 kW [275, 276] between those with $P_{\mathrm{FC,nom}} \geq \overline{P}_{\mathrm{P}}$. We underline that an available power higher than the average required, gives more degrees of freedom to find the optimized operation strategy, besides covering the energy losses due to buffer battery efficiencies. Figure 3.4 represents the hydrogen consumption and the efficiency of such systems, as a function of the produced power and of the set-point Φ_{FC}. Other characteristics of the stacks are reported in Table 3.3.

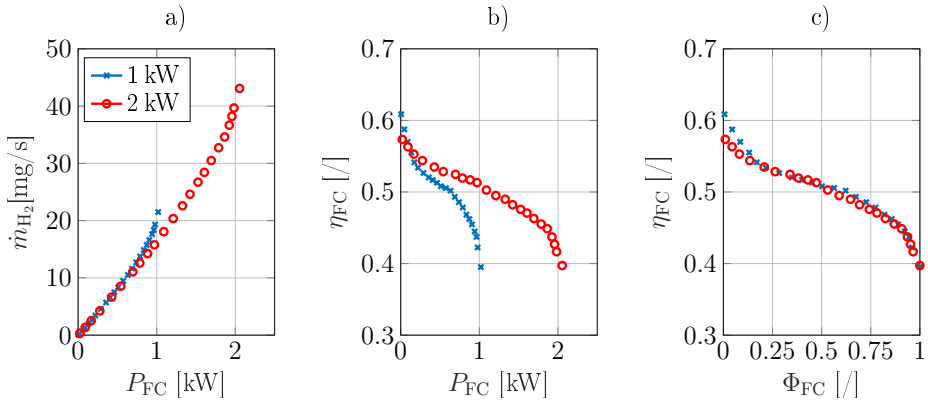


Figure 3.4: *Experimental data of commercially available 1 kW and 2 kW air-cooled PEMFC stacks [275, 276]: a) consumed hydrogen mass flow rate ($\dot{m}_{H_2}$) versus electrical power (P_{FC}), b) efficiency (η_{FC}) versus electrical power (P_{FC}), and c) efficiency (η_{FC}) versus set-point (Φ_{FC}).*

	1 kW	2 kW
Utilization factor	0.83	0.8
Number of cells	48	48
Weight with auxiliaries [kg]	4.4	12.5
Length [m]	0.219	0.303
Width [m]	0.268	0.350
Height [m]	0.123	0.183
Estimated Cost [277, 278] [€]	5200	9500

Table 3.3: *Characteristics of commercially available 1 kW and 2 kW air-cooled PEMFC stacks [275, 276].*

3.2.4.2 Metal hydrides

We determine the hydrogen consumption of the system leveraging on the required input power U_{FC} determined through the optimization methodology, see Section 3.2.3. Specifically, the hydrogen mass required over all the driving cycle reads

$$m_{H_2} = \int_{t=0}^{D} \dot{m}_{H_2}(t)dt, \tag{3.11}$$

where $\dot{m}_{H_2}$ is the hydrogen flow rate required from the FC

$$\dot{m}_{H_2}(t) = \frac{U_{FC}(t)}{LHV_{H_2}}. \tag{3.12}$$

$LHV_{H_2} = 120\,\text{MJ/kg}$ is the hydrogen lower heating value.

To store the required hydrogen mass we consider commercially available MH tanks [279], whose characteristics are reported in Table 3.4. We note that a detailed design of the system should also consider the thermal management of the MH [144]. In this preliminary work, we assume that the MH is always capable to supply the required hydrogen flow rate and we only consider the space required for the thermal management system, without undertaking an in depth design.

Feature	Value	Unit of Measure
Nominal capacity	2000	Sl
Weight	14	kg
Height	0.56	m
Diameter	0.11	m
Charge pressure	5-12	bar
Stored H_2 mass	164	g
Estimated Cost	4000	€

Table 3.4: *Characteristics of commercially available metal hydrides tanks [279] filled with AB_2 alloy.*

3.2.4.3 Buffer battery

To determine the capacity of the buffer battery we iteratively evaluate through the optimization methodology, see Section 3.2.3, the quantity of stored energy as a function of time

$$c_{BB}(t) = e_{FC}(t) - e_{PB}(t) = \int_{t=0}^{t} P_{FC}(t)dt - \int_{t=0}^{t} P_{PB}(t)dt, \tag{3.13}$$

where $P_{PB}(t)$ is the primary power considering also the round-trip efficiency of the buffer battery, assuming respectively the charge and discharge efficiency equal to $\eta_{BC} = 0.96$ and $\eta_{BD} = 0.96$ [273]. Then, the capacity of the battery is the difference between the maximum and the minimum amounts of stored energy

$$C_{BB} = \max\left(c_{BB}(t)\right) - \min\left(c_{BB}(t)\right). \tag{3.14}$$

Through the optimization methodology we also evaluate the state-of-charge as a function of time

$$SOC(t) = SOC(t-1) + \frac{P_{\mathrm{FC}}(t) - P_{\mathrm{PB}}(t)}{C_{\mathrm{BB}}}. \tag{3.15}$$

Finally, we note that small commercial Li-ion batteries for light mobility applications have a specific cost of 1.5 €/Wh [280].

3.3 Results and Discussion

In this section, we determine the characteristics of the components of the FCH-LEV and then we propose its design. We start by quantifying the physical size of the batteries that have to be replaced with the system composed of the FC, the MH tank, and the BB. The batteries of the e-moped have a mass $m_{\mathrm{b}} = 16.2\,\mathrm{kg}$ and occupy all the compartment under the saddle of the Askoll eS$_3$® [267]. From the technical sheet, such space is estimated as $V_{\mathrm{b}} = 5.4 \times 10^{-2}\,\mathrm{m}^3 = 54\,\mathrm{l}$. Considering the requested power profile P_{P} in Figure 3.3, and the charge and discharge efficiency of the Li-ion batteries (both assumed 0.96 [273]), the nominal capacity of the e-moped $C_{\mathrm{EV}} = 2820\,\mathrm{Wh}$ is tantamount to a nominal range $R_{\mathrm{EV}} = 119\,\mathrm{km}$, that corresponds to $n_{\mathrm{EV}} = 10.4$ driving cycles.

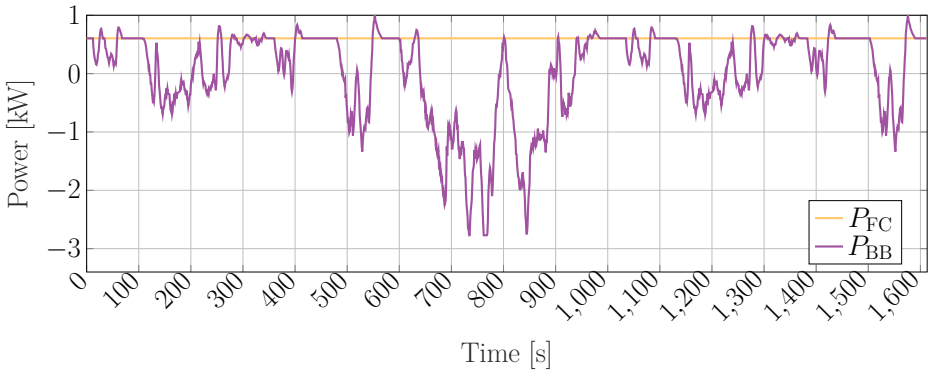


Figure 3.5: *Optimized fuel cell power P_{FC} (orange curve) and buffer battery power P_{BB} (purple curve) as a function of time for the driving cycle class 1 WLTC in Figure 3.5.*

Through the optimized methodology of Section 3.2.3 we obtain for the FCH-LEV the power curves of the fuel cell and of the buffer battery reported in Figure 3.5, considering $P_{\mathrm{FC,nom}}$ both 1 kW and 2 kW. From such

figure, we note that the optimal operating strategy consists of a constant set-point for the FC and a load following approach for the BB. Specifically, the BB operates at variable load because we realistically assume that the charge and discharge efficiencies do not vary as a function of the set-point. Vice versa, the constant FC set-point is such as to produce 605 W, necessary to guarantee energy equilibrium over the driving cycles. This power value depends solely on the required power curve and is independent on the size of the FC. The FC constant power obtained with the optimization process is greater than the integral average primary power demand $\overline{P}_{\mathrm{P}} = 580\,\mathrm{W}$ from the P_{P} curve in Figure 3.3, as a consequence of the BB efficiencies. We note that the overall efficiency could be reduced if the FC would operate at variable set-point. In fact, if the FC would be used in a load following mode producing for several time-steps a power lower than 605 W (hence with higher efficiency), in the following time-steps it should produce a power higher than 605 W (hence with lower efficiency) to guarantee energy equilibrium. As a consequence, more energy would be produced at lower efficiency (higher set-point) decreasing the overall performance. We also note that such reasoning holds true given the symmetrical efficiency curve around 605 W for both the 1 kW and 2 kW FCs, see Figure 3.4. Moreover, we underline that in the optimization process we do not consider the maintenance cost and the degradation due to variable set-point operation, hence further validating our results [281, 282]. The operating difference between the 1 kW and 2 kW FCs relies in the hydrogen consumption to produce the required 605 W. In fact, the stacks consume respectively $m_{\mathrm{H_2}}(1\,\mathrm{kW}) = 164\,\mathrm{g}$ and $m_{\mathrm{H_2}}(2\,\mathrm{kW}) = 157\,\mathrm{g}$ to cover the nominal range $R_{\mathrm{EV}} = 119\,\mathrm{km}$. The 2 kW stack consumes 7 g less hydrogen because for the same power output it works at a lower set-point, and hence with higher efficiency (Figure 3.4). However, the 2 kW stack costs about twice the 1 kW stack and has a mass about three times higher. Therefore, the marginal hydrogen saving does not justify the increase in cost and mass and we select the 1 kW stack for the FCH-LEV.

Through the optimized methodology of Section 3.2.3 we also verify that the required BB capacity is $C_{\mathrm{BB}} = 93\,\mathrm{Wh}$. Such battery is characterized from the curves in Figure 3.6, where the initial and final SOC is set to 0.54. We note that by using the minimum required buffer battery capacity there is only one value of initial and final SOC that guarantees that over all the driving cycle $0 \leq SOC \leq 1$, and hence the system is not flexible in operation. In addition, in the design methodology we do not consider

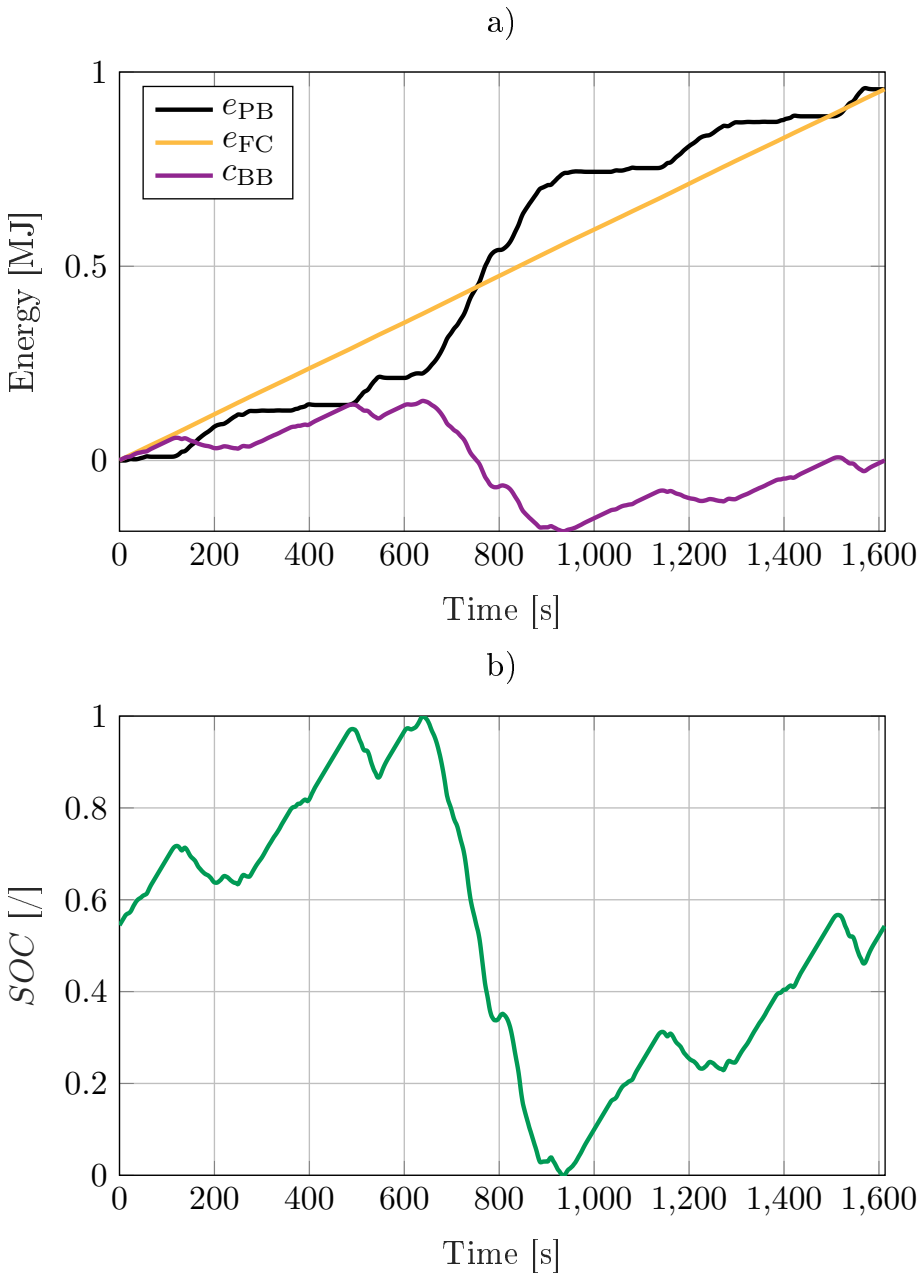


Figure 3.6: *Characterization of the buffer battery: a) produced energy from the fuel cell e_{FC} (orange curve), consumed energy from the moped e_{PB} (black curve), and quantity of stored energy c_{BB} (purple curve) as a function of time; b) state-of-charge as a function of time.*

that the PEMFC stacks have a start-up time of 30 s in which the BB has to provide all the required power. Therefore, we decide to oversize the battery capacity. Incidentally, the smallest commercial Li-ion batteries for mobility applications have a capacity of 240 Wh that is more than two times $C_{\mathrm{BB}} = 93\,\mathrm{Wh}$ [280]. Therefore, we select such 240 Wh buffer battery [283] with dimensions $0.145\,\mathrm{m} \times 0.308\,\mathrm{m} \times 0.042\,\mathrm{m}$ and mass of 3.3 kg.

The stored hydrogen mass in the 2000 Sl MH tank characterized in Table 3.4 is 164 g. Such mass is exactly the same consumed from the 1 kW FC for $n_{\mathrm{EV}} = 10.4$ driving cycles that compose the nominal range. Therefore, a FCH-LEV composed of 1 kW FC stack, a 240 Wh BB, and a 2000 Sl MH tank can cover the same range of the equivalent e-moped. The volume of such hybrid system is $V_{\mathrm{h}} = V_{\mathrm{FC}} + V_{\mathrm{BB}} + V_{\mathrm{MH}} = 7.2 \times 10^{-3}\,\mathrm{m}^3 + 1.9 \times 10^{-3}\,\mathrm{m}^3 + 5.3 \times 10^{-3}\,\mathrm{m}^3 = 1.44 \times 10^{-2}\,\mathrm{m}^3 = 14.4\,\mathrm{l}$. We note that the composing elements of the FCH-LEV can be easily arranged to fit the volume under the saddle. In fact, the FC stack and the buffer buttery are parallelepipeds [275, 276, 283], while the hydrides tanks are commercially available as cylinders or parallelepipeds [279, 284]. Moreover, a volume $V_{\mathrm{f}} = 39.6\,\mathrm{l}$ (that is a part of that occupied from the batteries of the e-moped $V_{\mathrm{b}} = 5.4 \times 10^{-2}\,\mathrm{m}^3 = 54\,\mathrm{l}$) is left free in the FCH-LEV. Such space is 2.75 times higher than $V_{\mathrm{h}} = 14.4\,\mathrm{l}$. Therefore, it will be confidently enough to host the thermal management system and eventually additional MH tanks. The mass of the hybrid system is $m_{\mathrm{h}} = m_{\mathrm{FC}} + m_{\mathrm{BB}} + m_{\mathrm{MH}} = 4.4\,\mathrm{kg} + 3.3\,\mathrm{kg} + 14\,\mathrm{kg} = 21.7\,\mathrm{kg}$, that is 5.5 kg higher than the mass of the batteries of the e-moped $m_{\mathrm{b}} = 16.2\,\mathrm{kg}$. In fact, the FCH-LEV has an higher volume energy density but a lower mass energy density. However, the 5.5 kg mass increase is almost negligible being only 3.5 % of the total mass $m_{\mathrm{tot}} = 157\,\mathrm{kg}$. In fact, repeating the design with $m^{\mathrm{c}}_{\mathrm{tot}} = 162.5\,\mathrm{kg}$, the hydrogen consumption is $m^{\mathrm{c}}_{\mathrm{H_2}}(1\,\mathrm{kW}) = 165\,\mathrm{g}$, instead of $m_{\mathrm{H_2}}(1\,\mathrm{kW}) = 164\,\mathrm{g}$. The e-moped has a cost of 3790 €, 1800 € of which are attributable to the batteries (Tables 3.1, and 3.2). The system composed of the 1 kW FC stack, the 240 Wh BB, and the 2000 Sl MH tank costs 9560 € (Tables 3.3, and 3.4). Such value is more than 5 times the cost of the batteries in the e-moped. However, in the near future, we expect that the diffusion of hydrogen technologies will lower the costs, making the FCH-LEV economically competitive.

If two MH tanks are installed in the moped the hybrid system has a mass $m_{\mathrm{h}} = m_{\mathrm{FC}} + m_{\mathrm{BB}} + 2m_{\mathrm{MH}} = 35.7\,\mathrm{kg}$ and occupies a volume $V_{\mathrm{h}} = V_{\mathrm{FC}} + V_{\mathrm{BB}} + 2V_{\mathrm{MH}} = 1.97 \times 10^{-2}\,\mathrm{m}^3 = 19.7\,\mathrm{l}$. Considering the

increased mass, the nominal range is 234 km that is only slightly lower than the double of the nominal range of the e-moped $R_{EV} = 119$ km. Similarly, with three MH tanks $m_h = 49.7$ kg, $V_h = 25$ l, and the nominal range is 348 km. We highlight that the FCH-LEV is superior than the Li-ion e-moped in terms of attainable range. Therefore, the system composed of the FC and MH tank can be considered a range extender for the base electric vehicle. In fact, the FCH-LEV can almost triplicate the nominal range with a negligible mass increase and with lower overall dimensions than the Li-ion batteries. The increase in the range is not physically possible with Li-ion batteries that occupy all the available volume. We also note that the free volume under the saddle considering three tanks is still $V_f = 29$ l, and can be used for the thermal management system.

Finally, it is also possible to store the hydrogen on board with a high pressure composite tank. In such case the available volume is $V_b - V_{FC} - V_{BB} = 5.4 \times 10^{-2}\,m^3 - 7.2 \times 10^{-3}\,m^3 - 1.9 \times 10^{-3}\,m^3 = 4.49 \times 10^{-2}\,m^3 = 44.9$ l. If all such free space is used to install the high pressure tank, it is possible to store $m_{H_2} = 164$ g at a pressure of 46 bar. However, the typical operating pressure of composite tanks is 300 bar [285, 286]. At such pressure, it is possible to store 1080 g of hydrogen, that are enough to cover more than 6 times the nominal range of the e-moped. Composite tanks have an average specific weight of 500 kg/m^3 [285, 286]. Therefore, a 44.9 l composite tank has an estimated mass of 22.5 kg. Such value makes the mass of the hybrid system $m_h = 30.2$ kg, that is 14 kg higher than the mass of the batteries of the e-moped. Alternatively, it is possible to store 164 g of hydrogen (that is enough to cover the nominal range) in a 6.8 l composite tank at 300 bar [287]. Such tank that has a mass of 3.5 kg, resulting in $m_h = 11.2$ kg, that is lower than the mass of the batteries of the e-moped. Such mass decrease results also in a reduction of the hydrogen consumption per cycle. Despite the possible advantages of high pressure storage, we note that the compression to 300 bar can require up to 10% of the hydrogen lower heating value [288], thus increasing the H_2 recharge cost.

3.3.1 Discussion

We note that the optimized control strategy, consisting of a constant set-point for the FC and a load following approach for the BB, can be straightforwardly implemented in an on board control unit. Moreover, we

underline that the constant $P_{\mathrm{FC}} = 605\,\mathrm{W}$ can also be obtained with the following iterative rule-based approach. Starting from the current tentative FC power P^*_{FC} we are able to calculate the requested primary power P_{PB} and the produced primary power, see below Equations (3.16) and (3.17) for the definitions. Such power profiles are integrated to evaluate the energy equilibrium: if the produced energy is lower/greater than the requested energy, the current tentative FC power is increased/decreased of 0.1 W. Such procedure is repeated until energy equilibrium is reached, given that we do not consider in this work the possibility to use the system as a plug-in FCH-LEV. We initialize the first tentative $P^*_{\mathrm{FC}} = 580\,\mathrm{W}$ as the integral average primary power demand $\overline{P}_{\mathrm{P}}$.

Starting from the primary power P_{P} in Equation (3.6), we introduce P_{PB} that is the required primary power that also considers the charge and discharge efficiency of the BB

$$\begin{cases} P_{\mathrm{PB}}(t) = P_{\mathrm{P}}(t)\eta_{\mathrm{BC}} & \text{if} \quad P_{\mathrm{P}}(t) \leq 0 \\ P_{\mathrm{PB}}(t) = P_{\mathrm{P}}(t) & \text{if} \quad 0 < P_{\mathrm{P}}(t) < P^*_{\mathrm{FC}} \\ P_{\mathrm{PB}}(t) = P^*_{\mathrm{FC}} + \frac{P_{\mathrm{P}}(t) - P^*_{\mathrm{FC}}}{\eta_{\mathrm{BD}}} & \text{if} \quad P_{\mathrm{P}}(t) \geq P^*_{\mathrm{FC}} \end{cases}, \tag{3.16}$$

where $\eta_{\mathrm{BC}} = 0.96$ is the BB charge efficiency [273], $\eta_{\mathrm{BD}} = 0.96$ is the BB discharge efficiency [273]. We note that P^*_{FC} is the FC power that does not vary with time, following the results of the optimized methodology. When $P_{\mathrm{P}}(t) \leq 0$ the generator produces power that is stored in the BB to be used later, and therefore has to be reduced according to the battery charge efficiency. Conversely, when $P_{\mathrm{P}}(t) > 0$ we observe two different cases. If $P_{\mathrm{P}}(t) \leq P^*_{\mathrm{FC}}$ the FC produces the power that is directly used in the motor. Vice versa, if $P_{\mathrm{P}}(t) > P^*_{\mathrm{FC}}$ the excess over the FC power is provided from the BB, considering the discharge efficiency.

The primary power produced by the fuel cell P_{FCB}, has also to consider the charge and discharge efficiency of the buffer battery

$$\begin{cases} P_{\mathrm{FCB}}(t) = P^*_{\mathrm{FC}}\eta_{\mathrm{BC}} & \text{if} \quad P_{\mathrm{P}}(t) \leq 0 \\ P_{\mathrm{FCB}}(t) = P_{\mathrm{P}}(t) + (P^*_{\mathrm{FC}} - P_{\mathrm{P}}(t))\,\eta_{\mathrm{BC}} & \text{if} \quad 0 < P_{\mathrm{P}}(t) < P^*_{\mathrm{FC}} \\ P_{\mathrm{FCB}}(t) = P^*_{\mathrm{FC}} & \text{if} \quad P_{\mathrm{P}}(t) \geq P^*_{\mathrm{FC}} \end{cases}. \tag{3.17}$$

Specifically, when $P_{\mathrm{P}}(t) \leq 0$ the power produced from the FC goes entirely in the BB, with the associated charge efficiency. Conversely, when

$0 < P_{\mathrm{P}}(t) < P^{*}_{\mathrm{FC}}$, the fuel cell satisfies $P_{\mathrm{P}}(t)$ directly and it sends only $P^{*}_{\mathrm{FC}} - P_{\mathrm{P}}(t)$ to the buffer battery, with the associated charge efficiency. Finally, when $P_{\mathrm{P}}(t) \geq P^{*}_{\mathrm{FC}}$ all the FC power is directly used in the motor.

After 249 iterative integration of Equations (3.16) and (3.17), we find $P^{\mathrm{RB}}_{\mathrm{FC}} = 605\,\mathrm{W} = P_{\mathrm{FC}}$ as the final iteration value of P^{*}_{FC} that guarantees the energy equilibrium over the driving cycle (i.e. the state-of-charge of the BB at the beginning and at the end of the driving cycle is the same). Such result is in accordance with the optimized methodology. Figure 3.7 represents the final iteration instant value of P_{FCB} that oscillates around $P^{\mathrm{RB}}_{\mathrm{FC}}$ as a consequence of the variable quantity of power going into the buffer battery, with the associated charge efficiency. In the same Figure we also represent the required primary power P_{PB} evaluated at the final iteration.

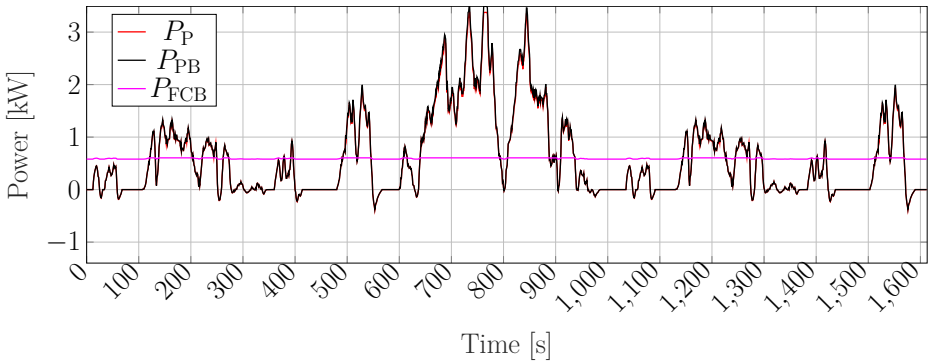


Figure 3.7: *Required primary power P_{P} (red curve), required primary power with buffer battery P_{PB} (black curve), and primary power produced by the fuel cell P_{FCB} (magenta curve) as a function of time for the driving cycle class 1 WLTC in Figure 3.2.*

We evaluate the potential and the impact of a domestic total green energy system for the recharge of the FCH-LEV composed of the 1 kW FC stack, the 240 Wh BB, and the 2000 Sl MH tank. We assume that the residential unit has installed a photovoltaic system with $3.3\,\mathrm{kW_p}$. Using the PVGIS database [227] and considering the city of Viterbo we obtain the typical hourly photovoltaic production for an entire year. Then, we use Energy Plus [87, 225, 289] to determine the hourly energy load reported in Figure 3.8, considering that Viterbo is classified as a heating based climate, according to IEA [224]. For this analysis, we consider that the photovoltaic production in surplus with respect to the residential load

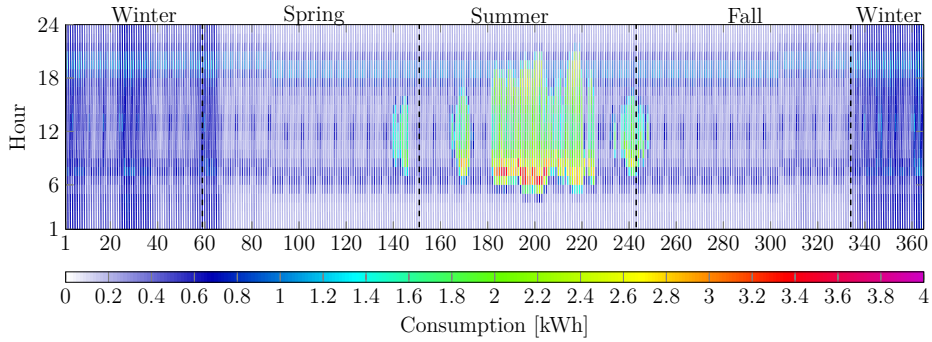


Figure 3.8: *Hourly energy consumption of an apartment in the city of Viterbo (heating based climate [224]).*

feeds a PEM electrolyser with a 80 % efficiency [290]. Such system produces 68 kg of hydrogen per year. Considering that the FCH-LEV needs 164 g of hydrogen to cover the nominal range of $R_{\mathrm{EV}} = 119$ km, the residential total green recharge system can recharge the FCH-LEV 415 times per year (more than once per day), or equivalently that the FCH-LEV can cover more than 49300 km per year with zero emissions.

	Bus	Car
PM2.5 [g]	176.8	145.6
PM10 [g]	218.4	52
NO_x [g]	8850.4	499,2
COV [g]	478.4	156
CO [g]	1872	1435.2
CO_2 [kg]	732	205

Table 3.5: *Emissions of conventional means of transportation for yearly average commute of a student in Viterbo [291].*

Finally, we also evaluate the potential environmental and health impact of the FCH-LEV when used for the mobility of students in a small city such as Viterbo. In this scenario, the average daily round-trip commute is 4 km, considering the typical routes defined in [291]. Given that the students attend the university five days per week, the yearly potential commute distance is 1040 km per student. Using the emission factors in [291], it is possible to quantify in Table 3.5 the yearly emissions of conventional means of transportation such as ICE-based bus and car for every

student. Assuming that the FCH-LEV is fed with green hydrogen (zero total emissions) is possible to avoid the release of these pollutants into the atmosphere. Moreover, given that the FCH-LEV consumes 164 g every 119 km, the yearly hydrogen consumption for every student is 1433 g. By dedicating a photovoltaic system to hydrogen production in a total green shared recharge system, it is possible to obtain 35700 g/kW$_p$. Therefore, for each student it is necessary to install a 4×10^{-2} kW$_p$ recharge system, or alternatively every installed kW$_p$ can satisfy the needs of 25 students.

The results of this chapter highlight the advantages of FCH-LEVs over traditional BEVs. In fact, comparing zero emission vehicles we have to focus on the overall value chain of mobility. The higher attainable driving range and the lower expected recharge time increase the available operating time of the FCH-LEV over the e-moped. This aspect is particularly relevant considering that the development of electric mobility is deeply connected to a shared paradigm. In such a scenario, the same mobility demand can be accomplished with less vehicles, leading to lower capital costs and emissions in production. Moreover, hydrogen has several intrinsic advantages. It can be produced from several renewable energy sources such as biogas and wind or photovoltaic electric energy. Also, it can be stored even on seasonal timespans. Finally, the natural gas distributions grids could be converted to hydrogen operation in the near future, decoupling the mobility energy demand from the electric distribution grid. Such aspect is crucial considering the increasing stress that intermittent renewable energy sources put on such grid.

3.4 Summary

Micro-mobility is increasingly popular due to several advantages, such as lower energy demand and less urban congestion, with respect to conventional internal combustion engine-based mobility. Most of nowadays micro-mobility vehicles are based on electric batteries. However, fuel cell light hybrid electric vehicles could be relevant for the increase in the driving-range and in the drivability, and for the reduction of the recharge time. Therefore, we assess the techno-economic feasibility of the conversion of a commercial battery electric moped (Askoll eS$_3$®) in a fuel cell hybrid electric moped. We leverage on the worldwide harmonised light-duty vehicles test cycle of class 1 to characterize the energy consumption of the electric moped through a dynamic model that accounts for aero-

dynamic drag and inertia. In this process, we also consider the efficiency of the transmission, of the electric motor and generator, and of the buffer battery. Then, we find the optimal size of the fuel cell, hydrogen storage, and buffer battery that replace the Li-ion batteries of the electric moped. For such conversion we develop an optimized sizing methodology based on backward dynamic programming, and we also demonstrate that it can implemented through a rule-based approach.

Results show that a 1 kW proton exchange membrane fuel cell, a 2000 Sl metal hydride hydrogen tank, and a 240 Wh buffer battery can cover the same range of the batteries in the electric moped (119 km). Such hybrid system occupies 39.6 l less volume than the batteries but is 5.5 kg heavier. However, such mass increase is not relevant being only 3.5 % of the total mass. With the current commercial quotations the hybrid system costs 9560 € that is more than five times the cost of the batteries of the moped. However, we expect that the evolution of the hydrogen based technologies will lower the prices. The empty volume resulting from the conversion can be used to install additional metal hydride tanks to increase the driving-range, with a negligible mass increase. In particular, with two tanks it is possible to reach up to 234 km, while with three tanks the driving-range is 348 km. Moreover, using composite tanks it is possible to cover the nominal range (119 km) with 6.8 l of hydrogen at 300 bar. Alternatively, using all the available volume under the saddle (44.9 l) to install the composite tank it is possible to cover the nominal range by storing hydrogen at 46 bar (with reduced compression energy required). Such configuration can also be used to store hydrogen at 300 bar, resulting in more than six times the nominal range.

3.4.1 Estimated impact and future works

The fuel cell hybrid electric vehicle can be recharged with green hydrogen becoming completely emissions free. In particular, in a typical residential apartment with a 3.3 kW_p photovoltaic system it is possible to produce on a yearly basis enough hydrogen to completely recharge the vehicle more than once per day. Such estimation only considers the photovoltaic production in surplus with respect to the energy loads of the apartment. Moreover, the fuel cell hybrid electric vehicle can have a relevant impact also for shared mobility. For example, considering the university students in a small Italian city (Viterbo), it is possible to considerably re-

duce the pollutants and greenhouse gas emissions (Table 3.5). Moreover, a dedicated photovoltaic system can produce the green hydrogen necessary for 25 students every 1 kW_p installed, on a yearly basis.

The results here presented can be further investigated by considering the design of the thermal management system, especially focusing on the metal hydride tank and on the fuel cell stack. Finally, some advanced materials (e.g. metal hydrides alloys) can be evaluated in order to improve the characteristics of the system such as the energy storage density.

Chapter 4

Performance evaluation of coupled MH-PCM storage systems through non-dimensional numbers

Efficient storage solutions that decouple energy use and production are pivotal to the green energy transition. In this context, hydrogen has shown excellent potential. In particular, Metal Hydride (MH) hydrogen storage is one of the most hopeful solutions for both stationary and mobile applications. To store the heat emitted during the absorption process and then to reuse it in the desorption process, the metal hydride is generally coupled with Phase Change Material (PCM).

In this chapter we develop a non-dimensional methodology to characterize the operation of several cylindrical metal hydride-phase change material tank layouts and to determine the optimal configuration in term of charge/discharge time and power. Especially, we apply the Buckingham theorem to obtain 13 non-dimensional parameters which totally describe the process. We utilize the proposed methodology to assess the impact of such parameters on a baseline design metal hydride-phase change material system. Finally, we evaluate a case study by introducing the optimal configuration and by comparing it with the baseline design.

The chapter is organized as follows. In Section 4.1 we state the aim of the chapter and we describe the system. Section 4.2 describes the mathematical model, the domains discretization, the heat exchange model,

and the non-dimensionalization of the problem. Results for the absorption and desorption processes are presented and discussed in Section 4.3. In Section 4.4 we highlight the main aspects of the results. Moreover, we introduce a case study to assess the usefulness of the methodology. Finally, we draw the conclusions in Section 4.5.

4.1 Problem Statement

Although in literature there are numerous studies to optimize the MH-PCM tanks in different respects, a methodology based on dimensionless numbers to characterize the system operation, assess the impact of the salient parameters of the phenomena, and evaluate an optimal configuration is still uncharted, to the best of our knowledge. In this chapter, we develop a dimensionless methodology to analyse and maximize the performances of different cylindrical MH-PCM tank layouts. In particular, by using the Buckingham theorem we combine the geometrical and physical properties of PCM and MH to obtain dimensionless numbers representative of the problem.

The overall system is composed of a inner MH cylinder and a hollow PCM cylinder surrounding the MH bed. The PCM absorbs heat during absorption and transfers heat during desorption. Figure 4.1 shows the system configuration. $\mathcal{L}$ and d are the MH cylinder length and diameter, respectively. During the charge/discharge cycle (absorption/desorption), the following assumptions are made:

- gases comply with the ideal gas model [292],
- porous medium is homogeneous [293],
- inlet/outlet hydrogen pressures are constant [203],
- physical properties of MH/PCM are not dependent on temperature (constant in time) [294],
- gas pressure inside the vessel is uniform, thus neglecting the actual pressure distribution [292],
- no border effect is considered.

In contrast to the gas pressure, the temperature is not evaluated homogeneously within the vessel. The discretization of the MH-PCM domain (to evaluate the effect of the temperature distribution) is addressed in Section 4.2.2. The domain is axisymmetric, therefore the nodes are placed

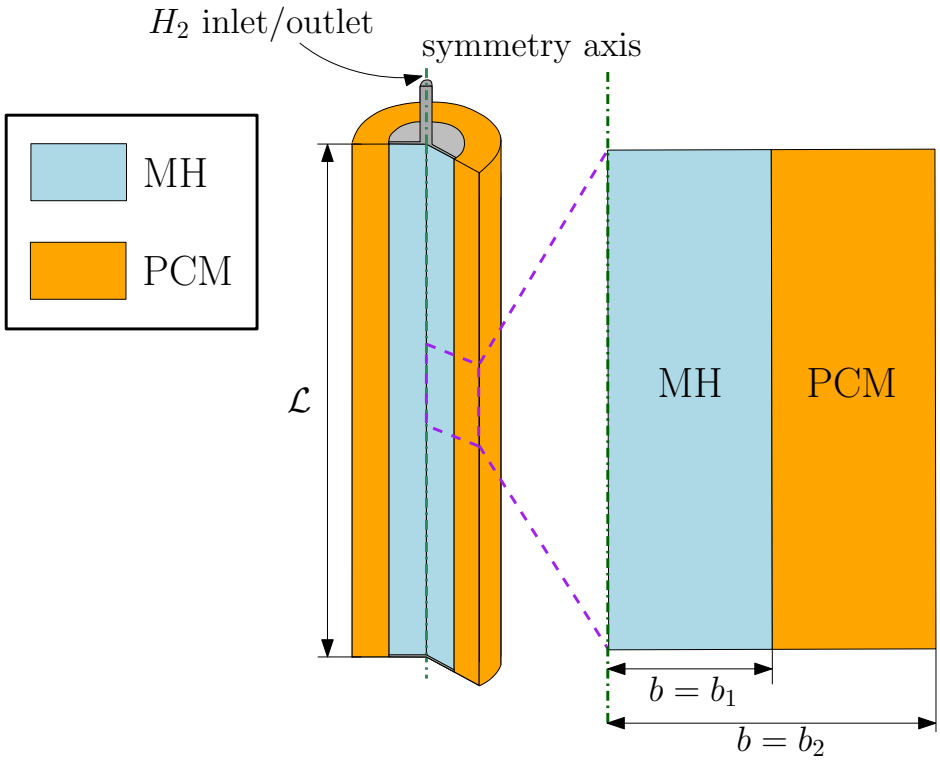


Figure 4.1: *The MH-PCM system configuration.*

between $b = 0$ (vessel core) and $b = b_2$ (external radius of the outer cylinder). In fact, the temperature varies in the radial direction and remains constant in the axial direction. The MH domain is discretized between $b = 0$ and $b = b_1$ (radius of the MH-PCM interface) while the PCM domain is discretized between $b = b_1$ and $b = b_2$. Such discretization allows to switch from partial differential equations to ordinary differential equations, in order to study the whole absorption/desorption process. The increase in problem's complexity is justified considering that our goal is to thoroughly study the influence of several physical parameters on the overall efficiency.

A complete cycle consists of a charge phase, a dormancy phase and a final discharge phase. These are reversible processes, although there exist some irreversibilities which lower the system efficiency (for example the metal powder deformation) [295]. In the present study, such phenomena are neglected and the complete cycle may be carried out indefinitely. Figure 4.2 shows the complete process in the MH-PCM storage system. The

hydrogen enters the inner cylinder from above by means of an inlet valve, thus starting the absorption process. As soon as the absorption ends, the hydrogen flow rate ceases and we can assume that the valve is closed. In the dormancy phase, MH keeps exchanging heat with the PCM until a steady-state condition is reached (i.e. when the hydride and the PCM temperatures coincide). Such operating condition is valid only if we consider that the PCM external surface is thermally insulated [217]. When the valve is open again the hydrogen gas starts flowing out of the vessel. Finally, the desorption phase begins as the thermodynamic conditions are satisfied: the hydrogen dissociates from MH and begins to flow out of the tank.

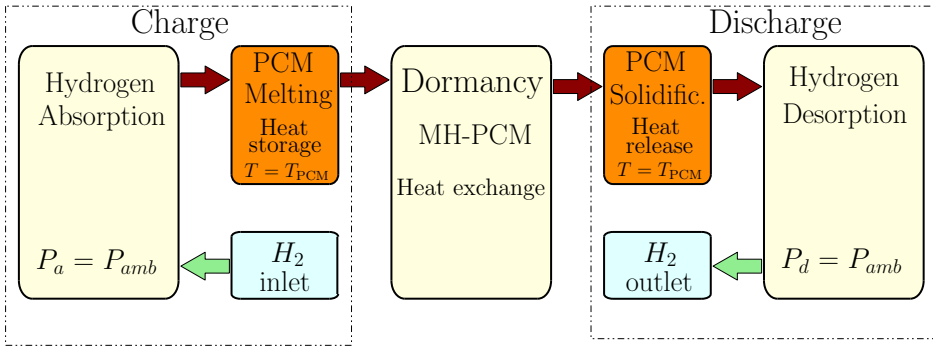


Figure 4.2: *The whole process in the MH-PCM storage system.*

4.2 Methodology

In this section we explore the mathematical methodology at the base of our study. In particular, we analyze the thermal exchange system, including geometrical/physical data, rationale, set of equations, and the domains discretization. Furthermore, we investigate the non-dimensionalization procedure employed to get the dimensionless parameters. Such parameters are crucial to evaluate several aspects of the whole process.

4.2.1 Mathematical model

By analyzing the governing equations of such a storage system [296], we evaluate for the absorption

$$\begin{cases} \frac{dm_{\mathrm{H}_2 g}}{dt} = f_{in,\mathrm{H}_2} - r m_{tot} \frac{MW_{\mathrm{H}_2} SC}{MW_{\mathrm{MH}}} \\ r = C_a e^{-\frac{E_a}{RT}} \ln \frac{P}{P_{eq}} (1 - \frac{m_{\mathrm{MH}}}{m_{tot}}) \\ \rho_{\mathrm{MH}} c_{p\mathrm{MH}} \frac{\partial T}{\partial t} = k_{\mathrm{MH}} \nabla^2 T + \dot{q}_a + f_{in,\mathrm{H}_2} c_{p\mathrm{H}_2} (T_{in,\mathrm{H}_2} - T) \frac{1}{V} \end{cases}, \tag{4.1}$$

and for the desorption

$$\begin{cases} \frac{dm_{\mathrm{H}_2 g}}{dt} = -f_{out,\mathrm{H}_2} - r m_{tot} \frac{MW_{\mathrm{H}_2} SC}{\mathrm{MW}_{\mathrm{MH}}} \\ r = C_d e^{-\frac{E_d}{RT}} \ln \frac{P - P_{eq}}{P_{eq}} (\frac{\mathrm{MW}_{\mathrm{MH}}}{m_{tot}}) \\ \rho_{\mathrm{MH}} c_{p\mathrm{MH}} \frac{\partial T}{\partial t} = k_{\mathrm{MH}} \nabla^2 T + \dot{q}_d \end{cases} . \tag{4.2}$$

In both cases, the first equation of the system represents the hydrogen conservation in gaseous form inside the vessel. Such ordinary differential equation considers the whole inner cylinder as control volume. In particular, the source terms are the inlet/outlet mass flow rate ($f_{in,\mathrm{H}_2}/f_{out,\mathrm{H}_2}$) and the overall absorbed/desorbed hydrogen calculated from the reaction rate (r), the total hydride mass (m_{tot}), the hydride and hydrogen molecular weights (MW_{MH}, MW_{H_2}) and the stoichiometric coefficient (SC). The second equation expresses r and involves typical reactions proportionality coefficients (C_a, C_d, E_a, E_d), and the universal gas constant (R). It is a partial differential equation that depends on hydrogen pressure (P), local temperature (T), equilibrium pressure (P_{eq}), and actual share of absorbed gas (being m_{MH} the time-dependent hydride mass). The reaction rate r definition is directly linked to the MH mass conservation

$$r = \frac{1}{m_{tot}} \frac{dm_{\mathrm{MH}}}{dt}. \tag{4.3}$$

With respect to P_{eq}, for absorption

$$P_{eq} = P_0 \, exp[\frac{\Delta H_a}{RT} - \frac{\Delta S_a}{R} + sl(\frac{m_{\mathrm{MH}}}{m_{tot}} - 0.5)], \tag{4.4}$$

while for desorption

$$P_{eq} = P_0 \, exp[-\frac{\Delta H_d}{RT} + \frac{\Delta S_d}{R} + sl(\frac{m_{\mathrm{MH}}}{m_{tot}} - 0.5)], \tag{4.5}$$

where P_0 is the reference pressure, ΔH_a and ΔS_a are the enthalpy/entropy variations for absorption reaction, ΔH_d and ΔS_d are the enthalpy/entropy variations for desorption reaction, as well as sl is the reaction plateau slope coefficient. Finally, the third equation is the energy conservation (Fourier law of conduction). The temporal variation of the local temperature is dependent on a conductive term ($k_{\mathrm{MH}}\nabla^2 T$), where k_{MH} is the MH thermal conductivity, and on a volumetric heat source term ($\dot{q}_a$, $\dot{q}_d$). Such term is made up of the heat generated as the reactions occur and is spatially distributed. ρ_{MH} and $c_{p\mathrm{MH}}$ are the MH density and specific heat, respectively. The MH conductivity k_{MH} and heat capacity $\rho_{\mathrm{MH}} c_{p\mathrm{MH}}$ are calculated as follows [216, 217]

$$k_{\mathrm{MH}} = \gamma k_{\mathrm{H_2}} + (1-\gamma) k_{\mathrm{m}}, \tag{4.6}$$

$$\rho_{\mathrm{MH}} c_{p\mathrm{MH}} = \gamma \rho_{\mathrm{H_2}} c_{p\mathrm{H_2}} + (1-\gamma) \rho_{\mathrm{m}} c_{p\mathrm{m}}, \tag{4.7}$$

where $\gamma = 0.5$ is the MH porosity, $k_{\mathrm{H_2}} = 0.185\,\mathrm{W/mK}$, $\rho_{\mathrm{H_2}} = 0.0899\,\mathrm{kg/m^3}$, $c_{p\mathrm{H_2}} = 14,300\,\mathrm{J/kgK}$ are the hydrogen conductivity, density and specific heat respectively and $k_{\mathrm{m}} = 2.0\,\mathrm{W/mK}$, $\rho_{\mathrm{m}} = 7260\,\mathrm{kg/m^3}$ and $c_{p\mathrm{m}} = 419\,\mathrm{J/kgK}$ are the $LaNi_5$ conductivity, density and specific heat.During absorption $\dot{q}_a$ is positive whereas during desorption $\dot{q}_d$ is negative. In each node

$$\dot{q_a} = -\Delta H_a r m_{tot} \frac{SC}{MW_{\mathrm{MH}}} \frac{1}{V}, \tag{4.8}$$

$$\dot{q_d} = +\Delta H_d r m_{tot} \frac{SC}{MW_{\mathrm{MH}}} \frac{1}{V}, \tag{4.9}$$

where V is the inner cylinder volume. (Note that ΔH_a is negative and ΔH_d is positive). We also have an additional term of heat exchange during absorption, which accounts for the difference between the inlet hydrogen temperature ($T_{in,\mathrm{H_2}}$) and the local temperature.

The second and third equations of the systems (4.1) and (4.2) are partial differential equations, which must be solved by means of an implicit scheme. To this aim, we express them according to the domains discretization. In particular, we evaluate a global equation for the whole MH tank (hydrogen mass conservation), and two additional equations in each node (local reaction rate and temperature). In the software implementation we use a Matlab's ode15s solver.

During dormancy, no reaction occurs and the energy conservation is the only active equation. This implies that the reaction kinetics equals

zero in each node and $\frac{dm_{H_2}}{dt} = 0$. During this phase, heat is still exchanged between the two materials and the temperatures slowly converge to a steady-state condition. Likewise, the gas pressure varies according to the ideal gas law.

4.2.2 Domains discretization

Due to the ideal axisymmetry, the discretization is equivalently carried out in a random direction between the center and the MH-PCM interface. Then, we make the assumption that no variable varies along the main axis of the canister, thus implying a favourable 1-D problem. The total number of nodes to discretize the MH-PCM storage system is $N_{TOT} = 110$.

Figure 4.3 shows the representation of the MH domain discretization, characterized by $N_{MH} = 50$ nodes. To substitute ∇T with a spatially discretized equation we use the central finite difference method, where Δb is the spatial distance between two consecutive nodes. Such discretization

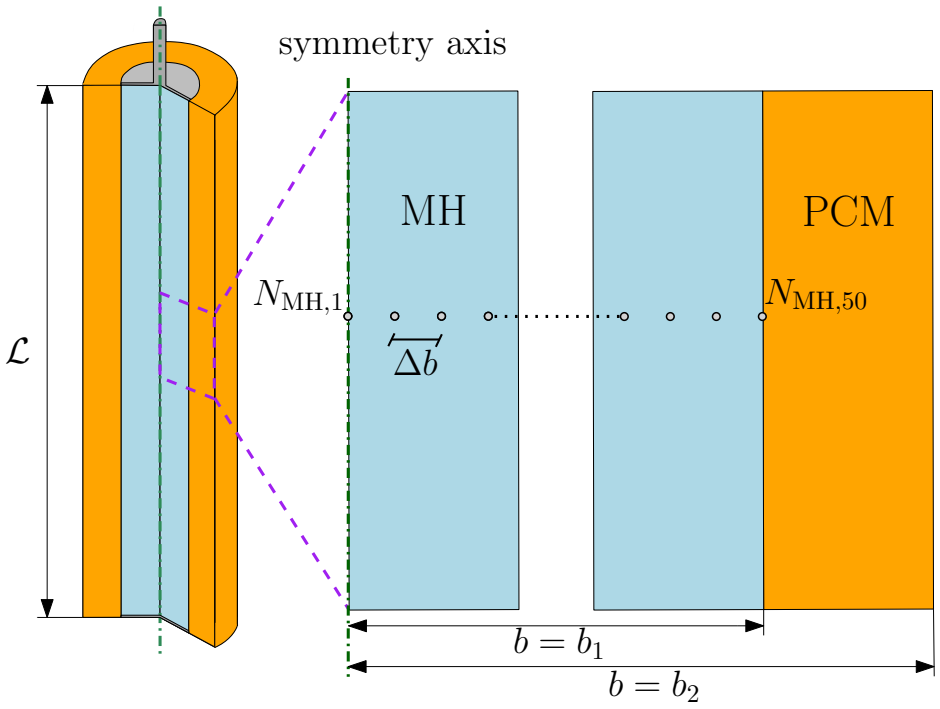


Figure 4.3: *The MH domain discretization [from $b = 0$ (vessel core) to $b = b_1$ (MH-PCM interface).]*

allows us to evaluate the local values of reaction rate r and temperature

T.

The PCM is not discretized in absorption because it exchanges heat with the MH, while melting with a constant temperature equal to solidification temperature (T_{sol}). For this reason, we consider PCM as a single node ($N_{\mathrm{PCM},a} = 1$) at $T_{\mathrm{PCM}} = T_{sol}$. Conversely, during desorption the PCM solidifies, thus mandating the discretization of its domain ($N_{\mathrm{PCM},d} = 60$). Also for the PCM domain, we adopt a finite central difference method. In this phase, the heat exchange varies from a convective to a conductive problem, thus implying that the PCM solidifies in the process. We adopt the PCM discretization model proposed in [297]. The authors use a variable space network, divided into two main regions. The first region between $b = b_1$ and $b = \epsilon$ considers the material at the solid state, being ϵ the solidification front. A second region between $b = \epsilon$ and $b = b_2$ considers the material at the liquid state. Figure 4.4 graphically shows the discretization scheme.

In addition to the standard Fourier's conduction equation, we consider an ad-hoc equation that represents the evolution of the solidification front. The coupling of two conduction laws at the interface (one for the solid region and one for the liquid region) leads to

$$\frac{d\epsilon}{dt} = \frac{1}{\rho_{\mathrm{PCM}}\lambda}\left[k_{\mathrm{PCM},s}\frac{\partial T_s}{\partial b}_{b=\epsilon} - k_{\mathrm{PCM},l}\frac{\partial T_l}{\partial b}_{b=\epsilon}\right], \tag{4.10}$$

where the s,l subscripts indicate solid and liquid regions respectively.

The solid region ($b < \epsilon$) is discretized with $N_{\mathrm{PCM},s} = 40$, whose relative distances increase as the solidification front progresses. Likewise, the liquid region ($b > \epsilon$) is discretized with $N_{\mathrm{PCM},l} = 20$, whose relative distances shrink as the solidification front progresses (Figure 4.4).

4.2.3 The heat exchange model

During the charge process, the convection is simulated by estimating the Nu number at the MH-PCM interface. The authors in [298] introduce the following Nu expression for a configuration similar to ours

$$\begin{aligned}\mathrm{Nu} = (2\theta)^{-0.5} + [0.35\mathrm{Ra}^{0.25} - (2\theta)^{-0.5}]* \\ * [1 + (0.0175\mathrm{Ra}^{3/4}\theta^{3/2})^{-2}]^{1/2},\end{aligned} \tag{4.11}$$

where $\theta = \mathrm{FoSt}$ is the non-dimensional time and Fo, St are the Fourier and Stefan numbers, respectively. Ra is the Rayleigh number. This function rapidly tends to a stationary value Nu_∞. Nevertheless, in [144] is

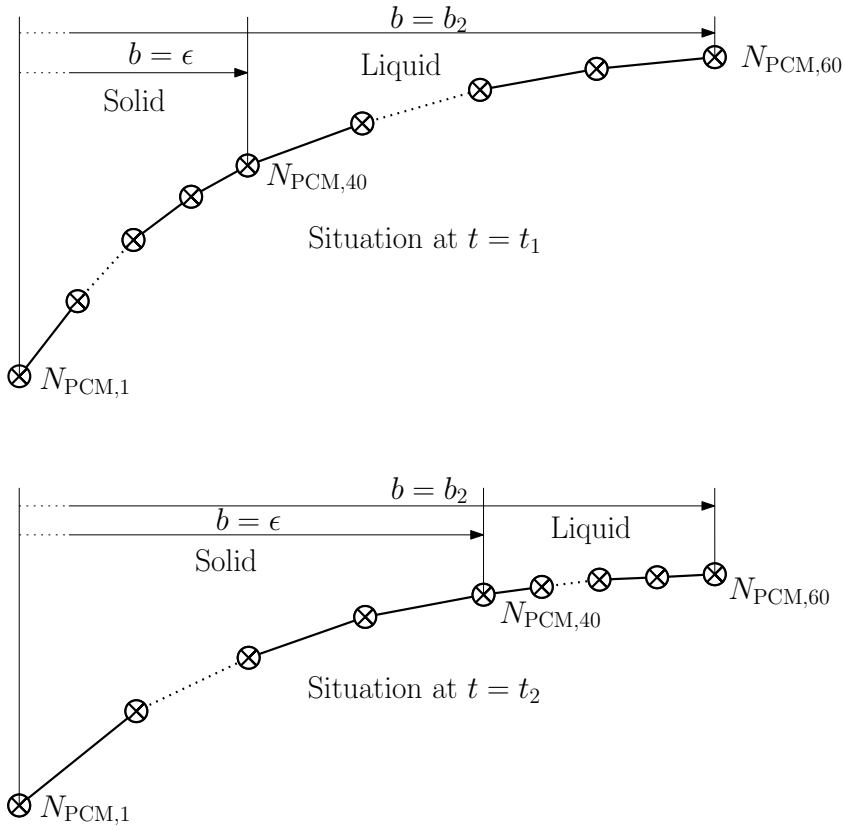


Figure 4.4: *Scheme of the discretized PCM domain at two different time steps, according to [297].*

demonstrated the we can safely assume $\text{Nu} = \text{Nu}_\infty$ for the whole temporal domain. Such assumption is valid because the difference between the two models is significant for a negligible period of time in case of a MH-PCM interface. Thus, we use the following, simpler expression

$$\text{Nu} = \frac{0.35\text{Ra}^{0.25}}{[1 + (0.143/\text{Pr})^{9/16}]^{4/9}} = \text{Nu}_\infty, \tag{4.12}$$

where Pr is the Prandtl number. From Nu we can directly estimate the convective heat exchange coefficient $h = \frac{\text{Nu}k_{\text{PCM}}}{\mathcal{L}}$, and thus determine the total heat flux exchanged at the interface. During dormancy, this equation is still valid and the whole system converges to a stationary condition. During the discharge process, we do not calculate Nu because the heat exchange has a conductive nature. The interface is therefore a simple discontinuity in thermal conductivity. Based on the above, we analyse the

power of the process ($\mathcal{P}$) only in the charge and discharge phases.

4.2.4 Non-dimensionalization of the problem

Finally, we employ a non-dimensional mathematical model to carry out a more general analysis of the above-mentioned physical problem. To this aim, we apply the Buckingham theorem to obtain 13 dimensionless numbers, which completely describe the physical phenomenon. The importance of the valve width is limited to the brief initial phase in which the flux is choked, thereby opposing to further hydrogen entering the canister. Due to the very short time typical of this phenomenon, the section of such valve (S_{valve}) is neglected during this process. Table 4.1 shows the non-dimensional parameters. The definition of all the non-dimensional numbers is univocal in the two phases, except for Π_9. In fact, Π_9 changes its definition between charge and discharge, due to the different heat exchange mechanism. For the absorption phase Π_9 is the PCM Pr number, while in the desorption phase Π_9 represents the non-dimensional PCM latent heat of fusion (λ^*).

4.3 Results

In this section we analyze the impact of several non-dimensional parameters on both the absorption and desorption phase. We consider a starting configuration where all the non-dimensional numbers are fixed based on the study [144]. Then, we vary separately Π_2, Π_7, Π_9, Π_{10}, Π_{11}, Π_{12}, whereas Π_1, Π_3, Π_4 are studied as control parameters. In particular, Π_1 is the non-dimensional equivalent power ($\mathcal{P}^*$). It is directly related to the inlet/outlet hydrogen mass flow rate. A high $\mathcal{P}^*$ indicates efficient charge/discharge processes. Π_3 is the Fo number and it suggests the total time needed for the reaction. Π_4 represents the canister state of charge (ϕ) and is equal to 0 when the canister is empty while it is equal to 1 when the canister is fully charged. All the variable non-dimensional numbers are ranged by carefully taking into exam the properties of various configurations and PCMs [141, 144, 204, 214, 215, 217], in order to retrieve the minimum and maximum plausible values for each of them.

Parameter	Definition	Denomination
Π_1	$\mathcal{P}\frac{d}{\alpha_{\mathrm{MH}}^3\rho_{MH}}\frac{1}{10^{18}}$	Equivalent power ($\mathcal{P}^*$)
Π_2	$\mathcal{L}/d$	Main aspect ratio
Π_3	$t\frac{\alpha_{\mathrm{MH}}}{d^2}$	Fourier number (Fo)
Π_4	$\frac{m_{\mathrm{H_2}}}{m_{\mathrm{H_2}}^{tot}}$	State of charge (ϕ)
Π_5	$\frac{m_{\mathrm{H_2}}^{tot}}{V\rho_{\mathrm{MH}}}$	Mass of H_2 stored
Π_6	$P_{eq}^{sol}\frac{d^2}{\alpha_{\mathrm{MH}}^2\rho_{\mathrm{MH}}}\frac{1}{10^{12}}$	Equilibrium pressure at T_{sol}
Π_7	P_{amb}/P_{eq}^{sol}	Ambient pressure
Π_8	$T_{sol}\frac{d^2c_{p\mathrm{MH}}}{\alpha_{\mathrm{MH}}^2}\frac{1}{10^{15}}$	Solidification temperature
Π_9	$\frac{\mu c_{p\mathrm{PCM}}}{k_{\mathrm{PCM}}}$	Prandtl number (Pr)
	$\lambda\frac{d^2}{\alpha_{PCM}^2}\frac{1}{10^{15}}$	Latent heat of the PCM (λ^*)
Π_{10}	$\frac{k_{\mathrm{PCM}}}{k_{\mathrm{MH}}}$	Thermal conductivities ratio
Π_{11}	$\frac{c_{p\mathrm{PCM}}}{c_{p\mathrm{MH}}}$	Specific heats ratio
Π_{12}	$\frac{\rho_{\mathrm{PCM}}}{\rho_{\mathrm{MH}}}$	Densities ratio

Table 4.1: *Non-dimensional parameters of the model.*

4.3.1 Absorption results

Figure 4.5 shows $\mathcal{P}^*$ as a function of ϕ for five different values of Π_2 ($\mathcal{L}/d$), with Fo in colorbar. From the figure we observe that over the whole ϕ interval, $\mathcal{P}^*$ is directly proportional to Π_2. Moreover, during the process Fo remains almost constant with the variation of Π_2, thus implying that

the canister is absorbing more hydrogen in the unit time. The results suggest that longer and thinner canisters exchange heat more efficiently with the PCM.

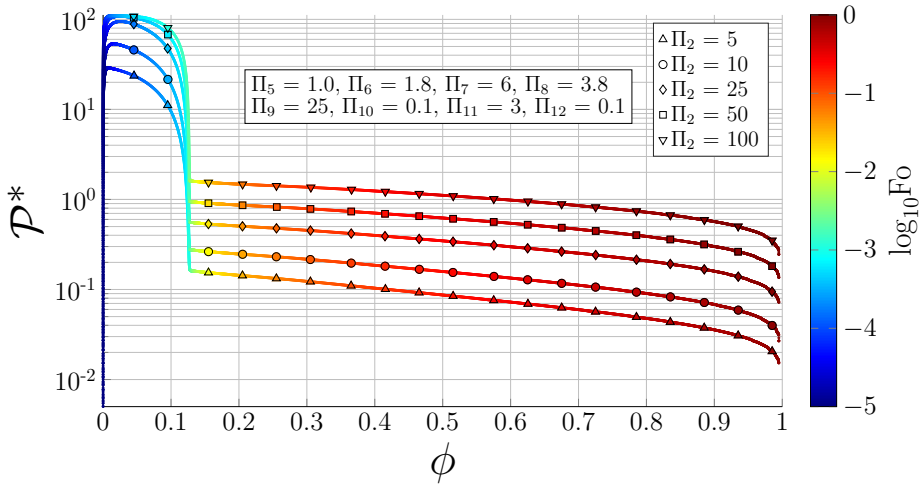


Figure 4.5: *$\mathcal{P}^*$ as a function of ϕ for different values of Π_2 in absorption with* Fo *in colorbar.*

Figure 4.6 shows $\mathcal{P}^*$ as a function of ϕ for five different values of Π_7. For increasing Π_7 (i.e. a higher inlet hydrogen pressure P_{amb}), we observe that $\mathcal{P}^*$ increases and Fo decreases over the whole process. The reduction of Fo is desirable because the same amount of hydrogen is absorbed in less time.

Figure 4.7 illustrates the impact of five different values of Π_9 (Pr) on $\mathcal{P}^*$. The impact is different along the process. In particular, for $0 \leq \phi \leq 0.12$ the curves overlap, whereas for $\phi > 0.12$ an increase of Pr slightly reduces $\mathcal{P}^*$. In fact, for $0 \leq \phi \leq 0.12$ the PCM does not affect the reaction because the hydride temperature is too low. As ϕ increases, more heat is developed and the hydride temperature raises. Thus, for $\phi > 0.12$, the PCM improves the reaction rate by absorbing heat from the hydride. In this case Fo is not deeply affected by the variation of Pr.

In Figure 4.8 we assess the trends of $\mathcal{P}^*$ for five different values of Π_{10}. Also this parameter has a significant impact only for $\phi > 0.12$. In this range a higher thermal conductivities ratio Π_{10} leads to a higher $\mathcal{P}^*$ because the PCM absorbs the reaction heat more efficiently. The reduced value of Fo implies that the canister is absorbing more hydrogen in less

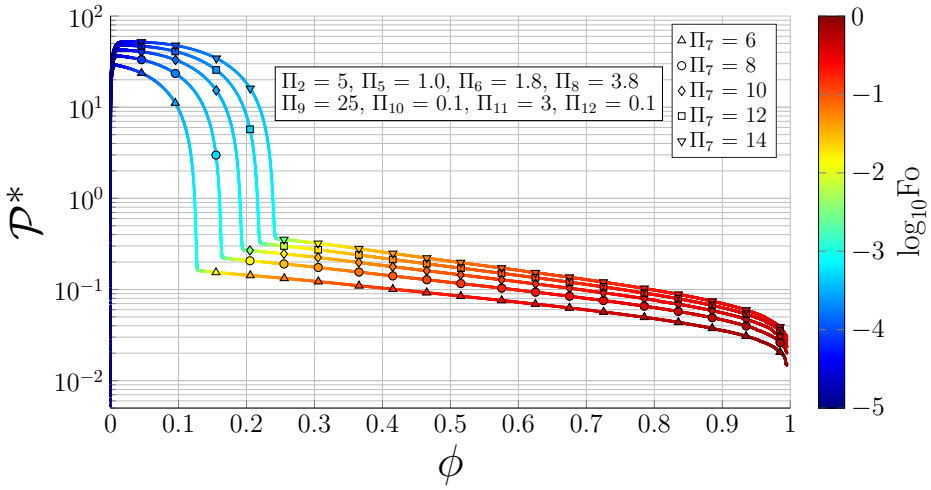


Figure 4.6: *$\mathcal{P}^*$ as a function of ϕ for different values of Π_7 in absorption with* Fo *in colorbar.*

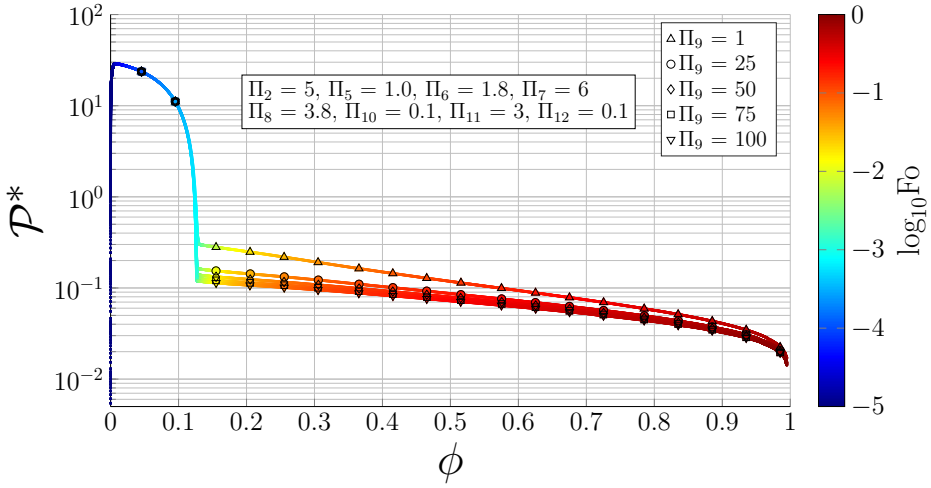


Figure 4.7: *$\mathcal{P}^*$ as a function of ϕ for different values of Π_9 in absorption with* Fo *in colorbar.*

time.

In Figure 4.9 we evaluate how the specific heats ratio Π_{11} affects $\mathcal{P}^*$. We can observe that a higher Π_{11} has a slightly positive effect even if the impact can be considered negligible.

Finally, Figure 4.10 shows that similarly to Π_{11}, also the densities ratio

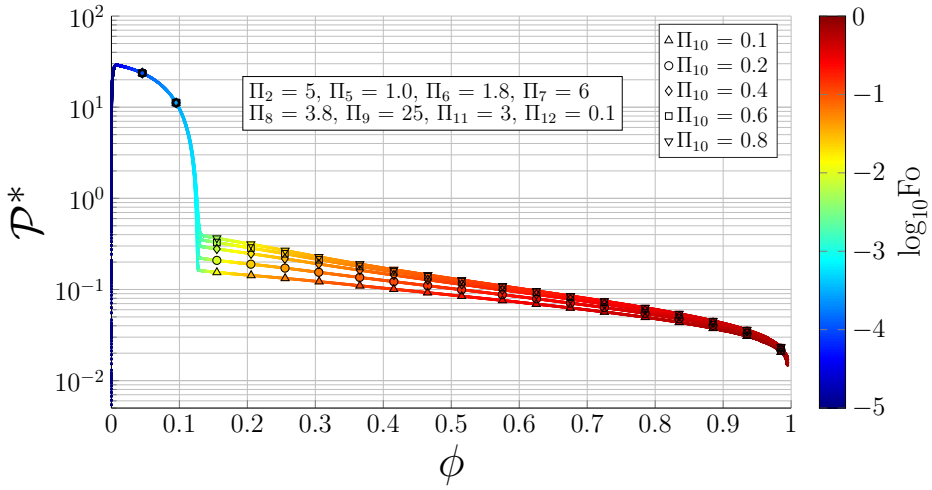


Figure 4.8: *$\mathcal{P}^*$ as a function of ϕ for different values of Π_{10} in absorption with* Fo *in colorbar.*

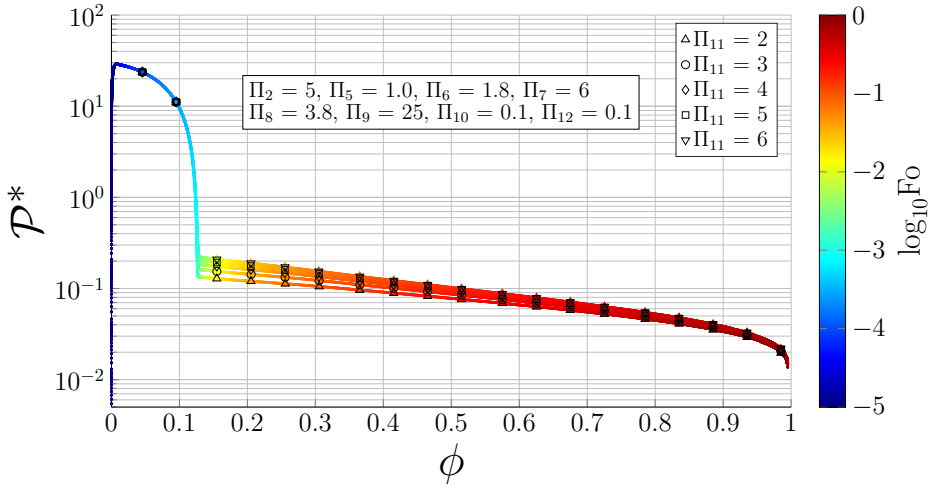


Figure 4.9: *$\mathcal{P}^*$ as a function of ϕ for different values of Π_{11} in absorption with* Fo *in colorbar.*

Π_{12} has an almost irrelevant impact on $\mathcal{P}^*$. For both these parameters the impact is less significant than Π_{10}, although an increase of Π_{12} is recommended in order to augment $\mathcal{P}^*$.

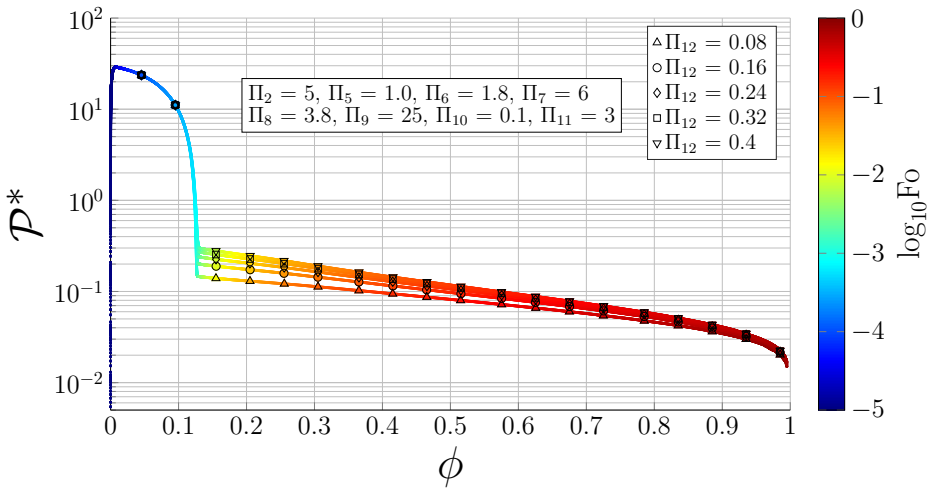


Figure 4.10: *$\mathcal{P}^*$ as a function of ϕ for different values of Π_{12} in absorption with* Fo *in colorbar.*

4.3.2 Desorption results

Figure 4.11 shows $\mathcal{P}^*$ as a function of ϕ for five different values of Π_2 in the desorption phase. As in absorption, higher values of Π_2 have positive effects on the process, leading to a more efficient heat exchange and a quicker discharge. Also in this case, Fo is nearly constant, suggesting that the canister is desorbing more hydrogen in the unit time.

In Figure 4.12 we note that the hydrogen outlet pressure Π_7 has a notable impact on the desorption phase efficiency. In fact, higher values of Π_7 reduce $\mathcal{P}^*$ over the whole ϕ interval. Basically, it is more difficult for the hydrogen gas to flow out of the canister if the ambient pressure is higher.

In Figure 4.13 we assess the trends of $\mathcal{P}^*$ for five different values of Π_9. Similarly to the absorption, also in desorption we note a first phase ($1 \geq \phi \geq 0.85$) where $\mathcal{P}^*$ is not dependent on Π_9 and the curves overlap and a second phase ($\phi < 0.85$) when they differ. For $\phi < 0.85$ $\mathcal{P}^*$ is positively affected by increasing values of Π_9. Such effect is due to the fact that the PCM intervenes in the reaction actively transferring heat to the MH.

Figure 4.14 shows $\mathcal{P}^*$ for five different values of Π_{10}. For $\phi < 0.85$ the impact of Π_{10} in desorption is significant. In fact, the heat exchange is

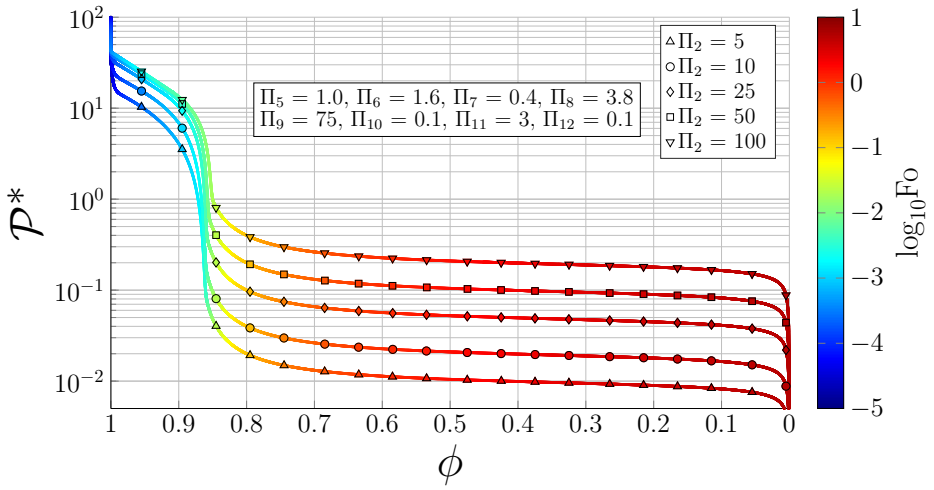


Figure 4.11: *$\mathcal{P}^*$ as a function of ϕ for different values of Π_2 in desorption with* Fo *in colorbar.*

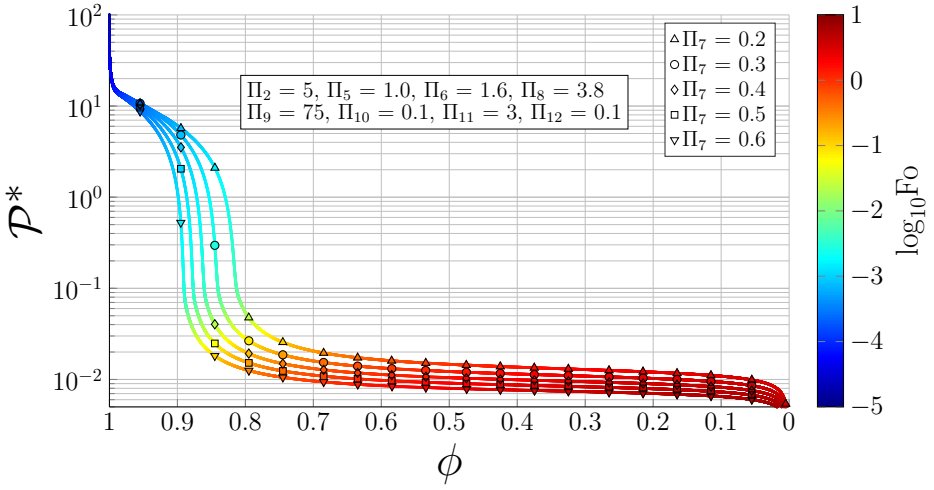


Figure 4.12: *$\mathcal{P}^*$ as a function of ϕ for different values of Π_7 in desorption with* Fo *in colorbar.*

now conduction-based and the thermal conductivity plays a direct role. Higher values of Π_{10} lead to an increased $\mathcal{P}^*$ and a decreased final Fo.

In Figure 4.15 and 4.16 we evaluate the effect of Π_{11} and Π_{12} on $\mathcal{P}^*$, respectively. For $\phi < 0.85$, in contrast to the absorption phase, $\mathcal{P}^*$ is

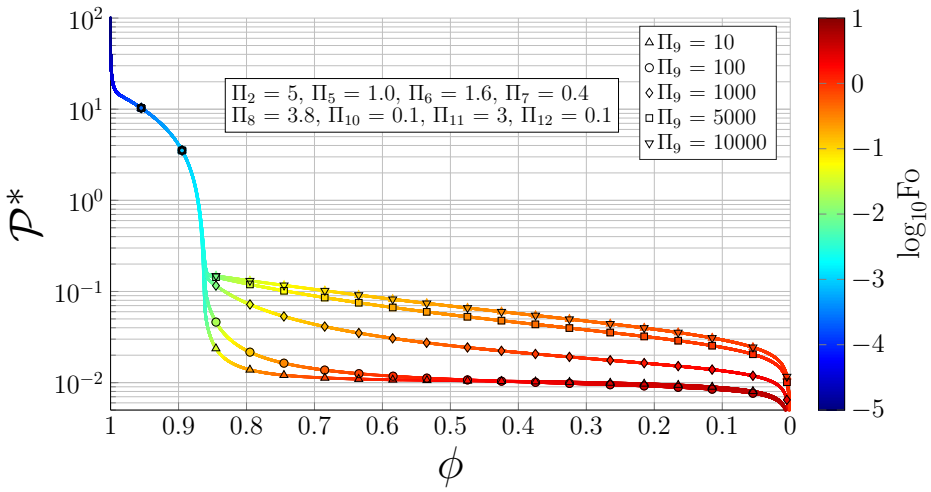


Figure 4.13: *$\mathcal{P}^*$ as a function of ϕ for different values of Π_9 in desorption with* Fo *in colorbar.*

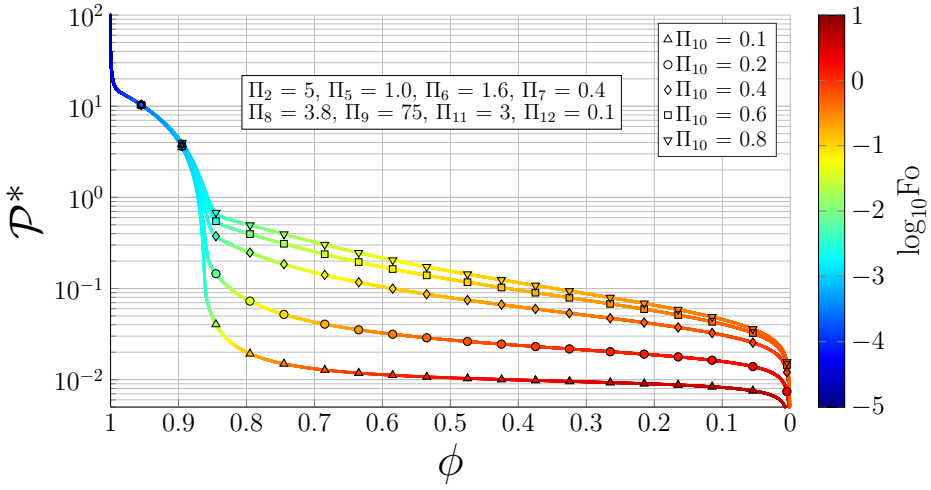


Figure 4.14: *$\mathcal{P}^*$ as a function of ϕ for different values of Π_{10} in desorption with* Fo *in colorbar.*

inversely proportional to both parameters. Such trends depend on the different nature of the heat exchange. However, the impact of Π_{11} and Π_{12} is almost negligible.

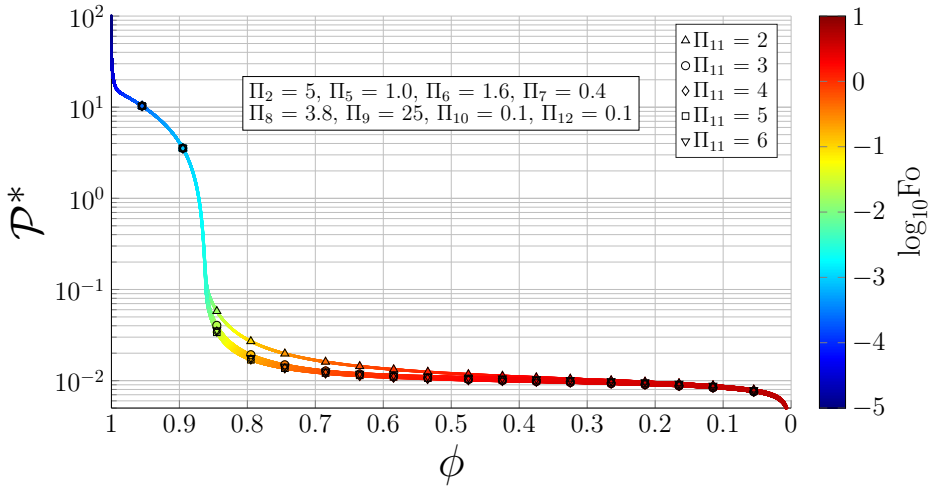


Figure 4.15: *$\mathcal{P}^*$ as a function of ϕ for different values of Π_{11} in desorption with* Fo *in colorbar.*

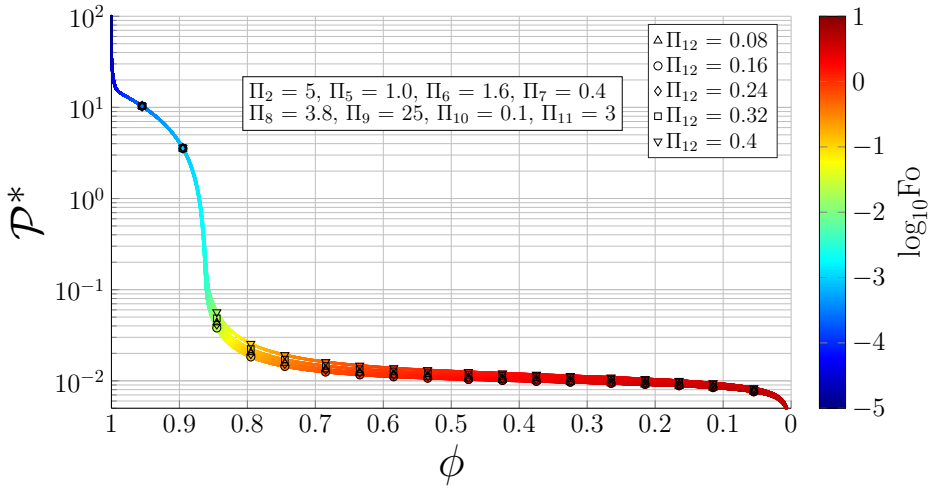


Figure 4.16: *$\mathcal{P}^*$ as a function of ϕ for different values of Π_{12} in desorption with* Fo *in colorbar.*

4.4 Discussion

According to Section 4.3 we observe that Π_2 ($\mathcal{L}/d$) and Π_{10} ($k_{\mathrm{PCM}}/k_{\mathrm{MH}}$) are the most significant non-dimensional parameters. Thus, to optimize the MH-PCM system operation we should use thin and long canisters, sur-

rounded by a PCM with a high value of the relative thermal conductivity. The efficiency of the processes is essentially enhanced thanks to a better heat exchange, which increases the reaction rate and the inlet/outlet hydrogen mass flow rate. Π_7 (P_{amb}/P_{eq}^{sol}) and Π_9 play an important role as well. However, Π_7 is mostly dependent on the operative conditions (especially during the discharge phase), whereas Π_9 has a real impact only in the desorption phase (when it is λ^*). In fact, we note that the latent heat of fusion of the PCM has a primary role on the desorption efficiency. Conversely, Π_9 (Pr), Π_{11} ($c_{p\mathrm{PCM}}/c_{p\mathrm{MH}}$) and Π_{12} ($\rho_{\mathrm{PCM}}/\rho_{\mathrm{MH}}$) have a minor role on the physical phenomena. Finally, the reactions are limited by the heat exchange with the PCM for $\phi > 0.12$ in absorption and for $\phi < 0.85$ in desorption. During the relatively short initial periods, the heat exchange non-dimensional parameters do not impact the operation and the different $\mathcal{P}^*$ curves coincide. Matter of fact, the MH temperature is too low (in absorption) or too high (in desorption) to limit the reaction rate and slow down the process. Thus, in this phase, the power (i.e. the mass flow rate) is only dependent on the reactions kinetics. The same observation can be made for the final stage of the reactions (the last 5 %), where the kinetics is predominant and drastically lowers the power. In conclusion, throughout the whole process the slope is dependent on the kinetics and is nearly constant in the central segment.

4.4.1 Case study

The goal of this section is to leverage the methodology proposed to determine an optimal configuration for a cylindrical MH-PCM hydrogen storage system. To this aim, we use $LaNi_5$ as MH since it is typically employed for this kind of applications [144]. Instead, the PCM must be further defined as one of the outcomes, in terms of physical properties that enhance the heat exchange. We also compare such optimal configuration with the baseline design used as reference in Section 4.3. For both configurations, we examine the charge/discharge time and power by fixing the amount of hydrogen to be absorbed (1 kWh of energy). In particular, 1 kWh of energy corresponds to 30 g of H_2. The $LaNi_5$ gravimetric density is equal to 1.28 %, therefore 2.34 kg of MH powder are needed. If we consider 34 % of the total volume as occupied by the powder, the canister volume required to store such amount of hydride is $8.60 \cdot 10^{-4}$ m^3. The free space is needed in order to account for the expansion phenomenon to

which the powder is subject during the absorption process and is a conservative percentage (conventionally, the threshold is set at 40 % [299]). In the optimal design, we select a canister with $\Pi_2 = 30$, being $\mathcal{L} = 99.48\,\text{cm}$ and $d = 3.32\,\text{cm}$. Π_5 is 1.0 whereas the other variable non-dimensional numbers (Π_7, Π_9, Π_{10}, Π_{11}, Π_{12}) are selected by analyzing the results of Section 4.3 and by retrieving the properties of the most efficient PCMs developed so far. Table 4.2 summarizes the non-dimensional configurations for the optimal and the baseline design.

Parameter	**Baseline Configuration**		**Optimal Configuration**	
	Absorption	Desorption	Absorption	Desorption
Π_2	5	5	30	30
Π_6	1.8	1.6	0.08	0.07
Π_7	6	0.4	1	0.03
Π_9	25	25	4.5	2.5
Π_{10}	0.1	0.1	0.3	0.6
Π_{11}	3	3	6.5	4
Π_{12}	0.1	0.1	0.25	0.3

Table 4.2: *Baseline and optimal non-dimensional configurations of the case study.*

The mathematical model and the numerical methodology are the same employed in Section 4.2 and the results are shown both through a non-dimensional (Figure 4.17) and a dimensional approach (Figure 4.18). Figure 4.17 shows the non-dimensional absorption and desorption phases for the optimal and the baseline configurations. The baseline design exhibits a higher charge and discharge power in a first brief phase, then the optimal design is more performing. Moreover, in both cases the final value of Fo for the optimal configuration is notably reduced, thus suggesting

a considerably quicker charge and discharge process. Figure 4.18 shows

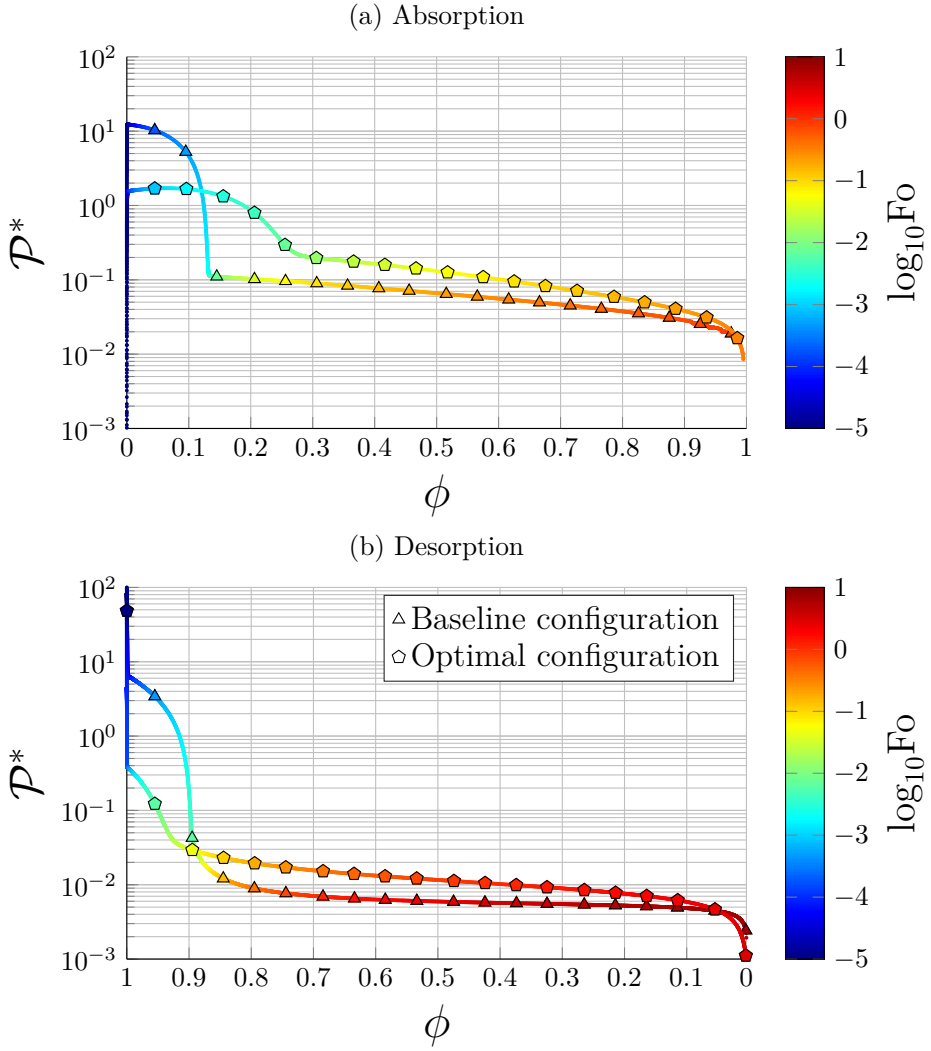


Figure 4.17: *Comparison between baseline and optimal configuration for the (a) Absorption phase and the (b) Desorption phase.*

the charge and discharge power as function of ϕ for the baseline and the optimal configurations in the absorption and the desorption phases. In absorption, the total time needed for the reaction decreases from 120 minutes to 9 minutes, with the correspondent average power increasing from 517.3 W to 7.05 kW. In desorption, the time decreases from 1100 minutes to 87 minutes, with the average power increasing from 55.7 W to 728.8 W.

Therefore, the enhancement is significant since the total time process is reduced from 1220 minutes to 97 minutes (i.e. a 92.1 % time reduction). We observe such improvement both in absorption and in desorption.

As for the selection of the PCM, $LiNO_3 - 3H_2O$ is a reasonable solution for such a configuration. In fact, due to the physical properties summarized in Table 4.3, it can easily achieve the non-dimensional values used in our case study. We use the exact same amount of PCM that is needed to store/transfer the heat released/required during the entire cycle. Therefore, such optimal MH-PCM configuration has a 14.4 kg_{H_2}/m^3 volumetric density, which can be achieved by a 180 bar pressure vessel at standard temperature. For comparison, the baseline design has a 8 kg_{H_2}/m^3 volumetric density.

	Liquid Phase	Solid Phase
Thermal conductivity k [W/mK]	0.58	1.32
Density ρ [kg/m^3]	1780	2140
Specific heat c_p [J/kgK]	2770	1730
Latent heat of fusion λ [J/kg]	296000	
Solidification temperature T_{sol} [K]	303	

Table 4.3: *Thermo-physical properties of* $LiNO_3 - 3H_2O$.

The difference in the volumetric density can be graphically appreciated in Figure 4.19, where it is plotted along with the temperature distribution of the MH-PCM system. The comparison between the two configurations highlights the enhancements of the optimization: the temperature is closer to the PCM solidification level while much less material has to be used in order to accomplish the discharge.

Note that, in the desorption phase, hydrogen is free to flow out with no restrictions or constraints. Thus, the mass flow rate is the highest physically possible at any time. Such a flow rate can indeed be limited in order to obtain a constant 1 kW power output for a longer period of time, for instance. This is particularly useful in stationary power gener-

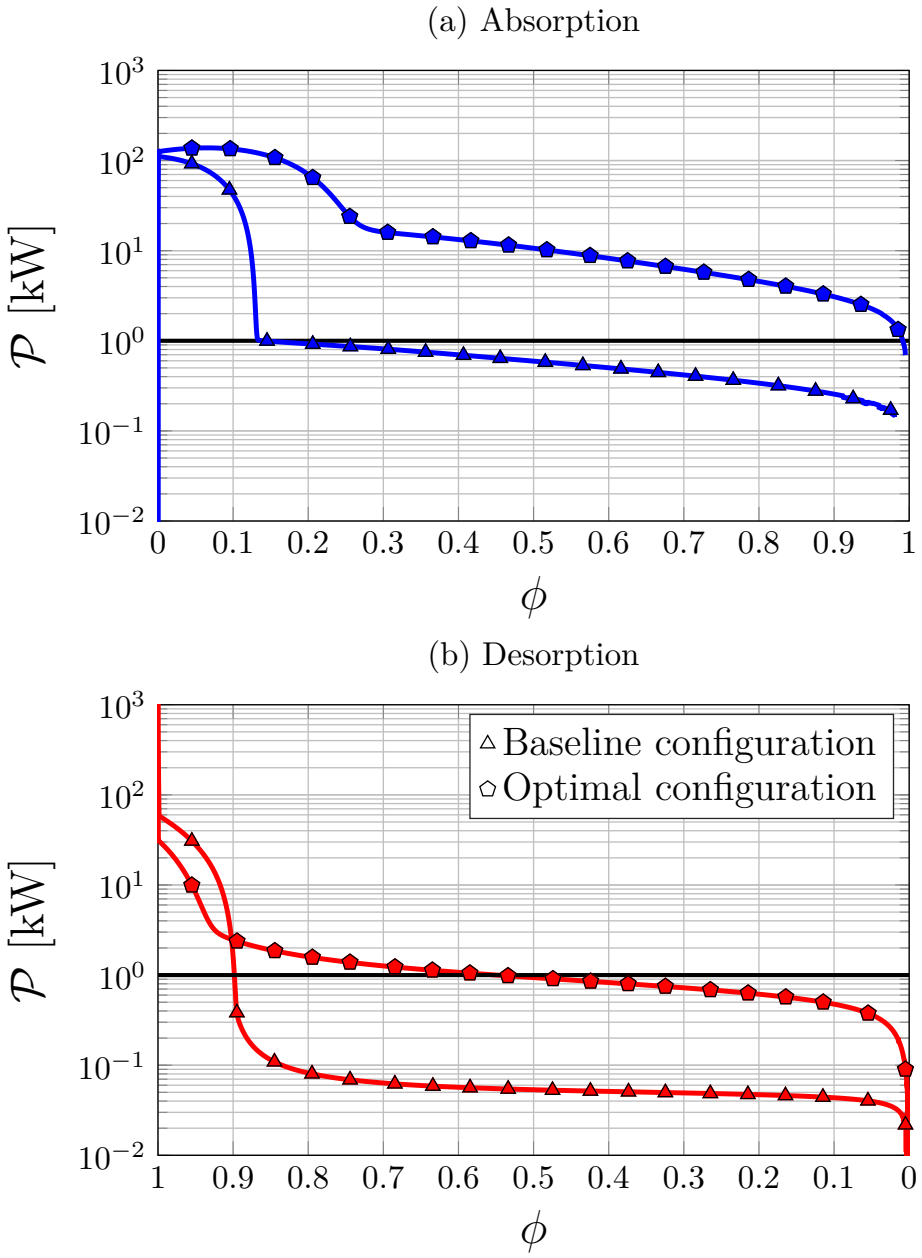


Figure 4.18: *Comparison between the baseline and the optimal configuration for the (a) Absorption phase and the (b) Desorption phase.*

ation systems and better represents the actual functioning of a practical application.

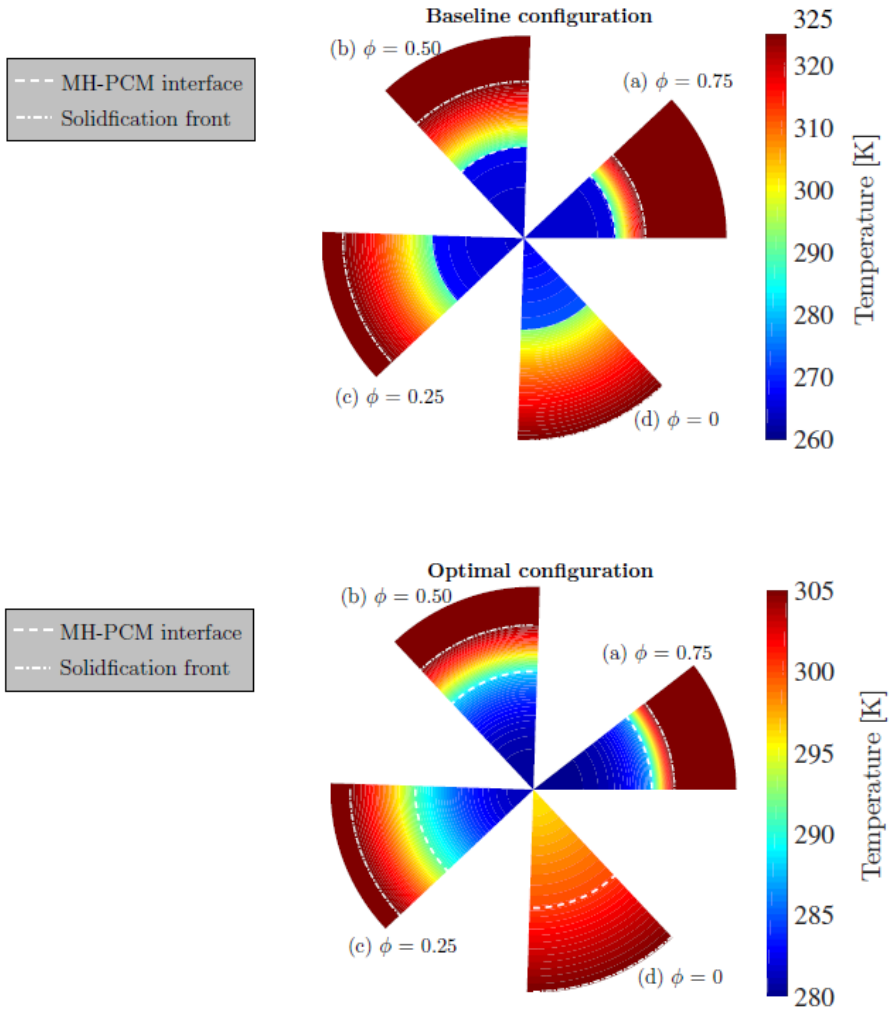


Figure 4.19: *Temperature distribution and solidification front evolution for 4 different values of ϕ in the baseline and optimal configuration.*

4.5 Summary

In this chapter we develop a flexible and versatile non-dimensional methodology to characterize the operation of different cylindrical MH-PCM storage tank layouts and to determine the optimal configuration, in terms of charge/discharge time and equivalent power. In particular, we utilize three sets of equations to study the absorption, the dormancy, and

the desorption phases, respectively. To analyze the impact of the temperature distribution on the system performance (i.e. the impact on the reaction rate), we discretize the MH-PCM axisymmetric geometry through the radial direction, neglecting border effects. In absorption the convective nature of the heat exchange allows us to consider the temperature constant for the liquid PCM. Conversely in desorption, due to the conductive nature of the heat transfer we discretize the PCM into two sub-domains: one solid and one liquid. We apply the Buckingham theorem to reduce the number of parameters which influence the physical phenomenon. By employing such procedure we obtain 13 non-dimensional numbers which totally describe the MH-PCM system operation.

We utilize such methodology to assess the impact of the salient geometrical and thermo-physical parameters on a baseline design MH-PCM system [144]. Then we evaluate and characterize the optimal configuration. According to the results, the main aspect ratio of the canister ($\mathcal{L}/d$) and the PCM relative thermal conductivity ($k_{\mathrm{PCM}}/k_{\mathrm{MH}}$) are the most influential parameters. In fact, we observe that thin and long canisters are more efficient at exchanging heat. Likewise, a high PCM relative thermal conductivity has a notable impact on the process, especially during desorption. The non-dimensional latent heat of fusion of the PCM (λ^*) follows as one of the most important parameter, although it only has an impact on the discharge phase. Finally, by starting from the baseline design we evaluate the optimal configuration, which is designed by analysing the impact of each of the non-dimensional parameters. Results show that a $LaNi_5/LiNO_3 - 3H_2O$ system for the storage of 1 kWh of H_2 exhibits 7.05 kW and 0.73 kW of average power in absorption and desorption, respectively. If compared with the baseline design, the optimal configuration is 92 % faster in absorption and desorption, since the total process time is reduced from 1220 minutes to 96 minutes.

This work fits into the heterogeneous field of the material-based hydrogen storage methods, with the aim to further characterize the functioning of the MH-PCM systems. For what concerns further possible applications, in our vision we could: (i) insert the optimal configuration in a more complex and wide environment (e.g. a multi-energy system), (ii) repeat the analysis for different shapes and geometry (e.g. the spherical geometry), (iii) remove the material constraint, in order to collect data on different metal hydrides (i.e. study the impact of the gravimetric density on the system performance), (iv) extend and complete the analysis by using a

enhanced PCM with carbon nanoparticles or metal foams.

Conclusions

This thesis studies through modeling, design, and optimization operations the performance and the economic and environmental benefits of innovative multi-energy systems. In particular, different aspects of individual elements are investigated with a broader perspective focused on their inclusion in a distributed generation context. All the analysed technologies show interesting potentialities in order to achieve the declared climate neutrality.

Chapter 1 evaluates the environmental and economic impact of the integration of a Li-Ion battery-based electricity storage in a residential context, for different climates and with different battery capacities. The results show that sizing the lithium-ion battery based on the variation of the self-consumed renewable energy yields a sustainable investment for all climates. In particular, a relative battery capacity $1.5\,\mathrm{h} < \Theta < 3.5\,\mathrm{h}$ is the best solution from an energy and economical point of view. The selected design criterion provides a pay back period between 1.8 years (moderate climate) and 4.7 years (cold climate). Moreover, from a techno-economic perspective, lithium-ion batteries are better suited for daily energy storage rather than seasonal storage. In fact, they efficiently fill the time lag between demand and production on a daily time scale. On the other hand, lithium-ion battery costs gathers unsustainable investments for seasonal storage also considering any foreseeable battery cost reduction. Optimized building-level battery storage cannot fill completely the temporal mismatch between production and usage. As a consequence, different technologies (e.g. electric mobility) should be also considered to locally consume all the energy produced by the photovoltaic.

Chapter 2 studies a comprehensive peer-to-peer charging strategy exploiting the existing infrastructure in a building environment. In particular, this condominium system for shared charge of electric vehicles implements a rule-based logic and a pricing policy aimed at the intelligent

use of the available energy and infrastructures. Such a system could be a crucial element of energy communities. Realistic case studies demonstrate the effectiveness of the proposed system, that lowers the cost of the electric vehicles charge and the grid usage. In particular, it is possible to reduce the energy community charging cost between 51% and 63% with respect to publicly available slow charging station (i.e. Enel X®), depending on the season and on charging strategy. Such results are obtained also reducing the energy withdrawn from a charge-dedicated electric line between 56% and 96% and increasing the photovoltaic self-consumption from 4% to 14%.

Chapter 3 assesses the conversion of a commercial electric moped (Askoll eS_3®) in a fuel cell hybrid-light electric vehicle. The optimal design of the components is found through an optimization methodology based on backward dynamic programming. Such optimal design and operation strategy can be also implemented with a rule-based approach. Results show that a system composed of a 1 kW proton exchange membrane fuel cell, a 2000 Sl metal hydride hydrogen tank, and a 240 Wh buffer battery can cover the same driving-range of the batteries in the electric moped (119 km). Such hybrid system occupies considerably less volume (almost 40 l) and has a negligibly higher mass. The free volume can be used to extend the driving-range up to almost three times the nominal value. Moreover, using high pressure composite tank it is possible to increase the mass energy density of the onboard energy storage, even if the compression can require up to 10 % of the hydrogen chemical energy. The fuel cell hybrid electric vehicle can be recharged with green hydrogen locally produced. In detail, a residential and a shared mobility scenarios in the small Italian city of Viterbo are analysed. In both cases, the local green hydrogen production from photovoltaic system is sufficient on a yearly basis to satisfy the mobility energy requirements.

Chapter 4 evaluates a non-dimensional methodology to characterize the operation of several cylindrical metal hydride-phase change material hydrogen storage tank layouts and to determine the optimal configuration in terms of charge/discharge time and power. Especially, the Buckingham theorem is used in order to obtain 13 non-dimensional parameters which completely describe the process. The proposed methodology is applied to assess the impact of such parameters on a baseline design metal hydride-phase change material system. According to the results, thin and long canisters are more efficient at exchanging heat. Likewise, a high value

of ratio between the thermal conductivity of the phase change material and the metal hydride has a notable impact on the process, especially during desorption. Moreover, Results show that a $LaNi_5/LiNO_3 - 3H_2O$ system for the storage of 1 kWh of H_2 exhibits 6.63 kW and 0.85 kW of average power in absorption and desorption, respectively. Such optimal configuration is 91 % faster in charge/discharge process respect to the baseline design, since the total time is reduced from 970 minutes to 85 minutes.

List of Figures

1 Example of multi-energy system. 6

1.1 Schematic representation of the main elements of the system. 18
1.2 Representation of the nZEB energy fluxes control logic. . . 21
1.3 Weekly appliances ad lighting consumption (u_{el}) of an apartment in the building. 22
1.4 Consumption deviation from phase average relative to (a) the data in Figures 1 of [218]; (b) the data in Figures 9 of [218]. 23
1.5 Modified weekly appliances ad lighting consumption ($u^*_{el,i}$) of an apartment in the building. 23
1.6 Zero-th order electrical circuit model of the battery [228]. . 25
1.7 Equivalent resistance of the battery as a function of the temperature and of the SoC. 26
1.8 Experimentally validated open-circuit voltage curves as a function of the SoC for different temperatures [228]. 27
1.9 Total building energy consumption as a function of time for (a) Cold climate; (b) Heating based climate; (c) Moderate climate; (d) Cooling based climate; (e) Hot climate. Numerical data can be found at 10.5281/zenodo.5816951. . 28
1.10 (a) Self-consumed energy as a function of Θ; (b) λ as a function of Θ. 31
1.11 (a) γ as a function Θ; (b) PayBack Period as a function of Θ. 33
1.12 D Frequency histograms: (a) Cold climate; (b) Heating based climate; (c) Moderate climate; (d) Cooling based climate; and (e) Hot climate. 36
1.13 State of Charge of the Li-Ion battery as a function of time for (a) Cold climate; (b) Heating based climate; (c) Moderate climate; (d) Cooling based climate; (e) Hot climate. . 37

2.1 Electric energy load in grey and unused electric energy in orange of an average apartment: a) yearly demand, b) demand of day 200 (summer), c) demand of day 50 (winter), and d) demand of day 300 (transitional). Data from the office of Energy Efficiency and Renewable Energy (EERE) [248]. 45
2.2 Scheme of the main elements of the condominium system for shared charge of electric vehicles. 46
2.3 Structure of the hardware of the charging system. 48
2.4 Wall-box: NEMA® 14-50 - 42 A, OpenEvse. 49
2.5 Logical structure of the charging system for the forecast part. 50
2.6 Logical structure of the charging system for the part of actual charge. 52
2.7 (a) Weekdays electric load frequency histogram for apartment 1, (b) Weekend days electric load frequency histogram for apartment 1. 54
2.8 (a) Weekdays electric load frequency histogram for apartment 2, (b) Weekend days electric load frequency histogram for apartment 2. 55
2.9 (a) Weekdays electric load frequency histogram for apartment 3, (b) Weekend days electric load frequency histogram for apartment 3. 56
2.10 Electric energy loads of the apartment 1 on weekday. Actual and forecast consumption in: (a) summer season, (b) transitional season, and (c) winter season. 57
2.11 Electric energy loads of the apartment 1 on weekend day. Actual and forecast consumption in: (a) summer season, (b) transitional season, and (c) winter season. 57
2.12 Electric energy loads of the apartment 2 on weekday. Actual and forecast consumption in: (a) summer season, (b) transitional season, and (c) winter season. 58
2.13 Electric energy loads of the apartment 2 on weekend day. Actual and forecast consumption in: (a) summer season, (b) transitional season, and (c) winter season. 58
2.14 Electric energy loads of the apartment 3 on weekday. Actual and forecast consumption in: (a) summer season, (b) transitional season, and (c) winter season. 59

2.15 Electric energy loads of the apartment 3 on weekend day. Actual and forecast consumption in: (a) summer season, (b) transitional season, and (c) winter season. 59

2.16 Percentage distribution curves of origin time and destination time on weekdays and weekend days [246]. 60

2.17 Economic results of the charging system serving a smart energy community of 3 users considering both the minimum cost (C_{min}) and the minimum time (T_{min}) behavioral patterns in summer season: (a) Charging costs, (b) Specific charging costs. 62

2.18 Economic results of the charging system serving a smart energy community of 3 users considering both the minimum cost (C_{min}) and the minimum time (T_{min}) behavioral patterns in transitional season: (a) Charging costs, (b) Specific charging costs. 63

2.19 Economic results of the charging system serving a smart energy community of 3 users considering both the minimum cost (C_{min}) and the minimum time (T_{min}) behavioral patterns in winter season: (a) Charging costs, (b) Specific charging costs. 64

2.20 Economic results of the charging system serving a smart energy community of 3 users that arrive at 1 PM considering both the (C_{min}) and the minimum time (T_{min}) behavioral patterns in summer season: (a) Charging costs, (b) Specific charging costs. 65

3.1 Schematic representation of the moped configurations: a) main elements of the e-moped, b) main elements of the FCH-LEV. 74

3.2 a) Class 1 WLTC speed profile; b) Class 1 WLTC acceleration profile. 77

3.3 Power to the wheel P_{W} (blue curve), power to the motor P_{M} (cyan curve), and primary power P_{P} (red curve) as a function of time for the driving cycle class 1 WLTC in Figure 3.2. 78

3.4 Experimental data of commercially available 1 kW and 2 kW air-cooled PEMFC stacks [275, 276]: a) consumed hydrogen mass flow rate ($\dot{m}_{H_2}$) versus electrical power (P_{FC}), b) efficiency (η_{FC}) versus electrical power (P_{FC}), and c) efficiency (η_{FC}) versus set-point (Φ_{FC}). 81
3.5 Optimized fuel cell power P_{FC} (orange curve) and buffer battery power P_{BB} (purple curve) as a function of time for the driving cycle class 1 WLTC in Figure 3.5. 83
3.6 Characterization of the buffer battery: a) produced energy from the fuel cell e_{FC} (orange curve), consumed energy from the moped e_{PB} (black curve), and quantity of stored energy c_{BB} (purple curve) as a function of time; b) state-of-charge as a function of time. 85
3.7 Required primary power P_P (red curve), required primary power with buffer battery P_{PB} (black curve), and primary power produced by the fuel cell P_{FCB} (magenta curve) as a function of time for the driving cycle class 1 WLTC in Figure 3.2. 89
3.8 Hourly energy consumption of an apartment in the city of Viterbo (heating based climate [224]). 90

4.1 The MH-PCM system configuration. 97
4.2 The whole process in the MH-PCM storage system. 98
4.3 The MH domain discretization [from $b = 0$ (vessel core) to $b = b_1$ (MH-PCM interface).] 101
4.4 Scheme of the discretized PCM domain at two different time steps, according to [297]. 103
4.5 $\mathcal{P}^*$ as a function of ϕ for different values of Π_2 in absorption with Fo in colorbar. 106
4.6 $\mathcal{P}^*$ as a function of ϕ for different values of Π_7 in absorption with Fo in colorbar. 107
4.7 $\mathcal{P}^*$ as a function of ϕ for different values of Π_9 in absorption with Fo in colorbar. 107
4.8 $\mathcal{P}^*$ as a function of ϕ for different values of Π_{10} in absorption with Fo in colorbar. 108
4.9 $\mathcal{P}^*$ as a function of ϕ for different values of Π_{11} in absorption with Fo in colorbar. 108

4.10 $\mathcal{P}^*$ as a function of ϕ for different values of Π_{12} in absorption with Fo in colorbar. 109
4.11 $\mathcal{P}^*$ as a function of ϕ for different values of Π_2 in desorption with Fo in colorbar. 110
4.12 $\mathcal{P}^*$ as a function of ϕ for different values of Π_7 in desorption with Fo in colorbar. 110
4.13 $\mathcal{P}^*$ as a function of ϕ for different values of Π_9 in desorption with Fo in colorbar. 111
4.14 $\mathcal{P}^*$ as a function of ϕ for different values of Π_{10} in desorption with Fo in colorbar. 111
4.15 $\mathcal{P}^*$ as a function of ϕ for different values of Π_{11} in desorption with Fo in colorbar. 112
4.16 $\mathcal{P}^*$ as a function of ϕ for different values of Π_{12} in desorption with Fo in colorbar. 112
4.17 Comparison between baseline and optimal configuration for the (a) Absorption phase and the (b) Desorption phase. . . 115
4.18 Comparison between the baseline and the optimal configuration for the (a) Absorption phase and the (b) Desorption phase. 117
4.19 Temperature distribution and solidification front evolution for 4 different values of ϕ in the baseline and optimal configuration. 118

List of Tables

1.1 Relevant properties of the selected building reported in the "Casaclima" energy certificate. 19
1.2 Relevant properties of the Li-Ion pouch cells, according to $IEC\,62660-1$ [223]. 19
1.3 Heating and Cooling Degrees Days and representative cities for each IEA climatic zone [224]. 20
1.4 Consumption data obtained, measured, and reported in the "Casaclima" energy certificate for the residential building in the Heating based climate. 24
1.5 Building energy consumption for each climate. 29
1.6 Relevant properties of the PV system as a fucntion of climate. 30
1.7 Average annual State of Charge and renewable electricity self consumption for $\Theta = 3.5\,\mathrm{h}$. 35

2.1 Specific energy costs based on the source. 50
2.2 Relevant properties of the selected electric vehicles [240, 256, 257]. 55
2.3 Selected origin and departure times on weekdays. 61
2.4 Selected origin and departure times on weekend days. . . . 61
2.5 Charge-dedicated electric line energy requirements aggregated for the three users. 67
2.6 Photovoltaic self-consumption percentage aggregated for the three users. 68

3.1 Relevant properties of the Askoll eS_3® [267]. 75
3.2 Relevant properties of the Askoll eS_3® batteries [268]. . . . 75
3.3 Characteristics of commercially available 1 kW and 2 kW air-cooled PEMFC stacks [275, 276]. 81

3.4 Characteristics of commercially available metal hydrides tanks [279] filled with AB_2 alloy. 82
3.5 Emissions of conventional means of transportation for yearly average commute of a student in Viterbo [291]. 90

4.1 Non-dimensional parameters of the model. 105
4.2 Baseline and optimal non-dimensional configurations of the case study. 114
4.3 Thermo-physical properties of $LiNO_3 - 3H_2O$. 116

Bibliography

[1] R. L. Arantegui, A. Jäger-Waldau, Photovoltaics and wind status in the european union after the paris agreement, Renewable and Sustainable Energy Reviews 81 (2018) 2460–2471.

[2] State of the union: Commission raises climate ambition and proposes 55% cut in emissions by 2030., Tech. rep., European Commission, https://ec.europa.eu/commission/presscorner/detail/en/IP_20_1599 Accessed on 10.11.2021.

[3] Committing to climate-neutrality by 2050: Commission proposes european climate law and consults on the european climate pact., Tech. rep., European Commission, https://ec.europa.eu/commission/presscorner/detail/en/ip_20_335 Accessed on 10.11.2021.

[4] Change, IPCC Climate and others, Mitigation of climate change, Contribution of working group III to the fifth assessment report of the intergovernmental panel on climate change 1454 (2014) 147.

[5] S. Solomon, G.-K. Plattner, R. Knutti, P. Friedlingstein, Irreversible climate change due to carbon dioxide emissions, Proceedings of the national academy of sciences 106 (6) (2009) 1704–1709.

[6] The European Parliament and the Council of the European Union, Directive 2012/27/eu of the european parliament and of the council of 25 october 2012 on energy efficiency, amending directives 2009/125/ec and 2010/30/eu and repealing directives 2004/8/ec and 2006/32/ec.

[7] Concerned Action Energy Performance of Buildings, http://www.epbd-ca.eu/ Accessed on 20.12.2021.

[8] Building Technologies Office, http://energy.gov/eere/efficiency/buildings Accessed on 20.12.2021.

[9] A. Mohammed, A. Ghaithan, A. Al-Hanbali, A. M. Attia, H. Saleh, O. Alsawafy, Performance evaluation and feasibility analysis of 10 kwp pv system for residential buildings in saudi arabia, Sustainable Energy Technologies and Assessments 51 (2022) 101920.

[10] L. Andreassi, M. Ciminelli, M. Feola, S. Ubertini, Innovative method for energy management: Modelling and optimal operation of energy systems.

[11] A. Franco, P. Salza, Strategies for optimal penetration of intermittent renewables in complex energy systems based on techno-operational objectives, Renew Energy (2011) 743–753.

[12] A. L. Facci, S. Ubertini, Meta-heuristic optimization for a high-detail smart management of complex energy systems, Energy Conversion and Management 160 (2018) 341–353.

[13] R. Cozzolino, L. Tribioli, G. Bella, Power management of a hybrid renewable system for artificial islands: a case study, Energy 106 (2016) 774–789.

[14] K. Lau, M. Yousof, S. Arshad, M. Anwari, A. Yatim, Performance analysis of hybrid photovoltaic/diesel energy system under malaysian conditions, Energy 35 (2010) 3245–55.

[15] A. L. Facci, V. Cigolotti, E. Jannelli, S. Ubertini, Technical and economic assessment of a sofc-based energy system for combined cooling, heating and power, Applied energy 192 (2017) 563–574.

[16] Building Technologies Office, Buildings, http://energy.gov/eere/efficiency/buildings Accessed on 20.12.2021.

[17] M. E. Biresselioglu, M. D. Kaplan, B. K. Yilmaz, Electric mobility in europe: A comprehensive review of motivators and barriers in decision making processes, Transportation Research Part A: Policy and Practice 109 (2018) 1–13.

[18] L. Q. Luu, E. R. Sanseverino, M. Cellura, H.-N. Nguyen, T. M. Nguyen, H. A. Nguyen, Comparative life cycle impact assessment of

electric and conventional bus in vietnam, Sustainable Energy Technologies and Assessments 54 (2022) 102873.

[19] X. Niu, Z. Zhan, B. Li, Z. Chen, Environmental governance and cleaner energy transition: Evaluating the role of environment friendly technologies, Sustainable Energy Technologies and Assessments 53 (2022) 102669.

[20] A. Barney, H. Polatidis, M. Jelić, N. Tomašević, G. Pillai, D. Haralambopoulos, Transition towards decarbonisation for islands: Development of an integrated energy planning platform and application, Sustainable Energy Technologies and Assessments 47 (2021) 101501.

[21] J. Koskela, A. Rautiainen, P. Järventausta, Using electrical energy storage in residential buildings–sizing of battery and photovoltaic panels based on electricity cost optimization, Applied energy 239 (2019) 1175–1189.

[22] C.-W. Lu, J.-C. Huang, C. Chen, M.-H. Shu, C.-W. Hsu, B. T. Bapu, An energy-efficient smart city for sustainable green tourism industry, Sustainable Energy Technologies and Assessments 47 (2021) 101494.

[23] H. Hashemi-Dezaki, S. M. M. Agah, H. Askarian-Abyaneh, H. Haeri-Khiavi, Sensitivity analysis of smart grids reliability due to indirect cyber-power interdependencies under various dg technologies, dg penetrations, and operation times, Energy Conversion and Management 108 (2016) 377–391.

[24] R. Bayindir, I. Colak, G. Fulli, K. Demirtas, Smart grid technologies and applications, Renewable and Sustainable Energy Reviews 66 (2016) 499–516.

[25] X. Yang, Y. Zhang, A comprehensive review on electric vehicles integrated in virtual power plants, Sustainable Energy Technologies and Assessments 48 (2021) 101678.

[26] H.-M. Groscurth, T. Bruckner, R. Kümmel, Modeling of energy-services supply systems, Energy 20 (9) (1995) 941–958.

[27] P. Mancarella, Mes (multi-energy systems): An overview of concepts and evaluation models, Energy 65 (2014) 1–17.

[28] T. Ackermann, G. Andersson, L. Soder, Distributed generation: a definition, Electric Power Systems Research (2001) 195–204.

[29] F. Franchetto, La generazione distribuita di energia: decentramento, smart grid e democrazia energetica.

[30] E. Shove, Time to rethink energy research, Nature Energy 6 (2) (2021) 118–120.

[31] Y. Zhang, X. Bai, F. P. Mills, J. C. Pezzey, Rethinking the role of occupant behavior in building energy performance: A review, Energy and Buildings 172 (2018) 279–294.

[32] G. Stuart, P. Fleming, V. Ferreira, P. Harris, Rapid analysis of time series data to identify changes in electricity consumption patterns in uk secondary schools, Building and Environment 42 (4) (2007) 1568–1580.

[33] A. L. Facci, L. Andreassi, S. Ubertini, Optimization of chcp (combined heat power and cooling) systems operation strategy using dynamic programming, Energy 66 (2014) 387–400.

[34] A. L. Facci, L. Andreassi, S. Ubertini, E. Sciubba, Analysis of the influence of thermal energy storage on the optimal management of a trigeneration plant, Energy procedia 45 (2014) 1295–1304.

[35] A. L. Facci, V. K. Krastev, G. Falcucci, S. Ubertini, Smart integration of photovoltaic production, heat pump and thermal energy storage in residential applications, Solar Energy 192 (2019) 133–143.

[36] A. L. Facci, S. Ubertini, Analysis of a fuel cell combined heat and power plant under realistic smart management scenarios, Applied Energy 216 (2018) 60–72.

[37] E. O'Shaughnessy, D. Cutler, K. Ardani, R. Margolis, Solar plus: Optimization of distributed solar pv through battery storage and dispatchable load in residential buildings, Applied Energy 213 (2018) 11–21.

[38] N. Kittner, F. Lill, D. M. Kammen, Energy storage deployment and innovation for the clean energy transition, Nature Energy 2 (9) (2017) 1–6.

[39] L. Tziovani, P. Kolios, L. Hadjidemetriou, E. Kyriakides, Energy scheduling in non-residential buildings integrating battery storage and renewable solutions, in: 2018 IEEE International Energy Conference (ENERGYCON), IEEE, 2018, pp. 1–6.

[40] D. Howell, B. Cunningham, T. Duong, P. Faguy, Overview of the doe vto advanced battery r&d program, Department of Energy.

[41] H. Chen, T. N. Cong, W. Yang, C. Tan, Y. Li, Y. Ding, Progress in electrical energy storage system: A critical review, Progress in natural science 19 (3) (2009) 291–312.

[42] C. Zhang, Y.-L. Wei, P.-F. Cao, M.-C. Lin, Energy storage system: Current studies on batteries and power condition system, Renewable and Sustainable Energy Reviews 82 (2018) 3091–3106.

[43] P. E. Campana, L. Cioccolanti, B. François, J. Jurasz, Y. Zhang, M. Varini, B. Stridh, J. Yan, Li-ion batteries for peak shaving, price arbitrage, and photovoltaic self-consumption in commercial buildings: A monte carlo analysis, Energy Conversion and Management 234 (2021) 113889.

[44] Y. Yang, S. Bremner, C. Menictas, M. Kay, Battery energy storage system size determination in renewable energy systems: A review, Renewable and Sustainable Energy Reviews 91 (2018) 109–125.

[45] W. Nam, J.-Y. Kim, K.-Y. Oh, The characterization of dynamic behavior of li-ion battery packs for enhanced design and states identification, Energy Conversion and Management 162 (2018) 264–275.

[46] I. Worighi, T. Geury, M. El Baghdadi, J. Van Mierlo, O. Hegazy, A. Maach, Optimal design of hybrid pv-battery system in residential buildings: End-user economics, and pv penetration, Applied Sciences 9 (5) (2019) 1022.

[47] J. Li, Optimal sizing of grid-connected photovoltaic battery systems for residential houses in australia, Renewable energy 136 (2019) 1245–1254.

[48] F. R. S. Sevilla, D. Parra, N. Wyrsch, M. K. Patel, F. Kienzle, P. Korba, Techno-economic analysis of battery storage and curtailment in a distribution grid with high pv penetration, Journal of Energy Storage 17 (2018) 73–83.

[49] M. Bortolini, M. Gamberi, A. Graziani, Technical and economic design of photovoltaic and battery energy storage system, Energy Conversion and Management 86 (2014) 81–92.

[50] M. Guezgouz, J. Jurasz, B. Bekkouche, T. Ma, M. S. Javed, A. Kies, Optimal hybrid pumped hydro-battery storage scheme for off-grid renewable energy systems, Energy Conversion and Management 199 (2019) 112046.

[51] A. Joseph, M. Shahidehpour, Battery storage systems in electric power systems, in: 2006 IEEE Power Engineering Society General Meeting, IEEE, 2006, pp. 8–pp.

[52] N. Garimella, N.-K. C. Nair, Assessment of battery energy storage systems for small-scale renewable energy integration, in: TENCON 2009-2009 IEEE region 10 conference, IEEE, 2009, pp. 1–6.

[53] R. Velik, The influence of battery storage size on photovoltaics energy self-consumption for grid-connected residential buildings, IJARER International Journal of Advanced Renewable Energy Research 2 (6).

[54] B. Nykvist, M. Nilsson, Rapidly falling costs of battery packs for electric vehicles, Nature climate change 5 (4) (2015) 329–332.

[55] D. D'agostino, P. Zangheri, L. Castellazzi, Towards nearly zero energy buildings in europe: A focus on retrofit in non-residential buildings, Energies 10 (1) (2017) 117.

[56] ECA, Energy efficiency in buildings: greater focus on cost-effectiveness still needed., https://op.europa.eu/webpub/eca/special-reports/energy-efficiency-11-2020/en/ Accessed on 20.12.2021.

[57] G. Merei, J. Moshövel, D. Magnor, D. U. Sauer, Optimization of self-consumption and techno-economic analysis of pv-battery systems in commercial applications, Applied Energy 168 (2016) 171–178.

[58] S. Antvorskov, Introduction to integration of renewable energy in demand controlled hybrid ventilation systems for residential buildings, Building and Environment 43 (8) (2008) 1350–1353.

[59] P. M. Congedo, C. Baglivo, D. D'Agostino, I. Zacà, Cost-optimal design for nearly zero energy office buildings located in warm climates, Energy 91 (2015) 967–982.

[60] M. Kapsalaki, V. Leal, M. Santamouris, A methodology for economic efficient design of net zero energy buildings, Energy and Buildings 55 (2012) 765–778.

[61] Y. Lu, S. Wang, K. Shan, Design optimization and optimal control of grid-connected and standalone nearly/net zero energy buildings, Applied Energy 155 (2015) 463–477.

[62] P. Chastas, T. Theodosiou, K. J. Kontoleon, D. Bikas, Normalising and assessing carbon emissions in the building sector: A review on the embodied co2 emissions of residential buildings, Building and Environment 130 (2018) 212–226.

[63] P. Chastas, T. Theodosiou, D. Bikas, Embodied energy in residential buildings-towards the nearly zero energy building: A literature review, Building and environment 105 (2016) 267–282.

[64] M. Conci, T. Konstantinou, A. van den Dobbelsteen, J. Schneider, Trade-off between the economic and environmental impact of different decarbonisation strategies for residential buildings, Building and Environment 155 (2019) 137–144.

[65] A. Martinez, S. D. de Garayo, P. Aranguren, D. Astrain, Assessing the reliability of current simulation of thermoelectric heat pumps for nearly zero energy buildings: Expected deviations and general guidelines, Energy Conversion and Management 198 (2019) 111834.

[66] S. Attia, P. Eleftheriou, F. Xeni, R. Morlot, C. Ménézo, V. Kostopoulos, M. Betsi, I. Kalaitzoglou, L. Pagliano, M. Cellura, et al., Overview and future challenges of nearly zero energy buildings (nzeb) design in southern europe, Energy and Buildings 155 (2017) 439–458.

[67] F. Asdrubali, I. Ballarini, V. Corrado, L. Evangelisti, G. Grazieschi, C. Guattari, Energy and environmental payback times for an nzeb retrofit, Building and Environment 147 (2019) 461–472.

[68] M. M. Sesana, G. Salvalai, Overview on life cycle methodologies and economic feasibility for nzebs, Building and Environment 67 (2013) 211–216.

[69] G. Tumminia, F. Guarino, S. Longo, D. Aloisio, S. Cellura, F. Sergi, G. Brunaccini, V. Antonucci, M. Ferraro, Grid interaction and environmental impact of a net zero energy building, Energy Conversion and Management 203 (2020) 112228.

[70] S. Cao, K. Sirén, Matching indices taking the dynamic hybrid electrical and thermal grids information into account for the decision-making of nzeb on-site renewable energy systems, Energy Conversion and Management 101 (2015) 423–441.

[71] D. D'Agostino, L. Mazzarella, What is a nearly zero energy building? overview, implementation and comparison of definitions, Journal of Building Engineering 21 (2019) 200–212.

[72] Y. Zhang, A. Lundblad, P. E. Campana, J. Yan, Employing battery storage to increase photovoltaic self-sufficiency in a residential building of sweden, Energy Procedia 88 (2016) 455–461.

[73] M. Akter, M. Mahmud, A. M. Oo, Comprehensive economic evaluations of a residential building with solar photovoltaic and battery energy storage systems: An australian case study, Energy and Buildings 138 (2017) 332–346.

[74] E. Tervo, K. Agbim, F. DeAngelis, J. Hernandez, H. K. Kim, A. Odukomaiya, An economic analysis of residential photovoltaic systems with lithium ion battery storage in the united states, Renewable and Sustainable Energy Reviews 94 (2018) 1057–1066.

[75] F. Cucchiella, I. D'adamo, M. Gastaldi, Photovoltaic energy systems with battery storage for residential areas: an economic analysis, Journal of Cleaner Production 131 (2016) 460–474.

[76] J. Liu, M. Wang, J. Peng, X. Chen, S. Cao, H. Yang, Techno-economic design optimization of hybrid renewable energy applications for high-rise residential buildings, Energy Conversion and Management 213 (2020) 112868.

[77] J. Liu, X. Chen, H. Yang, Y. Li, Energy storage and management system design optimization for a photovoltaic integrated low-energy building, Energy 190 (2020) 116424.

[78] M. Dijk, R. J. Orsato, R. Kemp, The emergence of an electric mobility trajectory, Energy policy 52 (2013) 135–145.

[79] H. Quak, N. Nesterova, T. van Rooijen, Possibilities and barriers for using electric-powered vehicles in city logistics practice, Transportation Research Procedia 12 (2016) 157–169.

[80] C. E. Maldonado, Implementing the Energy Performance of Buildings Directive (EPBD): Featuring Country Reports 2010, European Union, 2011.

[81] European Commission, Delivering the european green deal, https://ec.europa.eu/info/strategy/priorities-2019-2024/european-green-deal/delivering-european-green-deal_en Accessed on 28.02.2022 (july 2021).

[82] L. Rubino, C. Capasso, O. Veneri, Review on plug-in electric vehicle charging architectures integrated with distributed energy sources for sustainable mobility, Applied Energy 207 (2017) 438–464.

[83] International energy Agency, Global ev outlook 2021 - accelerating ambitions despite the pandemic, https://iea.blob.core.windows.net/assets/ed5f4484-f556-4110-8c5c-4ede8bcba637/GlobalEVOutlook2021.pdf Accessed on 28.02.2022 (April 2021).

[84] G. Duarte, C. Rolim, P. Baptista, How battery electric vehicles can contribute to sustainable urban logistics: A real-world application in lisbon, portugal, Sustainable Energy Technologies and Assessments 15 (2016) 71–78.

[85] M. Nour, S. M. Said, A. Ali, C. Farkas, Smart charging of electric vehicles according to electricity price, in: 2019 international conference on innovative trends in computer engineering (ITCE), IEEE, 2019, pp. 432–437.

[86] BNEF, Battery pack prices cited below 100 $/kwh for the first time in 2020, while market average sits at 137 $/kwh.

[87] A. Rosati, A. L. Facci, S. Ubertini, Techno-economic analysis of battery electricity storage towards self-sufficient buildings, Energy Conversion and Management 256 (2022) 115313.

[88] D. Sperling, N. Lutsey, Energy efficiency in passenger transportation, The Bridge 44 (3).

[89] M. Nilsson, B. Nykvist, Governing the electric vehicle transition–near term interventions to support a green energy economy, Applied energy 179 (2016) 1360–1371.

[90] Z. Jiao, L. Ran, J. Chen, H. Meng, C. Li, Data-driven approach to operation and location considering range anxiety of one-way electric vehicles sharing system, Energy Procedia 105 (2017) 2287–2294.

[91] P. A. Aguilar, B. Groß, Battery electric vehicles and fuel cell electric vehicles, an analysis of alternative powertrains as a mean to decarbonise the transport sector.

[92] G. Haddadian, M. Khodayar, M. Shahidehpour, Accelerating the global adoption of electric vehicles: barriers and drivers, The Electricity Journal 28 (10) (2015) 53–68.

[93] E. Azadfar, V. Sreeram, D. Harries, The investigation of the major factors influencing plug-in electric vehicle driving patterns and charging behaviour, Renewable and Sustainable Energy Reviews 42 (2015) 1065–1076.

[94] K. M. Tan, V. K. Ramachandaramurthy, J. Y. Yong, Integration of electric vehicles in smart grid: A review on vehicle to grid technologies and optimization techniques, Renewable and Sustainable Energy Reviews 53 (2016) 720–732.

[95] R. Danielis, Quale politiche per promuovere le automobile elettriche in italia? un commento.

[96] G. Putrus, P. Suwanapingkarl, D. Johnston, E. Bentley, M. Narayana, Impact of electric vehicles on power distribution networks, in: 2009 IEEE Vehicle Power and Propulsion Conference, IEEE, 2009, pp. 827–831.

[97] A. Boynuegri, M. Uzunoglu, O. Erdinç, E. Gokalp, A new perspective in grid connection of electric vehicles: Different operating modes for elimination of energy quality problems, Applied energy 132 (2014) 435–451.

[98] J. P. Martins, J. C. Ferreira, V. Monteiro, J. A. Afonso, J. L. Afonso, Iot and blockchain paradigms for ev charging system, Energies 12 (15) (2019) 2987.

[99] Evadoption, Stat of the week: Percent of households that rent by country, https://evadoption.com/stat-of-the-week-percent-of-households-that-rent-by-country/ Accessed on 28.02.2022.

[100] J. Axsen, S. Goldberg, J. Bailey, G. Kamiya, B. Langman, J. Cairns, M. Wolinetz, A. Miele, Electrifying vehicles: insights from the canadian plug-in electric vehicle study, Simon Fraser University, Vancouver, Canada.

[101] D. Lopez-Behar, M. Tran, J. R. Mayaud, T. Froese, O. E. Herrera, W. Merida, Putting electric vehicles on the map: A policy agenda for residential charging infrastructure in canada, Energy Research & Social Science 50 (2019) 29–37.

[102] S. Ayyadi, H. Bilil, M. Maaroufi, Optimal charging of electric vehicles in residential area, Sustainable Energy, Grids and Networks 19 (2019) 100240.

[103] A. Dubey, S. Santoso, Electric vehicle charging on residential distribution systems: Impacts and mitigations, IEEE Access 3 (2015) 1871–1893.

[104] S. Shao, M. Pipattanasomporn, S. Rahman, Challenges of phev penetration to the residential distribution network, in: 2009 IEEE Power & Energy Society General Meeting, IEEE, 2009, pp. 1–8.

[105] K. Clement-Nyns, E. Haesen, J. Driesen, The impact of charging plug-in hybrid electric vehicles on a residential distribution grid, IEEE Transactions on power systems 25 (1) (2009) 371–380.

[106] A. G. Boulanger, A. C. Chu, S. Maxx, D. L. Waltz, Vehicle electrification: Status and issues, Proceedings of the IEEE 99 (6) (2011) 1116–1138.

[107] A. Dubey, S. Santoso, M. P. Cloud, Understanding the effects of electric vehicle charging on the distribution voltages, in: 2013 IEEE Power & Energy Society General Meeting, IEEE, 2013, pp. 1–5.

[108] J. C. Gómez, M. M. Morcos, Impact of ev battery chargers on the power quality of distribution systems, IEEE transactions on power delivery 18 (3) (2003) 975–981.

[109] D. Oliveira, A. Z. De Souza, L. Delboni, Optimal plug-in hybrid electric vehicles recharge in distribution power systems, Electric Power Systems Research 98 (2013) 77–85.

[110] K. Mets, T. Verschueren, W. Haerick, C. Develder, F. De Turck, Optimizing smart energy control strategies for plug-in hybrid electric vehicle charging, in: 2010 IEEE/IFIP Network Operations and Management Symposium Workshops, Ieee, 2010, pp. 293–299.

[111] S. Shao, M. Pipattanasomporn, S. Rahman, Demand response as a load shaping tool in an intelligent grid with electric vehicles, IEEE Transactions on Smart Grid 2 (4) (2011) 624–631.

[112] S. Han, S. Han, K. Sezaki, Development of an optimal vehicle-to-grid aggregator for frequency regulation, IEEE Transactions on smart grid 1 (1) (2010) 65–72.

[113] E. Sortomme, M. A. El-Sharkawi, Optimal scheduling of vehicle-to-grid energy and ancillary services, IEEE Transactions on Smart Grid 3 (1) (2011) 351–359.

[114] C. Liu, K. K. Chai, E. T. Lau, Y. Wang, Y. Chen, Optimised electric vehicles charging scheme with uncertain user-behaviours in smart grids, in: 2017 IEEE 28th annual international symposium on personal, indoor, and mobile radio communications (PIMRC), IEEE, 2017, pp. 1–5.

[115] J. J. Escudero-Garzás, A. García-Armada, G. Seco-Granados, Fair design of plug-in electric vehicles aggregator for v2g regulation, IEEE Transactions on Vehicular Technology 61 (8) (2012) 3406–3419.

[116] T. Markel, M. Kuss, P. Denholm, Communication and control of electric drive vehicles supporting renewables, in: 2009 IEEE Vehicle Power and Propulsion Conference, IEEE, 2009, pp. 27–34.

[117] W. Shi, V. W. Wong, Real-time vehicle-to-grid control algorithm under price uncertainty, in: 2011 IEEE International Conference on Smart Grid Communications (SmartGridComm), IEEE, 2011, pp. 261–266.

[118] Y. He, B. Venkatesh, L. Guan, Optimal scheduling for charging and discharging of electric vehicles, IEEE transactions on smart grid 3 (3) (2012) 1095–1105.

[119] C. Jin, J. Tang, P. Ghosh, Optimizing electric vehicle charging: A customer's perspective, IEEE Transactions on vehicular technology 62 (7) (2013) 2919–2927.

[120] A. A. Panagopoulos, F. Christianos, M. Katsigiannis, K. Mykoniatis, G. Chalkiadakis, M. Pritoni, T. Peffer, O. P. Panagopoulos, E. S. Rigas, D. E. Culler, et al., iplugie: Intelligent electric vehicle charging in buildings with grid-connected intermittent energy resources, Simulation Modelling Practice and Theory 115 (2022) 102439.

[121] H. Liu, Y. Wang, Y. Wang, Z. Li, Strategic scheduling of pev charging load: A non-cooperative game model, in: 2017 36th Chinese Control Conference (CCC), IEEE, 2017, pp. 11284–11288.

[122] M. A. Masoum, S. M. Nabavi, Hybrid optimal online-overnight charging coordination of plug-in electric vehicles in smart grid, Journal of Power Sources 330 (2016) 7–17.

[123] A. Ovalle, A. Hably, S. Bacha, et al., Grid optimal integration of electric vehicles: Examples with Matlab implementation, Springer, 2018.

[124] G. Alkawsi, Y. Baashar, D. Abbas U, A. A. Alkahtani, S. K. Tiong, et al., Review of renewable energy-based charging infrastructure for electric vehicles, Applied Sciences 11 (9) (2021) 3847.

[125] W. Short, P. Denholm, Preliminary assessment of plug-in hybrid electric vehicles on wind energy markets, Tech. rep., National Renewable Energy Lab.(NREL), Golden, CO (United States) (2006).

[126] A. Haque, A. I. Saif, P. Nguyen, S. S. Torbaghan, Exploration of dispatch model integrating wind generators and electric vehicles, Applied energy 183 (2016) 1441–1451.

[127] K. E. Forrest, B. Tarroja, L. Zhang, B. Shaffer, S. Samuelsen, Charging a renewable future: The impact of electric vehicle charging intelligence on energy storage requirements to meet renewable portfolio standards, Journal of Power sources 336 (2016) 63–74.

[128] O. Ekren, C. H. Canbaz, Ç. B. Güvel, Sizing of a solar-wind hybrid electric vehicle charging station by using homer software, Journal of Cleaner Production 279 (2021) 123615.

[129] H. Fathabadi, Novel wind powered electric vehicle charging station with vehicle-to-grid (v2g) connection capability, Energy conversion and management 136 (2017) 229–239.

[130] M. O. Badawy, Y. Sozer, Power flow management of a grid tied pv-battery system for electric vehicles charging, IEEE Transactions on Industry Applications 53 (2) (2016) 1347–1357.

[131] D. Wu, H. Zeng, C. Lu, B. Boulet, Two-stage energy management for office buildings with workplace ev charging and renewable energy, IEEE Transactions on Transportation Electrification 3 (1) (2017) 225–237.

[132] G. Loreti, A. L. Facci, I. Baffo, S. Ubertini, Combined heat, cooling, and power systems based on half effect absorption chillers and polymer electrolyte membrane fuel cells, Applied Energy 235 (2019) 747–760.

[133] R. Peters, R. Deja, M. Engelbracht, M. Frank, L. Blum, D. Stolten, et al., Efficiency analysis of a hydrogen-fueled solid oxide fuel cell system with anode off-gas recirculation, Journal of Power Sources 328 (2016) 105–113.

[134] Y. Haseli, Maximum conversion efficiency of hydrogen fuel cells, international journal of hydrogen energy 43 (18) (2018) 9015–9021.

[135] J. O. Abe, A. Popoola, E. Ajenifuja, O. Popoola, Hydrogen energy, economy and storage: review and recommendation, International journal of hydrogen energy 44 (29) (2019) 15072–15086.

[136] L. Zhou, Progress and problems in hydrogen storage methods, Renewable and Sustainable Energy Reviews 9 (4) (2005) 395–408.

[137] J. Xiao, R. Peng, D. Cossement, P. Bénard, R. Chahine, Cfd model for charge and discharge cycle of adsorptive hydrogen storage on activated carbon, International journal of hydrogen energy 38 (3) (2013) 1450–1459.

[138] S. D. Patil, M. R. Gopal, Analysis of a metal hydride reactor for hydrogen storage, International Journal of Hydrogen Energy 38 (2) (2013) 942–951.

[139] S. Niaz, T. Manzoor, A. H. Pandith, Hydrogen storage: Materials, methods and perspectives, Renewable and Sustainable Energy Reviews 50 (2015) 457–469.

[140] L. Tong, Y. Yuan, T. Yang, P. Bénard, C. Yuan, J. Xiao, Hydrogen release from a metal hydride tank with phase change material jacket and coiled-tube heat exchanger, International Journal of Hydrogen Energy 46 (63) (2021) 32135–32148.

[141] H. El Mghari, J. Huot, J. Xiao, Analysis of hydrogen storage performance of metal hydride reactor with phase change materials, International Journal of Hydrogen Energy 44 (54) (2019) 28893–28908.

[142] B. Sakintuna, F. Lamari-Darkrim, M. Hirscher, Metal hydride materials for solid hydrogen storage: a review, International journal of hydrogen energy 32 (9) (2007) 1121–1140.

[143] S. D. Lewis, P. Chippar, Analysis of heat and mass transfer during charging and discharging in a metal hydride-phase change material reactor, Journal of Energy Storage 33 (2021) 102108.

[144] A. L. Facci, M. Lauricella, S. Succi, V. Villani, G. Falcucci, Optimized modeling and design of a pcm-enhanced h2 storage, Energies 14 (6) (2021) 1554.

[145] S. Z. Baykara, Hydrogen: A brief overview on its sources, production and environmental impact, International Journal of Hydrogen Energy 43 (23) (2018) 10605–10614.

[146] F. Piraino, P. Fragiacomo, A multi-method control strategy for numerically testing a fuel cell-battery-supercapacitor tramway, Energy Conversion and Management 225 (2020) 113481.

[147] P. Fragiacomo, F. Piraino, Vehicle-to-grid application with hydrogen-based tram, Energy Conversion and Management 250 (2021) 114915.

[148] H. S. Das, C. W. Tan, A. Yatim, Fuel cell hybrid electric vehicles: A review on power conditioning units and topologies, Renewable and Sustainable Energy Reviews 76 (2017) 268–291.

[149] K. V. Kordesch, G. R. Simader, Environmental impact of fuel cell technology, Chemical Reviews 95 (1) (1995) 191–207.

[150] C. Depcik, T. Cassady, B. Collicott, S. P. Burugupally, X. Li, S. S. Alam, J. R. Arandia, J. Hobeck, Comparison of lithium ion batteries, hydrogen fueled combustion engines, and a hydrogen fuel cell in powering a small unmanned aerial vehicle, Energy Conversion and Management 207 (2020) 112514.

[151] G. Oeschger, P. Carroll, B. Caulfield, Micromobility and public transport integration: The current state of knowledge, Transportation Research Part D: Transport and Environment 89 (2020) 102628.

[152] O. Korzilius, O. Borsboom, T. Hofman, M. Salazar, Optimal design of electric micromobility vehicles, arXiv preprint arXiv:2104.10155.

[153] C. Silva, At what extent the benefits of introducing alternative light-duty vehicles offset those of increasing the buses average occupancy?, Energy conversion and management 70 (2013) 211–219.

[154] A. Ewert, M. Brost, C. Eisenmann, S. Stieler, Small and light electric vehicles: An analysis of feasible transport impacts and opportunities for improved urban land use, Sustainability 12 (19) (2020) 8098.

[155] F. Liao, G. Correia, Electric carsharing and micromobility: A literature review on their usage pattern, demand, and potential impacts, International Journal of Sustainable Transportation (2020) 1–30.

[156] K. Hyvönen, P. Repo, M. Lammi, Light electric vehicles: substitution and future uses, Transportation Research Procedia 19 (2016) 258–268.

[157] N. Schelte, S. Severengiz, J. Schünemann, S. Finke, O. Bauer, M. Metzen, Life cycle assessment on electric moped scooter sharing, Sustainability 13 (15) (2021) 8297.

[158] The European Parliament and the Council of the European Union, Directive 2007/46/ec of the european parliament and of the council of 5 september 2007 establishing a framework for the approval of motor vehicles and their trailers, and of systems, components and separate technical units intended for such vehicles, Tech. rep., https://eur-lex.europa.eu/legal-content/EN/TXT/PDF/?uri=CELEX:32007L0046&from=EN, Accessed on 10.11.2021 (2007).

[159] E. Howe, F. J. Jakobsen, Unu global scooter sharing market report 2019, Tech. rep., Unu (2019).

[160] E. Howe, F. J. Jakobsen, Unu global scooter sharing market report 2020, Tech. rep., Unu (2020).

[161] T. Fletcher, K. Ebrahimi, The effect of fuel cell and battery size on efficiency and cell lifetime for an l7e fuel cell hybrid vehicle, Energies 13 (22) (2020) 5889.

[162] C. Zhai, F. Luo, Y. Liu, Cooperative power split optimization for a group of intelligent electric vehicles travelling on a highway with varying slopes, IEEE Transactions on Intelligent Transportation Systems.

[163] S. Lombardi, M. Villani, D. Chiappini, L. Tribioli, Cooling system energy consumption reduction through a novel all-electric powertrain traction module and control optimization, Energies 14 (1) (2021) 33.

[164] M. Sorrentino, V. Cirillo, L. Nappi, Development of flexible procedures for co-optimizing design and control of fuel cell hybrid vehicles, Energy Conversion and Management 185 (2019) 537–551.

[165] S. Ahmadi, S. Bathaee, A. H. Hosseinpour, Improving fuel economy and performance of a fuel-cell hybrid electric vehicle (fuel-cell, battery, and ultra-capacitor) using optimized energy management strategy, Energy Conversion and Management 160 (2018) 74–84.

[166] Z. Hu, J. Li, L. Xu, Z. Song, C. Fang, M. Ouyang, G. Dou, G. Kou, Multi-objective energy management optimization and parameter sizing for proton exchange membrane hybrid fuel cell vehicles, Energy Conversion and Management 129 (2016) 108–121.

[167] V. Paladini, T. Donateo, A. De Risi, D. Laforgia, Super-capacitors fuel-cell hybrid electric vehicle optimization and control strategy development, Energy conversion and management 48 (11) (2007) 3001–3008.

[168] A. L. Facci, L. Andreassi, F. Martini, S. Ubertini, Comparing energy and cost optimization in distributed energy systems management, Journal of Energy Resources Technology 136 (3) (2014) 032001.

[169] A. Hawkes, M. Leach, Cost-effective operating strategy for residential micro-combined heat and power, Energy 32 (5) (2007) 711–723.

[170] L. Tribioli, R. Cozzolino, L. Evangelisti, G. Bella, Energy management of an off-grid hybrid power plant with multiple energy storage systems, Energies 9 (8) (2016) 661.

[171] L. Bartolucci, S. Cordiner, V. Mulone, M. Santarelli, P. Lombardi, C. Wenge, B. Arendarski, P. Komarnicki, Grid service potential from optimal sizing and scheduling the charging hub of a commercial electric vehicle fleet, in: 2020 IEEE International Conference on Environment and Electrical Engineering and 2020 IEEE Industrial and Commercial Power Systems Europe (EEEIC/I&CPS Europe), IEEE, 2020, pp. 1–6.

[172] M. Alparone, M. Minutillo, M. Migliaccio, E. Jannelli, N. Massarotti, Hydrogen-based hybrid power unit for light vehicles: Assessment of energy performance and radiated electromagnetic emissions, Il nuovo cimento C 41 (6) (2018) 1–8.

[173] A. Buono, P. Di Trolio, M. Minutillo, M. Migliaccio, E. Jannelli, N. Massarotti, F. Conventi, C. Di Donato, F. Nunziata, L. Vanoli, et al., Hydrogen-bike equipped with hybrid power unit: Energy performance analysis and electromagnetic emissions test.

[174] P. Di Giorgio, P. Di Trolio, E. Jannelli, M. Minutillo, F. V. Conte, Model based preliminary design and optimization of internal combustion engine and fuel cell hybrid electric vehicle, Energy Procedia 148 (2018) 1191–1198.

[175] A. Shmaryahu, N. Amar, A. Ivanov, I. Aharon, Sizing procedure for system hybridization based on experimental source modeling for electric vehicles, Energies 14 (17) (2021) 5275.

[176] G. Di Ilio, P. Di Giorgio, L. Tribioli, G. Bella, E. Jannelli, Preliminary design of a fuel cell/battery hybrid powertrain for a heavy-duty yard truck for port logistics, Energy Conversion and Management 243 (2021) 114423.

[177] Suzuki, MET POLICE TRIALS HYDROGEN FUEL CELL BURGMAN, https://bikes.suzuki.co.uk/news/suzuki-hydrogen-fuel-cell-burgman-trialled-by-met-police/ Accessed on 10.11.2021.

[178] Atena, The hydrogen-powered electric scooter, https://www.atenaweb.com/en/hyscooter/ Accessed on 10.11.2021.

[179] M. R. Gopal, S. S. Murthy, Prediction of heat and mass transfer in annular cylindrical metal hydride beds, International Journal of Hydrogen Energy 17 (10) (1992) 795–805.

[180] A. Jemni, S. B. Nasrallah, J. Lamloumi, A. P. Guegan, Study of heat and mass transfer in a metal-hydrogen reactor, Zeitschrift für Physikalische Chemie 183 (1-2) (1994) 197–203.

[181] F. Askri, A. Jemni, S. B. Nasrallah, Study of two-dimensional and dynamic heat and mass transfer in a metal–hydrogen reactor, International Journal of Hydrogen Energy 28 (5) (2003) 537–557.

[182] B. Talaganis, G. Meyer, P. Aguirre, Modeling and simulation of absorption–desorption cyclic processes for hydrogen storage-compression using metal hydrides, International journal of hydrogen energy 36 (21) (2011) 13621–13631.

[183] H.-G. Kang, E.-S. Lee, S. Cho, M. H. Chang, S.-H. Yun, M.-Y. Ahn, K. J. Jung, H. Chung, M. Shim, K.-M. Song, et al., Thermo-hydraulic analysis on in-bed calorimetry in a thin double-layered annulus metal hydride bed, Fusion engineering and design 84 (2-6) (2009) 989–992.

[184] C. Chung, C.-J. Ho, Thermal–fluid behavior of the hydriding and dehydriding processes in a metal hydride hydrogen storage canister, international journal of hydrogen energy 34 (10) (2009) 4351–4364.

[185] A. Jemni, S. B. Nasrallah, J. Lamloumi, Experimental and theoretical study of ametal–hydrogen reactor, International Journal of Hydrogen Energy 24 (7) (1999) 631–644.

[186] Z. Bao, Z. Wu, S. N. Nyamsi, F. Yang, Z. Zhang, Three-dimensional modeling and sensitivity analysis of multi-tubular metal hydride reactors, Applied thermal engineering 52 (1) (2013) 97–108.

[187] E. I. Gkanas, M. Khzouz, G. Panagakos, T. Statheros, G. Mihalakakou, G. I. Siasos, G. Skodras, S. S. Makridis, Hydrogenation behavior in rectangular metal hydride tanks under effective heat management processes for green building applications, Energy 142 (2018) 518–530.

[188] Z. Wu, F. Yang, Z. Zhang, Z. Bao, Magnesium based metal hydride reactor incorporating helical coil heat exchanger: simulation study and optimal design, Applied energy 130 (2014) 712–722.

[189] H. Wang, A. K. Prasad, S. G. Advani, Hydrogen storage system based on hydride materials incorporating a helical-coil heat exchanger, International journal of hydrogen energy 37 (19) (2012) 14292–14299.

[190] L. Tong, J. Xiao, T. Yang, P. Bénard, R. Chahine, Complete and reduced models for metal hydride reactor with coiled-tube heat exchanger, International Journal of Hydrogen Energy 44 (30) (2019) 15907–15916.

[191] C. A. Krokos, D. Nikolic, E. S. Kikkinides, M. C. Georgiadis, A. K. Stubos, Modeling and optimization of multi-tubular metal hydride beds for efficient hydrogen storage, international journal of hydrogen energy 34 (22) (2009) 9128–9140.

[192] M. Bhouri, I. Bürger, M. Linder, Numerical investigation of hydrogen charging performance for a combination reactor with embedded metal hydride and coolant tubes, International Journal of Hydrogen Energy 40 (20) (2015) 6626–6638.

[193] F. Askri, M. B. Salah, A. Jemni, S. B. Nasrallah, Optimization of hydrogen storage in metal-hydride tanks, International journal of hydrogen Energy 34 (2) (2009) 897–905.

[194] C. Veerraju, M. R. Gopal, Heat and mass transfer studies on plate fin-and-elliptical tube type metal hydride reactors, Applied thermal engineering 30 (6-7) (2010) 673–682.

[195] J. Ma, Y. Wang, S. Shi, F. Yang, Z. Bao, Z. Zhang, Optimization of heat transfer device and analysis of heat & mass transfer on the finned multi-tubular metal hydride tank, International journal of hydrogen energy 39 (25) (2014) 13583–13595.

[196] C. Chung, S.-W. Yang, C.-Y. Yang, C.-W. Hsu, P.-Y. Chiu, Experimental study on the hydrogen charge and discharge rates of metal hydride tanks using heat pipes to enhance heat transfer, Applied energy 103 (2013) 581–587.

[197] C. Chung, Y.-Z. Chen, Y.-P. Chen, M.-S. Chang, Cfd investigation on performance enhancement of metal hydride hydrogen storage vessels using heat pipes, Applied Thermal Engineering 91 (2015) 434–446.

[198] F. A. Elhamshri, M. Kayfeci, Enhancement of hydrogen charging in metal hydride-based storage systems using heat pipe, International Journal of Hydrogen Energy 44 (34) (2019) 18927–18938.

[199] I. Dincer, M. A. Rosen, Thermal energy storage systems and applications, John Wiley & Sons, 2021.

[200] H. Nazir, M. Batool, F. J. B. Osorio, M. Isaza-Ruiz, X. Xu, K. Vignarooban, P. Phelan, A. M. Kannan, et al., Recent developments in phase change materials for energy storage applications: A review, International Journal of Heat and Mass Transfer 129 (2019) 491–523.

[201] S. Garrier, B. Delhomme, P. De Rango, P. Marty, D. Fruchart, S. Miraglia, A new mgh2 tank concept using a phase-change material to store the heat of reaction, International journal of hydrogen energy 38 (23) (2013) 9766–9771.

[202] A. A. R. Darzi, H. H. Afrouzi, A. Moshfegh, M. Farhadi, Absorption and desorption of hydrogen in long metal hydride tank equipped with phase change material jacket, international journal of hydrogen energy 41 (22) (2016) 9595–9610.

[203] H. B. Maad, F. Askri, S. B. Nasrallah, Heat and mass transfer in a metal hydrogen reactor equipped with a phase-change heat-exchanger, International Journal of Thermal Sciences 99 (2016) 271–278.

[204] H. El Mghari, J. Huot, L. Tong, J. Xiao, Selection of phase change materials, metal foams and geometries for improving metal hydride performance, International Journal of Hydrogen Energy 45 (29) (2020) 14922–14939.

[205] P. Marty, P. de Rango, B. Delhomme, S. Garrier, Various tools for optimizing large scale magnesium hydride storage, Journal of alloys and compounds 580 (2013) S324–S328.

[206] S. Nyallang Nyamsi, I. Tolj, M. Lototskyy, Metal hydride beds-phase change materials: Dual mode thermal energy storage for medium-high temperature industrial waste heat recovery, Energies 12 (20) (2019) 3949.

[207] D. N. Nkwetta, F. Haghighat, Thermal energy storage with phase change material-a state-of-the art review, Sustainable cities and society 10 (2014) 87–100.

[208] K. B. Minko, V. I. Artemov, G. G. Yan'kov, Numerical study of hydrogen purification using metal hydride reactor with aluminium foam, Applied Thermal Engineering 76 (2015) 175–184.

[209] F. Laurencelle, J. Goyette, Simulation of heat transfer in a metal hydride reactor with aluminium foam, International Journal of Hydrogen Energy 32 (14) (2007) 2957–2964.

[210] S. Ferekh, G. Gwak, S. Kyoung, H.-g. Kang, M.-h. Chang, S.-h. Yun, Y.-h. Oh, W. Kim, D. Kim, T. Hong, et al., Numerical comparison of heat-fin-and metal-foam-based hydrogen storage beds during hydrogen charging process, International Journal of Hydrogen Energy 40 (42) (2015) 14540–14550.

[211] C. Wang, T. Lin, N. Li, H. Zheng, Heat transfer enhancement of phase change composite material: Copper foam/paraffin, Renewable energy 96 (2016) 960–965.

[212] P. Zhang, Z. Meng, H. Zhu, Y. Wang, S. Peng, Experimental and numerical study of heat transfer characteristics of a paraffin/metal foam composite pcm, Energy Procedia 75 (2015) 3091–3097.

[213] Y. Du, Y. Ding, Towards improving charge/discharge rate of latent heat thermal energy storage (lhtes) by embedding metal foams in

phase change materials (pcms), Chemical Engineering and Processing: Process Intensification 108 (2016) 181–188.

[214] L. Tong, J. Xiao, P. Bénard, R. Chahine, Thermal management of metal hydride hydrogen storage reservoir using phase change materials, International Journal of Hydrogen Energy 44 (38) (2019) 21055–21066.

[215] S. Mellouli, N. B. Khedher, F. Askri, A. Jemni, S. B. Nasrallah, Numerical analysis of metal hydride tank with phase change material, Applied Thermal Engineering 90 (2015) 674–682.

[216] Y. Ye, J. Lu, J. Ding, W. Wang, J. Yan, Numerical simulation on the storage performance of a phase change materials based metal hydride hydrogen storage tank, Applied Energy 278 (2020) 115682.

[217] Y. Ye, J. Ding, W. Wang, J. Yan, The storage performance of metal hydride hydrogen storage tanks with reaction heat recovery by phase change materials, Applied Energy 299 (2021) 117255.

[218] X. Liu, N. Iftikhar, H. Huo, R. Li, P. S. Nielsen, Two approaches for synthesizing scalable residential energy consumption data, Future Generation Computer Systems 95 (2019) 586–600.

[219] T. Ahmad, H. Chen, Y. Guo, J. Wang, A comprehensive overview on the data driven and large scale based approaches for forecasting of building energy demand: A review, Energy and Buildings 165 (2018) 301–320.

[220] U. Desideri, L. Arcioni, D. Leonardi, L. Cesaretti, P. Perugini, E. Agabitini, N. Evangelisti, Design of a multipurpose "zero energy consumption" building according to european directive 2010/31/eu: Architectural and technical plants solutions, Energy 58 (2013) 157–167.

[221] Y. Schmitt, A. Troi, G. P. W. Sparber, Klimahaus casaclima–a regional energy certification system stimulates low energy architecture, in: Proceedings of PLEA2007-The 24th Conference on Passive and Low Energy Architecture, Singapore, 2007, pp. 22–24.

[222] A. Magrini, G. Lentini, S. Cuman, A. Bodrato, L. Marenco, From nearly zero energy buildings (nzeb) to positive energy buildings

(peb): The next challenge-the most recent european trends with some notes on the energy analysis of a forerunner peb example, Developments in the Built Environment 3 (2020) 100019.

[223] N. Omar, M. Daowd, O. Hegazy, G. Mulder, J.-M. Timmermans, T. Coosemans, P. Van den Bossche, J. Van Mierlo, Standardization work for bev and hev applications: Critical appraisal of recent traction battery documents, Energies 5 (1) (2012) 138–156.

[224] J. Laustsen, Energy efficiency requirements in building codes, energy efficiency policies for new buildings. iea information paper.

[225] Energyplus, https://energyplus.net/ Accessed on 20.12.2021.

[226] R. McKenna, E. Merkel, W. Fichtner, Energy autonomy in residential buildings: A techno-economic model-based analysis of the scale effects, Applied Energy 189 (2017) 800–815.

[227] European Commission, Photovoltaic geographical information system., https://re.jrc.ec.europa.eu/pvg_tools/it/#PVP Accessed on 20.12.2021.

[228] S. Onori, L. Tribioli, Adaptive pontryagin s minimum principle supervisory controller design for the plug-in hybrid gm chevrolet volt, Applied Energy 147 (2015) 224–234.

[229] N. Kim, S. Cha, H. Peng, Optimal control of hybrid electric vehicles based on pontryagin's minimum principle, IEEE Transactions on control systems technology 19 (5) (2010) 1279–1287.

[230] G. L. Plett, Sigma-point kalman filtering for battery management systems of lipb-based hev battery packs: Part 2: Simultaneous state and parameter estimation, Journal of power sources 161 (2) (2006) 1369–1384.

[231] R. Willis, Principles of mechanism, Longmans, Green, Harlow, 1870.

[232] S. K. Mohammadian, Y. Zhang, Thermal management optimization of an air-cooled li-ion battery module using pin-fin heat sinks for hybrid electric vehicles, Journal of Power Sources 273 (2015) 431–439.

[233] Marklines, Nissan leaf teardown: Lithium-ion battery pack structure, https://www.marklines.com/en/report_all/rep1786_201811 Accessed on 20.12.2021.

[234] L. Guzzella, A. Sciarretta, et al., Vehicle propulsion systems, Vol. 1, Springer, New York City, 2007.

[235] D. Parra, M. K. Patel, Effect of tariffs on the performance and economic benefits of pv-coupled battery systems, Applied energy 164 (2016) 175–187.

[236] V. Ciancio, S. Falasca, I. Golasi, G. Curci, M. Coppi, F. Salata, Influence of input climatic data on simulations of annual energy needs of a building: Energyplus and wrf modeling for a case study in rome (italy), Energies 11 (10) (2018) 2835.

[237] J. H. Yoon, R. Baldick, A. Novoselac, Dynamic demand response controller based on real-time retail price for residential buildings, IEEE Transactions on Smart Grid 5 (1) (2014) 121–129.

[238] Eurostat, Electricity price statistics, https://ec.europa.eu/eurostat/statistics-explained/index.php?title=Electricity_price_statistics Accessed on 20.12.2021.

[239] Banca D'Italia, Cambi di riferimento del 14 dicembre 2020, https://www.bancaditalia.it/compiti/operazioni-cambi/cambio/cambi_rif_20201214/ Accessed on 20.12.2021.

[240] Nissan, WLTP - Nissan Leaf, https://www-europe.nissan-cdn.net/content/dam/Nissan/ch/it/brochures/pkw/leaf-2018-brochure-listino-prezzi.pdf Accessed 10 02 2022.

[241] Change in distance travelled by car, https://www.odyssee-mure.eu/publications/efficiency-by-sector/transport/distance-travelled-by-car.html Accessed on 20.12.2021.

[242] Co2 emission performance standards for cars and vans, https://ec.europa.eu/clima/policies/transport/vehicles/regulation_en Accessed on 20.12.2021.

[243] European Parliament, Regulation (ec) no 715/2007 of the european parliament and of the council of 20 june 2007 on type approval of

motor vehicles with respect to emissions from light passenger and commercial vehicles (euro 5 and euro 6) and on access to vehicle repair and maintenance information (text with eea relevance).

[244] A. Rosati, G. Loreti, A. L. Facci, J. Taborri, S. Rossi, S. Ubertini, Smart energy community for electric vehicles recharge in a building environment, in: 13th International Conference on Applied Energy ICAE-2021, ICAE, 2021.

[245] C. Beckel, W. Kleiminger, R. Cicchetti, T. Staake, S. Santini, The eco data set and the performance of non-intrusive load monitoring algorithms, in: Proceedings of the 1st ACM conference on embedded systems for energy-efficient buildings, 2014, pp. 80–89.

[246] H. Wang, X. Zhang, L. Wu, C. Hou, H. Gong, Q. Zhang, M. Ouyang, Beijing passenger car travel survey: implications for alternative fuel vehicle deployment, Mitigation and Adaptation Strategies for Global Change 20 (5) (2015) 817–835.

[247] European Commission, Photovoltaic geographical information system (pvgis), https://ec.europa.eu/jrc/en/pvgis. Accessed 10 09 2021 (2021).

[248] Office of Energy Efficiency e Renewable Energy (EERE), https://openei.org/doe-opendata/dataset/commercial-and-residential-hourly-load-profiles-for-all-tmy3-locations-in-the-united-states Accessed on 20.12.2021.

[249] Arera, Andamento del prezzo dell'energia elettrica per il consumatore domestico tipo in maggior tutela, https://www.arera.it/it/dati/eep35.htm Accessed on 07.07.2021 (2021).

[250] Eurostat, Electricity price statistics, https://ec.europa.eu/eurostat/statistics-explained/index.php?title=Electricity_price_statistics Accessed on 07.07.2021 (2021).

[251] A. Filip, et al., Blued: A fully labeled public dataset for event-based nonintrusive load monitoring research, in: 2nd workshop on data mining applications in sustainability (SustKDD), Vol. 2012, 2011.

[252] A. Monacchi, D. Egarter, W. Elmenreich, S. D'Alessandro, A. M. Tonello, Greend: An energy consumption dataset of households in

italy and austria, in: 2014 IEEE International Conference on Smart Grid Communications (SmartGridComm), IEEE, 2014, pp. 511–516.

[253] J. Z. Kolter, M. J. Johnson, Redd: A public data set for energy disaggregation research, in: Workshop on data mining applications in sustainability (SIGKDD), San Diego, CA, Vol. 25, 2011, pp. 59–62.

[254] S. Makonin, F. Popowich, L. Bartram, B. Gill, I. V. Bajić, Ampds: A public dataset for load disaggregation and eco-feedback research, in: 2013 IEEE electrical power & energy conference, IEEE, 2013, pp. 1–6.

[255] N. Batra, M. Gulati, A. Singh, M. B. Srivastava, It's different: Insights into home energy consumption in india, in: Proceedings of the 5th ACM Workshop on Embedded Systems For Energy-Efficient Buildings, 2013, pp. 1–8.

[256] EV Database, Smart fortwo electric drive, https://ev-database.org/car/1090/Smart-ForTwo-Electric-Drive#charging. Accessed 10 02 2022.

[257] EV Database, Tesla model 3, https://ev-database.org/car/1555/Tesla-Model-3. Accessed 10 02 2022.

[258] E. Paffumi, M. De Gennaro, G. Martini, European-wide study on big data for supporting road transport policy, Case Studies on Transport Policy 6 (4) (2018) 785–802.

[259] Enel X, How much does it cost to charge an electric car?, https://corporate.enelx.com/en/question-and-answers/how-much-does-it-cost-to-charge-electric-car Accessed on 14.04.2022.

[260] European Environment Agency, Greenhouse gas emission intensity of electricity generation in europe, https://www.eea.europa.eu/ims/greenhouse-gas-emission-intensity-of-1 Accessed on 13.01.2023.

[261] J. López, D. Cordero-Moreno, Optimal plug-in electric vehicles charging coordination in electrical distribution networks, in: 2018 IEEE Third Ecuador Technical Chapters Meeting (ETCM), IEEE, 2018, pp. 1–6.

[262] M. Uzunoglu, M. Alam, Dynamic modeling, design and simulation of a pem fuel cell/ultra-capacitor hybrid system for vehicular applications, Energy Conversion and Management 48 (5) (2007) 1544–1553.

[263] S. Mekhilef, R. Saidur, A. Safari, Comparative study of different fuel cell technologies, Renewable and Sustainable Energy Reviews 16 (1) (2012) 981–989.

[264] Askoll, Electric and even more energetic. Askol eS_3., https://www.askollelectric.com/site/en/consumer-escooter-es3/ Accessed on 10.11.2021.

[265] Quotidiano Motori, Scooter elettrici più venduti in Italia: i migliori 5., https://www.quotidianomotori.com/moto/scooter/scooter-elettrici-piu-venduti/2/ Accessed on 10.11.2021.

[266] Vaielettrico, Scooter elettrici, listino facile: oltre 90 modelli., https://www.vaielettrico.it/moto-e-scooter-elettrici-il-listino-facile/ Accessed on 10.11.2021.

[267] Askoll, Electric scooter: user manual, Tech. rep., Askoll EVA Spa, https://www.askollelectric.com/download/en/askoll_libretto_uso_manutenzione_scooter.pdf, Accessed on 10.11.2021 (2016).

[268] Askoll, Battery for e-e-scooter 1.410 Wh, https://shop.askollelectric.com/en/products/Battery-for-e-scooter-1410-Wh Accessed on 10.11.2021.

[269] M. Tutuianu, P. Bonnel, B. Ciuffo, T. Haniu, N. Ichikawa, A. Marotta, J. Pavlovic, H. Steven, Development of the world-wide harmonized light duty test cycle (wltc) and a possible pathway for its introduction in the european legislation, Transportation research part D: transport and environment 40 (2015) 61–75.

[270] S. C. Walpole, D. Prieto-Merino, P. Edwards, J. Cleland, G. Stevens, I. Roberts, The weight of nations: an estimation of adult human biomass, BMC public health 12 (1) (2012) 1–6.

[271] J. T. McConville, C. E. Clauser, T. D. Churchill, J. Cuzzi, I. Kaleps, Anthropometric relationships of body and body segment moments

of inertia, Tech. rep., ANTHROPOLOGY RESEARCH PROJECT INC YELLOW SPRINGS OH (1980).

[272] CGM, 508A BERLINO MONO, https://cgmitalia.net/product/berlino/ Accessed on 10.11.2021.

[273] C.-Y. Tseng, Y.-F. Lue, Y.-T. Lin, J.-C. Siao, C.-H. Tsai, L.-M. Fu, Dynamic simulation model for hybrid electric scooters, in: 2009 IEEE International Symposium on Industrial Electronics, IEEE, 2009, pp. 1464–1469.

[274] S. A. Khateeb, M. M. Farid, J. R. Selman, S. Al-Hallaj, Mechanical–electrochemical modeling of li-ion battery designed for an electric scooter, Journal of power sources 158 (1) (2006) 673–678.

[275] h2planet, Stack h 1000: The ready to use fuel-cell stack!, Tech. rep., https://www.h2planet.eu/grk_files/catalogo/prodotti/brochure/Stack/Brochure_H-1000_EN.pdf, Accessed on 10.11.2021.

[276] h2planet, Stack h 2000: The ready to use fuel-cell stack!, Tech. rep., https://www.h2planet.eu/grk_files/catalogo/prodotti/brochure/Stack/Brochure_H-2000_EN.pdf, Accessed on 10.11.2021.

[277] FuelCellStore, 1kW Hydrogen Fuel Cell Power Generator, https://www.fuelcellstore.com/fuel-cell-stacks/high-power-fuel-cell-stacks/g-hfcs-1kw36v-1000w-hydrogen-fuel-cell-power-generator Accessed on 10.11.2021.

[278] FuelCellStore, 2kW Hydrogen Fuel Cell Power Generator, https://www.fuelcellstore.com/fuel-cell-stacks/high-power-fuel-cell-stacks/g-hfcs-2kw25v-1kw-hydrogen-fuel-cell-power-generator Accessed on 10.11.2021.

[279] h2planet, Myh2-hydrogen stored simple: H_2 smart metal hydrides storage system, Tech. rep., https://www.h2planet.eu/grk_files/catalogo/prodotti/brochure/MyH2/Brochure_MyH2_ENG.pdf, Accessed on 10.11.2021.

[280] Hollandbikeshop.com, E-Motion E-Bike Battery shop the largest and most affordable!, https://hollandbikeshop.com/en-gb/bicycle-parts-electric-bicycle/e-motion-electric-bicyc

le-parts/e-motion-e-bike-battery-parts/e-motion-e-bike-battery Accessed on 10.11.2021.

[281] Y. Zhang, C. Zhang, R. Fan, S. Huang, Y. Yang, Q. Xu, Twin delayed deep deterministic policy gradient-based deep reinforcement learning for energy management of fuel cell vehicle integrating durability information of powertrain, Energy Conversion and Management 274 (2022) 116454.

[282] S. Dirkes, J. Leidig, P. Fisch, S. Pischinger, Prescriptive lifetime management for pem fuel cell systems in transportation applications, part i: State of the art and conceptual design, Energy Conversion and Management 277 (2023) 116598.

[283] Hollandbikeshop.com, E-Motion E-Bike Battery Li-ion 24S/10Ah - Black, https://hollandbikeshop.com/en-gb/bicycle-parts-electric-bicycle/e-motion-electric-bicycle-parts/e-motion-e-bike-battery-parts/e-motion-e-bike-battery/e-motion-e-bike-battery-li-ion-24s-10ah-black/ Accessed on 10.11.2021.

[284] h2planet, Myh2 slim 350-slim hydrogen storage: H_2 slim and smart metal hydrides storage system, Tech. rep., https://www.h2planet.eu/grk_files/catalogo/prodotti/brochure/MyH2/Brochure_MyH2_SLIM350_ENG.pdf, Accessed on 10.11.2021.

[285] h2planet, CARBON FIBER CYLINDER - X-FIBER S, https://www.h2planet.eu/en/products/professional/Hydrogenstorage/cilindri_in_fibra_di_carbonio/ Accessed on 10.11.2021.

[286] h2planet, X-Fiber S9, https://www.h2planet.eu/en/detail/xfiber_s9 Accessed on 10.11.2021.

[287] h2planet, X-Fiber S6.8, https://www.h2planet.eu/en/detail/xfiber_s68 Accessed on 10.11.2021.

[288] A. Gupta, Vätgaslagring,-distribution och-rening (2017).

[289] D. B. Crawley, L. K. Lawrie, F. C. Winkelmann, W. F. Buhl, Y. J. Huang, C. O. Pedersen, R. K. Strand, R. J. Liesen, D. E. Fisher, M. J. Witte, et al., Energyplus: creating a new-generation building

energy simulation program, Energy and buildings 33 (4) (2001) 319–331.

[290] S. S. Kumar, V. Himabindu, Hydrogen production by pem water electrolysis–a review, Materials Science for Energy Technologies 2 (3) (2019) 442–454.

[291] L. Andreassi, G. Falcucci, A. L. Facci, S. Ubertini, Environmental and health impact of electric and hydrogen light vehicles: The case of an italian small city, Tech. rep., SAE Technical Paper (2019).

[292] A. Chaise, P. De Rango, P. Marty, D. Fruchart, Experimental and numerical study of a magnesium hydride tank, International Journal of Hydrogen Energy 35 (12) (2010) 6311–6322.

[293] Z. Bao, F. Yang, Z. Wu, X. Cao, Z. Zhang, Simulation studies on heat and mass transfer in high-temperature magnesium hydride reactors, Applied energy 112 (2013) 1181–1189.

[294] S. Mellouli, E. Abhilash, F. Askri, S. B. Nasrallah, Integration of thermal energy storage unit in a metal hydride hydrogen storage tank, Applied Thermal Engineering 102 (2016) 1185–1196.

[295] J. B. Von Colbe, J.-R. Ares, J. Barale, M. Baricco, C. Buckley, G. Capurso, N. Gallandat, D. M. Grant, M. N. Guzik, I. Jacob, et al., Application of hydrides in hydrogen storage and compression: Achievements, outlook and perspectives, international journal of hydrogen energy 44 (15) (2019) 7780–7808.

[296] B. Talaganis, G. Meyer, P. Aguirre, Modeling and simulation of absorption–desorption cyclic processes for hydrogen storage-compression using metal hydrides, International journal of hydrogen energy 36 (21) (2011) 13621–13631.

[297] W. D. Murray, F. Landis, Numerical and machine solutions of transient heat-conduction problems involving melting or freezing: Part i-method of analysis and sample solutions, Journal of Heat Transfer 81 (2) (1959) 106–112.

[298] P. Jany, A. Bejan, Scaling theory of melting with natural convection in an enclosure, International Journal of Heat and Mass Transfer 31 (6) (1988) 1221–1235.

[299] R. Sreeraj, A. Aadhithiyan, S. Anbarasu, Integration of thermal augmentation methods in hydride beds for metal hydride based hydrogen storage systems: review and recommendation, Journal of Energy Storage 52 (2022) 105039.

Ringraziamenti

Ci tengo a ringraziare i miei familiari ed Emanuela che, con il loro continuo supporto e la loro vicinanza, mi hanno permesso di raggiungere questo importante traguardo vivendo il percorso in maniera leggera e serena. L'aver condiviso questo risultato con voi lo rende unico e speciale.

Vorrei poi ringraziare il Professor Facci ed il Professor Ubertini per essere stati una preziosa guida e per avermi dato questa magnifica opportunitá di crescita personale e professionale. La loro competenza e la loro passione sono stati per me una continua fonte di ispirazione.

Vorrei inoltre ringraziare Gabriele per essere stato un collega di alto livello, ma soprattutto un amico vero e sincero.

Un ringraziamento speciale infine a Juri e a tutti gli amici e colleghi dell'Unitus.